



Max Planck **Graduate Center** 
mit der Johannes Gutenberg-Universität Mainz

3D-Electron Microscopy of Protein Complexes of Different Size and Symmetry

Dissertation zur Erlangung des Grades

“Dr. rer. nat.”

an der Johannes Gutenberg-Universität Mainz

Philipp Arnold

Geb. am 04.10.1982 in Kaiserslautern

Mainz, Oktober 2012

Dekan:

1. Berichterstatter:

2. Berichterstatter:

Tag der Prüfung:

“Wichtig ist, dass man nicht aufhört zu fragen!”

Albert Einstein

Table of contents

1	Introduction	1
1.1	Electron microscopy of proteins	1
1.2	Goal of the PhD thesis	2
1.3	Arthropod hemocyanins (Hc)	3
1.3.1	Hemocyanins	3
1.3.2	The 2x6mer hemocyanins in arthropods	4
1.3.3	Goal of this project	4
1.4	The gp140 proteins from HIV	5
1.4.1	Introduction to HIV	5
1.4.2	The virus structure	6
1.4.3	The envelope glycoproteins	6
1.4.4	Goal of this project	8
1.5	The 20S-PA28 proteasome complex	9
1.5.1	The proteasome - an overview	9
1.5.2	Activation and regulation of the 20S proteasome	10
1.5.3	Goal of this project	12
1.6	The hepatitis B virus (HBV) capsid	13
1.6.1	Structure of the capsid	13
1.6.2	The HBV capsid as antigen carrier	15
1.6.3	Goal of this project	16
2	Material and Methods	19
2.1	Animals	19
2.2	Protein samples	23
2.2.1	2x6meric hemocyanins	23
2.2.2	HIV-Env proteins, CD4 and mABs	23
2.2.3	20S and 20S-PA28 proteasome complex	23
2.2.4	Hepatitis B virus capsids	23
2.3	Electron microscopes (EM)	24
2.4	Electron microscopic detection devices	25
2.5	Computer hardware	25
2.6	Computer software	26
2.7	EM grids	28
2.8	Negative staining	28
2.8.1	Basic principles	28
2.8.2	The stain solutions	29

2.8.3	The single droplet method	30
2.8.4	The Teflon block staining method	31
2.9	Preparation of unstained vitrified samples	32
2.10	Image processing methods	34
2.10.1	Particle selection	34
2.10.2	CTF correction	34
2.10.3	Bandpass filtering	34
2.10.4	Particle alignment	36
2.10.5	Multivariate statistical analysis (MSA)	37
2.10.6	Orientation determination	38
2.10.7	Projection matching	40
2.10.8	3D reconstruction of class sum images	42
2.10.9	Refinement as an iterative process	42
2.10.10	Resolution determination of the reconstructed model	42
2.10.11	Filtering and 3D masking	43
3	Results	47
3.1	Crustacean 2x6mer hemocyanins	47
3.1.1	<i>Astacus leptodactylus</i> 2x6mer hemocyanin (AleHc)	49
3.1.2	<i>Carcinus maenas</i> 2x6mer hemocyanin (CmaHc)	50
3.1.3	<i>Homarus americanus</i> 2x6mer hemocyanin (HamHc)	51
3.1.4	<i>Odontodactylus scyllarus</i> 2x6mer hemocyanin (OscHc)	52
3.2	The gp140 proteins from HIV X4- and R5-strands	55
3.2.1	3D reconstruction of NL4-3 (X4) and Ada (R5)	55
3.2.2	Molecular model building and immunoelectron microscopy	56
3.2.3	Docking of the molecular model into NL4-3 and Ada	58
3.2.4	Activation of NL4-3 with CD4	59
3.3	The 20S-PA28 proteasome complex	62
3.3.1	Raw data acquisition and class sum formation	62
3.3.2	Density map and molecular model of the 20S-PA28 complex	64
3.3.3	3D density map and docked molecular model of the 20S particle	67
3.4	Hepatitis B virus capsids	69
3.4.1	3D reconstruction of T3- and T4-assemblies	69
3.4.2	Averages of the asymmetric subunits	73
3.4.3	Structural details of the T3 capsid	74
3.4.4	Connections between dimers in the T3 capsid	75
3.4.5	Resolution of the inserted epitope	77

4 Discussion	79
4.1 Arthropod 2x6mer hemocyanins	79
4.1.1 Decapod 2x6mer hemocyanins	79
4.1.2 <i>Odontodactylus scyllarus</i> 2x6mer hemocyanin	80
4.1.3 Comparison of the studied 2x6mers to a crustacean 4x6mer	80
4.2 Envelope proteins from HIV	84
4.3 The 20S and 20S-PA28 proteasome	86
4.3.1 Preparation and image acquisition of the proteasome sample	86
4.3.2 Evaluation of the 3D reconstructions	86
4.3.3 Conclusions on function and structure of the 20S-PA28 complex	89
4.4 Hepatitis B virus capsids	91
4.4.1 Evaluation of the T3 capsid	91
4.4.2 Interaction in the HBV core protein dimer	91
4.4.3 Interaction between HBV core protein dimers	94
4.5 Negative staining EM and 3D reconstruction	96
4.5.1 Comparing overall structural details of protein complexes	96
4.5.2 Comparing molecular details	97
5 Summary	101
6 Zusammenfassung	103
7 Appendix	105
8 Bibliography	109
9 Danksagung - Acknowledgment	125
10 Erklärung and Copyright	129
11 Curriculum vitae	131

List of Figures

Fig. 1.1	Replica of the original 1934 Ernst Ruska EM.	1
Fig. 1.2	Arthropod hemocyanin organization	3
Fig. 1.3	HIV distribution among adults	5
Fig. 1.4	HIV architecture	6
Fig. 1.5	The 20S proteasome.	9
Fig. 1.6	20s with different regulators.	10
Fig. 1.7	Double capped 20S-PA26 complex	11
Fig. 1.8	Worldwide hepatitis B prevalence.	13
Fig. 1.9	Nomenclature of subunits in HBV capsids.	14
Fig. 1.10	Stabilizing structural elements in the HBV core protein	15
Fig. 1.11	3D reconstruction of a T4 HBV capsid	16
Fig. 2.1	The freshwater crayfish <i>Astacus leptodactylus</i>	19
Fig. 2.2	The lobster <i>Homarus americanus</i>	20
Fig. 2.3	The shore crab <i>Carcinus maenas</i>	21
Fig. 2.4	The mantis shrimp <i>Odontodactylus scyllarus</i>	22
Fig. 2.5	Tecnai12 electron microscope.	24
Fig. 2.6	Beowulf cluster at the JGU Mainz	26
Fig. 2.7	Grid architecture	28
Fig. 2.8	Different staining results.	29
Fig. 2.9	The single droplet method	30
Fig. 2.10	Block staining.	31
Fig. 2.11	Ice quality of vitrified samples	32
Fig. 2.12	Gatan plunge-freezer CP3	33
Fig. 2.13	Bandpass filter	35
Fig. 2.14	Multy-reference-alignment (MRA).	36
Fig. 2.15	Hierarchical ascendant classification (HAC) tree.	38
Fig. 2.16	Euler angles representation	39
Fig. 2.17	Slices through a 3D volume	41
Fig. 2.18	Iterative refinement process	44
Fig. 3.1	Development of a 2x6mer hemocyanin reconstruction.	47
Fig. 3.2	Dimensions of the decapod-type 2x6mer hemocyanin	48
Fig. 3.3	<i>Astacus leptodactylus</i> 2x6mer hemocyanin shown at high threshold	48
Fig. 3.4	<i>Astacus leptodactylus</i> 2x6mer hemocyanin	49
Fig. 3.5	<i>Carcinus maenas</i> 2x6mer hemocyanin.	50
Fig. 3.6	<i>Homarus americanus</i> 2x6mers hemocyanin.	51
Fig. 3.7	Negative stain image of <i>O. scyllarus</i>	52

Fig. 3.8	Development of the 3D density map from the 2x6mer OscHc.	53
Fig. 3.9	<i>Odontodactylus scylarus</i> 2x6mer hemocyanin	54
Fig. 3.10	Negative stain of NL4-3	55
Fig. 3.11	Initial gp140 model	56
Fig. 3.12	3D reconstruction of NL4-3 and ADA gp140 trimers	57
Fig. 3.13	mAbs binding epitops.	58
Fig. 3.14	Docking of mAb 447-52D	59
Fig. 3.15	Molecular models of NL4-3 gp140 and ADA gp140 trimers	60
Fig. 3.16	3D reconstruction of CD4-liganded NL4-3 gp140 trimers.	61
Fig. 3.17	Negative stain image of 20S-PA28 and 20S particles	62
Fig. 3.18	Single 20S-PA28 and 20S particles in negative stain	63
Fig. 3.19	Class sum images from 20S-PA28 and 20S particles	63
Fig. 3.20	3D reconstruction of the 20S-PA28 complex	65
Fig. 3.21	3D reconstruction of 20S-PA28 with docked crystal structures	66
Fig. 3.22	3D reconstruction of the 20S proteasome	67
Fig. 3.23	Docking of the 20S proteasome with docked crystal structure	68
Fig. 3.24	Electron microscopy of HBV capsids	69
Fig. 3.25	Density maps of T3 and T4 HBV capsids.	70
Fig. 3.26	Molecular models of T4 and T3 HBV capsids	71
Fig. 3.27	Averaged dimer of T4 and T3.	72
Fig. 3.28	Symmetry axes in the T3 capsid	73
Fig. 3.29	Pseudo-C3 symmetry axis.	75
Fig. 3.30	Dimer connections in HBV capsids	76
Fig. 3.31	Pseudo-C3-symmetry axis at different threshold levels	77
Fig. 4.1	Isopod 2x6mer hemocyanin	81
Fig. 4.2	Comparison of 2x6mer hemocyanins with the 4x6mer hemocyanin from <i>C. truncata</i>	82
Fig. 4.3	Hypothetical evolution of decapod hemocyanins	83
Fig. 4.4	Comparison of NL4-3 and Ada gp120 parts.	85
Fig. 4.5	Comparison of symmetric and asymmetric proteasome reconstructions	87
Fig. 4.6	3D density maps of the 20S-PA28 complex and the 20S proteasome at differet thresholds	89
Fig. 4.7	Cut-open view of the docked 20S-PA28.	90
Fig. 4.8	The hydrophobic core in HBV capsids	92
Fig. 4.9	Hydrophobic interaction in the T3 capsid	93
Fig. 4.10	Connection between dimers in the T3 capsid	95
Fig. 4.11	Hypothetical interactions between dimers in HBV capsids.	96

1 Introduction

1.1 Electron microscopy of proteins

The invention of the electron microscope (EM) in 1931 by Ernst Ruska and Max Knoll (Borries and Ruska, 1938) (Fig. 1.1) enabled the viewing of structures below the size of a cell, opening an entirely new field in biology. Originally developed to view viruses, it was initially

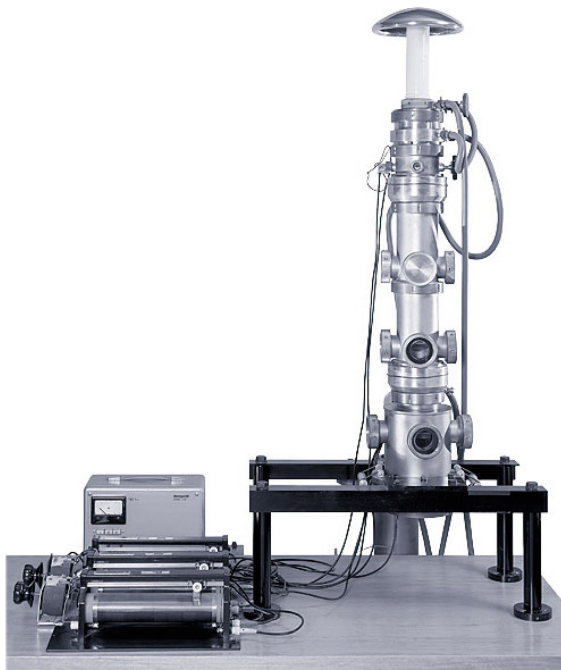


Fig. 1.1 Replica of the original 1934 Ernst Ruska EM. Part of the collection situated in the German museum in Munich. (www.deutsches-museum.de)

used to display metal lattices (Ruska, 1932). From these two very different applications, one sees the diverse possibilities that electron microscopy offers. From metal lattice reconstruction (e.g. Iijima, 1973) over element analysis (e.g. Egerton, 2012) up to protein structures at high resolution (e.g. Zhou, 2008) many questions from the fields of physics, chemistry and biology can be answered with the help of the EM. As I was working on biological samples only, I will give a short introduction into the developments that were made over the years. The main problem using biological samples in the electron microscope is their beam sensitivity and low natural contrast. There are several possibilities to enhance contrast in the EM. The first one applied was to negatively stain the samples using heavy atoms (e. g. Brenner and Horne, 1959). Although this method was already suggested in 1934,

there are still developments in the field such as cryo-negative staining (e.g. De Carlo and Harris, 2011). This method basically coats the sample with heavy atoms and under the EM one only sees the shell or solvent excluded surface of the original sample.

The second very successful method is to vitrify the unstained sample in an aqueous environment (Dubochet and McDowell, 1981; Dubochet et al., 1982). Therefore the sample is shock-frozen using liquid ethane or propane (<20ms) to prevent the formation of ice crystals. The problem with unstained frozen samples is the difficult handling and the very low natural contrast under the EM. The difficult handling comes from the fact that temperatures above -150°C lead to the formation of crystals and therefore the sample has to be kept at liquid nitrogen temperature. The low contrast results from comparable scattering properties of the proteins and the surrounding media (vitreous water). Therefore images from vitrified samples are usually taken at defocus (Frank, 2002).

As cryo-EM has become a very powerful tool in structure determination of biological samples, special EMs have been developed during the last years. From FEI (Eindhoven, Netherlands) the TecnaiG² Polara and more recently the TitanKryos have been introduced. From other manufactures such as JEOL (Akishima, Japan) or ZEISS (Jena, Germany) there have been developments, too.

1.2 Goal of the PhD thesis

With the help of negatively stained biological samples many questions have been answered over the years and the understanding of protein complexes rose through their visualisation. Nevertheless there are limits in resolution (~15Å) and therefore only certain questions can be answered. During my PhD project I will answer different questions with the help of negative stain EM and compare the results in some cases with the results from vitrified samples. In this thesis I will show that negative stain EM can be a very helpful tool during the analysis of protein complexes from different size and shape and that it is possible to localize certain epitopes with the help of antibodies, thus enhancing the degree of information in structures derived from negative stain EM. At the same time limits will be shown that display insuperable borders of the method. In the following parts of the introduction I will introduce the protein complexes I used during my studies and will raise some questions that should be answered during the reconstruction process.

1.3 Arthropod hemocyanins (Hc)

1.3.1 Hemocyanins

Hemocyanins are the respiratory proteins of many molluscs and arthropods. Their function is the transport of oxygen from the respiratory tissue (lungs, gills) to the consuming tissues. Two copper ions, coordinated by three histidine each, bind oxygen molecules reversely. Although having the same physiological function, their structures differ substantially. In the electron microscope molluscan hemocyanins appear as hollow cylindrical molecules. Work done in the Markl lab (e.g. Gatsogiannis et al., 2007; Gatsogiannis and Markl, 2009) revealed many details of the architecture of these fascinating molecules.

Hemocyanins from arthropods on the other hand form cubic structures. The smallest building block is the hexamer (Fig. 1.2), consisting of six monomers that are non-covalently linked (Markl and Decker, 1992).

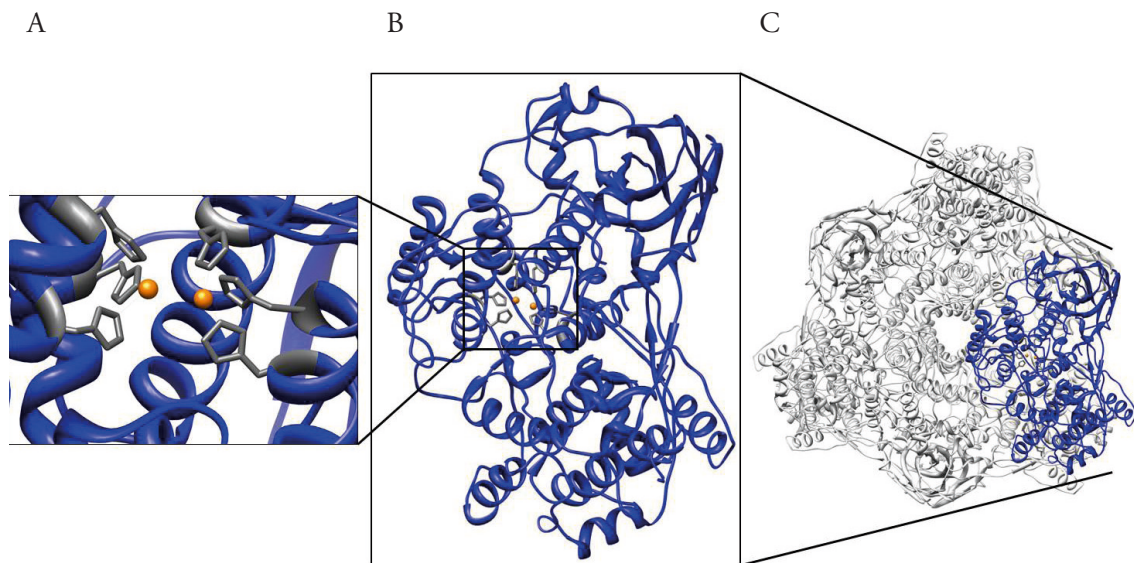


Fig. 1.2 Arthropod hemocyanin organization. (A) Active site of the subunit. Two copper ions (orange) are coordinated by three histidines (grey) respectively. (B) Hemocyanin subunit. Note that the active site is located in the centre. (C) Topview of the hexamer. Note the obvious C3 symmetry. The C2 symmetry axis is orthogonal to this one.

The hemocyanin hexamer from *Panulirus interruptus*, the Californian spiny lobster, was crystallized (Voldeba and Hol, 1989) (pdbentry1HCY). From *Limulus polyphemus*, the horseshoe crab, oxygenated (pdbentry1NOL) and deoxygenated (pdbentry1LLA) subunits were resolved (Hazes et al., 1993) at 2-3Å. Depending on the species, oligo-hexameric assemblies occur, such as 2x6mers (e.g. in *Carcinus menas*, the shore crab), 4x6mers (e.g. *Eurypelma cali-*

fornicum, the tarantula), 6x6mers (e.g. *Scutigera coleoptrata*, the house centipede) or 8x6mers (e.g. *Limulus polyphemus*, the horseshoe crab) (Markl and Decker, 1992).

1.3.2 The 2x6mer hemocyanins in arthropods

The three-dimensional structure of 2x6mer arthropod hemocyanins has long been under debate (Markl and Decker, 1992; Micetic et al., 2011). In this study the 2x6mer hemocyanins from the three decapods *Astacus leptodactylus* (AleHc), *Homarus americanus* (HamHc) and *Carcinus menas* (CmaHc) were studied. Furthermore the 2x6mer hemocyanin of the stomatopod *Odontodactylus scyllarus* (OscHc) was examined. Hereby the structural differences in respect to the orientation of the two hexamers within the multimeric structure were of interest. Previous studies suggest different architectures for 2x6mer hemocyanins from different species (Markl, 1980; Bijlholt&van Bruggen, 1985; Scherbaum et al., 2010; Markl and Decker, 1992; Micetic et al., 2011). However, this remained uncertain, because convincingly resolved 3D structures are lacking for solitary 2x6mers. On the other hand, knowledge of the inter-hexamer interfaces at the level of single amino acids is prerequisite for understanding the allosteric interaction of hexamers.

1.3.3 Goal of this project

The goal of this project was to obtain three dimensional density maps from the respective 2x6mer hemocyanins that allow automated docking of the crystallographic hexamer. Ultimately the quaternary structure of the 2x6mer and the orientation of the two hexamers with respect to each other should be resolved. For this a resolution of 25-30Å should suffice. As this resolution can be reached with negatively stained samples, this method was chosen as it is simple and fast. It enables one to check many different samples within a short period of time and makes sample handling easier. Another aspect was to see whether the obtained 2x6mer structures can be found as sub-structures of higher oligomeric hemocyanins.

1.4 The gp140 proteins from HIV

1.4.1 Introduction to HIV

The human immunodeficiency virus (HIV) belongs to the large family of retroviruses and causes AIDS (Acquired Immune Deficiency Syndrome). In 2010 34 million people were infected with HIV and 37 million had already died from AIDS (UNAIDS, World AIDS Day Report 2011). The first cases of AIDS were described in 1981 (Morbidity and Mortality Weekly Reports 1981) where an unusual number of homosexual men were found with *Pneumocystis* Pneumonia, a disease almost exclusively found in immune system deficient patients. Further studies of the virus have shown that it developed from the SIV (simian immunodeficiency virus) and might have developed in the early 20th century in Cameroon. Today 2/3 of all HIV positive patients live in the sub-Sahara region in Africa. In some countries 20% of the people are infected (e.g. South Africa) and the country with the highest percentage infection rate is Swaziland with 42% HIV positives (UNAIDS, World AIDS Day Report 2011) (Fig. 1.3).

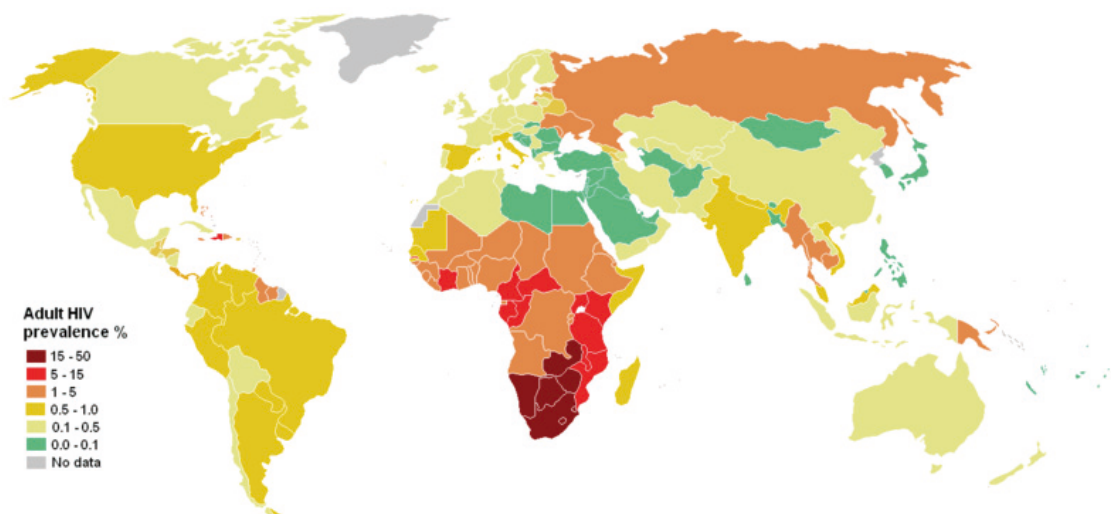


Fig. 1.3 HIV distribution among adults. Note the high numbers in the sub-Sahara region. Among Western countries, the USA has one of the highest prevalence rates. The country with the highest overall HIV infection rate is Swaziland, a small country embedded into the South African mainland. 42% of all adults between 18 and 49 years old are HIV positive (UNAIDS, World AIDS Day Report 2011).

1.4.2 The virus structure

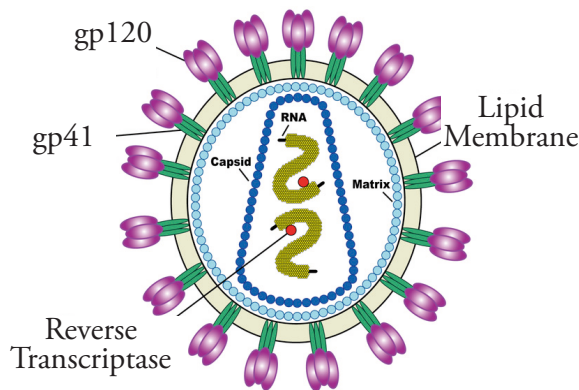


Fig. 1.4 HIV architecture. The glycoproteins are embedded into a lipid membrane which is followed by matrix proteins. These protect the virus capsid that contains the RNA and the reverse transcriptase (image: wikipedia).

HIV has two single-stranded RNA molecules in its inner part (Fig. 1.4). These are surrounded by a capsid made up of the viral protein p24. This capsid also hosts some other proteins important for the virus: the nucleocapsid proteins p6 and p7, preventing the RNA from being degraded, an integrase and a reverse transcriptase.

Around this inner capsid is a matrix formed by p17, ensuring structural integrity and stability of the virion. The matrix is surrounded by a membrane that is made from host cell lipids. This membrane hosts the envelope proteins (Env) gp41 and gp120. These proteins play a crucial role in receptor and co-

receptor binding and in membrane fusion and therefore are major medical targets.

1.4.3 The envelope glycoproteins

The envelope glycoproteins (Env) of HIV are the key elements mediating viral entry into cells and represent the major target for HIV-neutralizing antibodies (Caffrey, 2011). Env derive from gp160 precursors that trimerize in the endoplasmic reticulum and, following cleavage in the Golgi, generate noncovalently associated trimers of gp120 and gp41 heterodimers. CD4-gp120 binding induces conformational changes in Env both to expose epitopes for subsequent interaction with coreceptors (CCR5 or CXCR4) and to activate the transmembranary gp41 subunits for membrane fusion. Fusion is initiated by insertion of the gp41 fusion peptides into the cell membrane and subsequent formation of a 6-helix bundle structure by intramolecular association of the N- and C-terminal heptad repeats (NHR, CHR) of three gp41 protomers (Harrison, 2008).

According to their coreceptor usage, HIV-1 strains can be subdivided into CCR5- (R5) and CXCR4-tropic (X4) variants. While R5 strains are usually transmitted and predominate at early stages of infection, X4 variants occur in approximately 50% of subtype B infected patients in chronic stages of the disease and correlate with an accelerated progression to AIDS (Mosier, 2009). CXCR4 usage is mainly mediated by mutations in the variable loop 3 (V3)

of gp120, especially at the V3 stem, providing an increased positive net charge (Poveda et al., 2010). A fundamental knowledge of the Env trimeric structure and activation process is essential for a detailed comprehension of viral entry and tropism as well as for the development of efficient entry inhibitors and immunogens. Due to the high degree of flexibility, instability and glycosylation of native Env, an accurate structural characterization of the Env trimer is a challenging task. X-ray crystallography is yet restricted to monomeric gp120 substructures of HIV or SIV devoid of substantial variable domains (Chen et al., 2005; Huang et al., 2005; Kwong et al., 2000; Kwong et al., 1998; Pancera et al., 2010; Wyatt et al., 1998; Zhou et al., 2007). The arrangement of the gp41 structure (Buzon et al., 2010) within the spike context is even more obscure. Structures of whole trimers of HIV or SIV were obtained by several groups using cryoelectron tomography. Fitting of known crystal structures into the tomographic density maps led to molecular models of Env roughly elucidating trimer assembly and CD4 induced conformational changes. However, the proposed quaternary structures differ between studies from rods to mushroom like spikes with one or three gp41 protrusions (Liu et al., 2008; White et al., 2010; Zanetti et al., 2006; Zhu et al., 2006). Recently, structural analyses using soluble trimeric Env constructs complemented these models (Harris et al., 2011; Moscoso et al., 2011; Wu et al., 2010; Mao et al., 2012; Tran et al., 2012). Solubilized spikes from virus-like particles with cross-linked gp120 and gp41 devoid of intracellular and transmembranary regions supported the existence of three “legs” instead of one “stalk” (Wu et al., 2010).

Alternatively to solubilized spikes, soluble trimeric gp140 constructs were generated to mimic the exterior part of the viral spikes (Binley et al., 2000; Zhang et al., 2001). These gp140 constructs, composed of gp120 linked to the extracellular part of gp41, were proven to be useful tools in immunologic and structural studies (Derby et al., 2007). Expression of gp140 can be achieved either by deleting the interjacent protease cleavage site (Zhang et al., 2001) or by introduction of an interprotomeric stabilizing disulfide bridge (Binley et al., 2000). The first structural analysis of such trimeric Env constructs was published recently using a subtype C gp140 with partially truncated V2 loops, unbound or bound to a CD4 mimicking miniprotein (Moscoso et al., 2011). The authors observed an “open roof” architecture of gp140 and suggest that CD4 induces an outward shift of gp120 domains associated with a loosening of prefusion gp41-gp120 interactions. Subramaniam and coworkers could demonstrate, moreover, that soluble gp140 constructs display an almost identical gp120 molecular arrangement as that observed in intact HIV-1 virions, both in the unliganded and the CD4 activated state (Harris et al., 2011).

All the aforementioned studies have characterized trimeric R5 Env, either from intact virions or from soluble gp140 constructs derived from SIV or HIV-1. No quaternary structural data is available for X4 Envs. A deeper knowledge about the X4 Env architecture and the differences to R5 Env would provide a better understanding of structural properties associ-

ated with the CXCR4 coreceptor shift (White et al., 2010; Lusso et al., 2005; Naganawa et al., 2008; Sharon et al., 2003; Wu et al., 2010; Zhuang et al., 2011) and assist drug design against X4 HIV-1 infections.

1.4.4 Goal of this project

This part of my PhD thesis had the goal to provide a 3D envelope for gp140 molecules from X4- and R5-tropic viruses. As there is no crystal structure available for the entire gp140 molecule, but only for its subdomains, immunoelectron microscopy of different epitopes could be performed to propose a reliable molecular model. Moreover the Env proteins should be incubated with CD4, their primary receptor, to see structural changes due to interaction with it. The results from both gp140 types, should be compared to better understand the binding mechanism of the virus to the cell surface.

1.5 The 20S-PA28 proteasome complex

1.5.1 The proteasome - an overview

The 20S proteasome is one of the key players in protein degradation that is found in archaeans, bacteria and eucaryotes. It consists of 2x2 ring systems (Fig. 1.5). The inner rings are built by the beta subunits and the outer rings are built by the alpha subunits. In Archaea and Bacteria the alpha and beta subunits are homo-oligomers and the beta subunits are all proteolytically active after removal of the propetide (Bochtler et al., 1999).

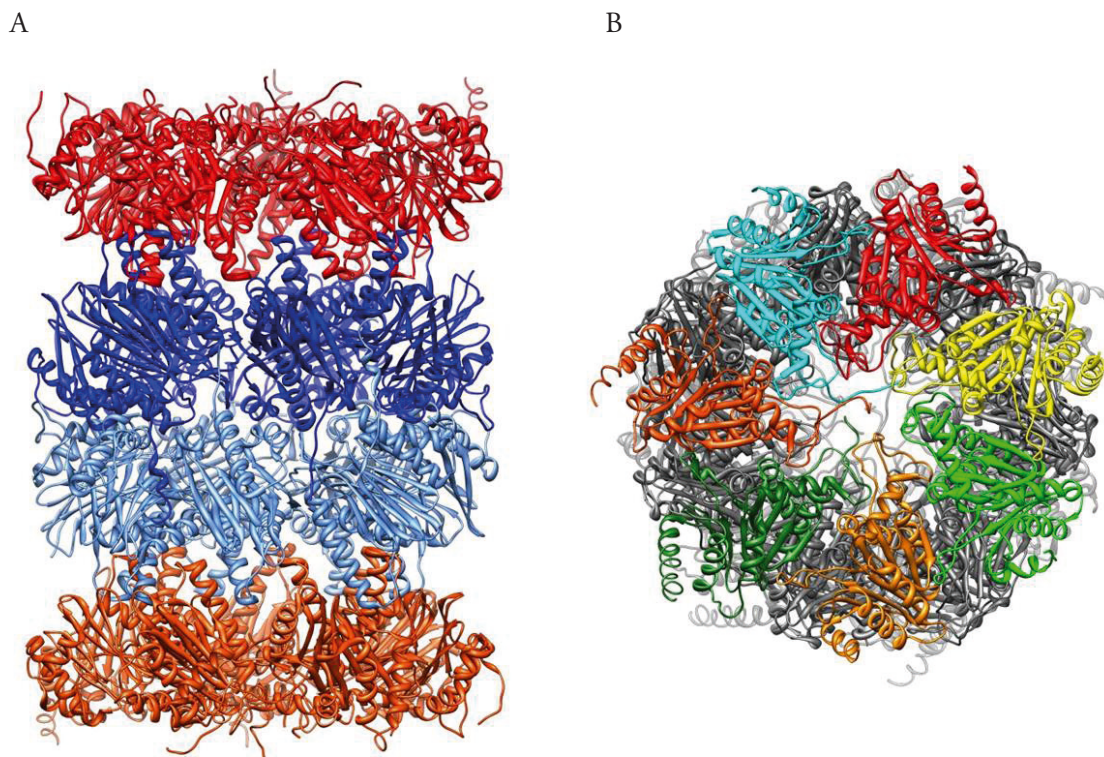


Fig. 1.5 The 20S proteasome. (A) Side view with the alpha subunits in red and the beta subunits in blue. The C2 symmetry axis is perpendicular to the plane. (B) Top view of the 20S particle. The seven subunits are colour-coded. In low resolution this view is along the pseudo c7 symmetry axis (pictures were produced using the bovine crystal structure; pdbentry1IRU).

The eucaryotic proteasome consists of seven different alpha and beta subunits respectively, these are termed $\alpha 1$ - $\alpha 7$ and $\beta 1$ - $\beta 7$. From X-ray crystallography of the bovine 20S proteasome (Unno et al., 2002)(pdbentry1IRU) it is known that it displays C2-symmetry (Fig. 1.5 (A)). In contrast to procaryotic proteasome there are only three beta subunits proteolytic active: $\beta 1$, $\beta 2$, and $\beta 5$. $\beta 1$ has an caspase-like activity, that is explained by an arginine (45) in

its S1 pocket. β 2 has trypsin-like activity and this can be explained by a glutamate residue (53) found in the S1 pocket. β 5 displays chymotrypsin-like activity and this might be due to apolar methionine (45) found in S1. The S1 pocket describes the first amino acid C-terminal of the catalytic amino acid that is found in the active site. All subunits cleave their own propetide during maturation and therefore they are independent from activating enzymes (Bochtler et al., 1999).

1.5.2 Activation and regulation of the 20S proteasome

To mediate the 20S proteasome activity, two complexes have been described. The PA700 (19S) regulatory complex and the PA28 (11S) activating complex (Bochtler et al., 1999). The PA700 complex together with the 20S proteasome forms the 26s proteasome, that is responsible for recognition and degradation of ubiquitin-tagged proteins (Hershko and Ciechanover, 1998; Voges, Zwickl and Baumeister, 1999; Hershko et al., 2000). The PA700 itself is a unsymmetrical protein complex of \sim 20 proteins. Although there has been major efforts to unravel the structure of the PA700 molecule it has not finally been shown. Nevertheless there is good understanding about the composition and localisation of this protein complex (de Fonseca and Morris, 2008; Bohn et al., 2010; Bedford et al., 2011; Lander, Estrin & Matyskiela et al., 2012).

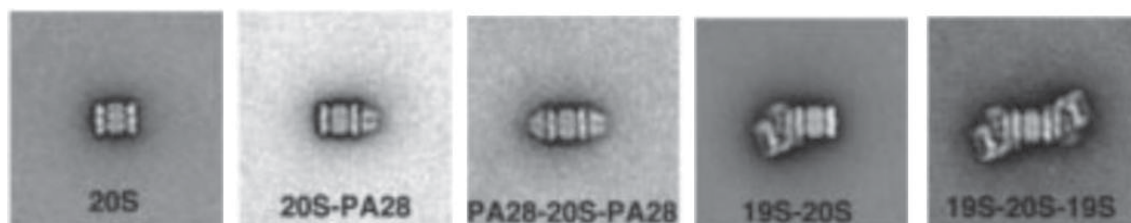


Fig. 1.6 20S particle with different regulators. PA28 and 19S particles can bind to the 20S core particle in different combinations. From PA28 single capped to 19s double capped complexes everything can be found in *in vitro* mixed samples (class sum images taken from Cascio et al., 2002).

PA28 on the other side does not regulate the 20S activity, but activates it. The activation mechanism is not well understood. The PA28 protein complex is comprised of seven copies of a PA28-alpha or PA28-beta subunit (Bochtler et al., 1999). Biochemical data suggests that there exist complexes that are single-capped and double-capped with PA28 (Shibatani et al., 2006). Nevertheless it seems as if there were more single-capped complexes than double capped ones. An EM study from *in vitro* mixed samples has shown that there are various kinds of complexes possible (Fig. 1.6): not only between 20S and PA28, but also between 20S, PA28 and 19s (Cascio et al., 2002).

However, the previously used components were not derived from a single organism, but generated by mixing recombinant components from two very different species. Another study revealed the crystal structure of a bactericidal PA26 (PA28 equivalent from procaryotes) double capped 20S *Trypanosoma* core particle (Whitby et al., 2000) (Fig 1.7). It showed for the first time interaction sites between the alpha subunits from the 20S core and PA28 molecules. Despite all efforts, the structure of a PA28-20S complex from the same organism has never been shown.

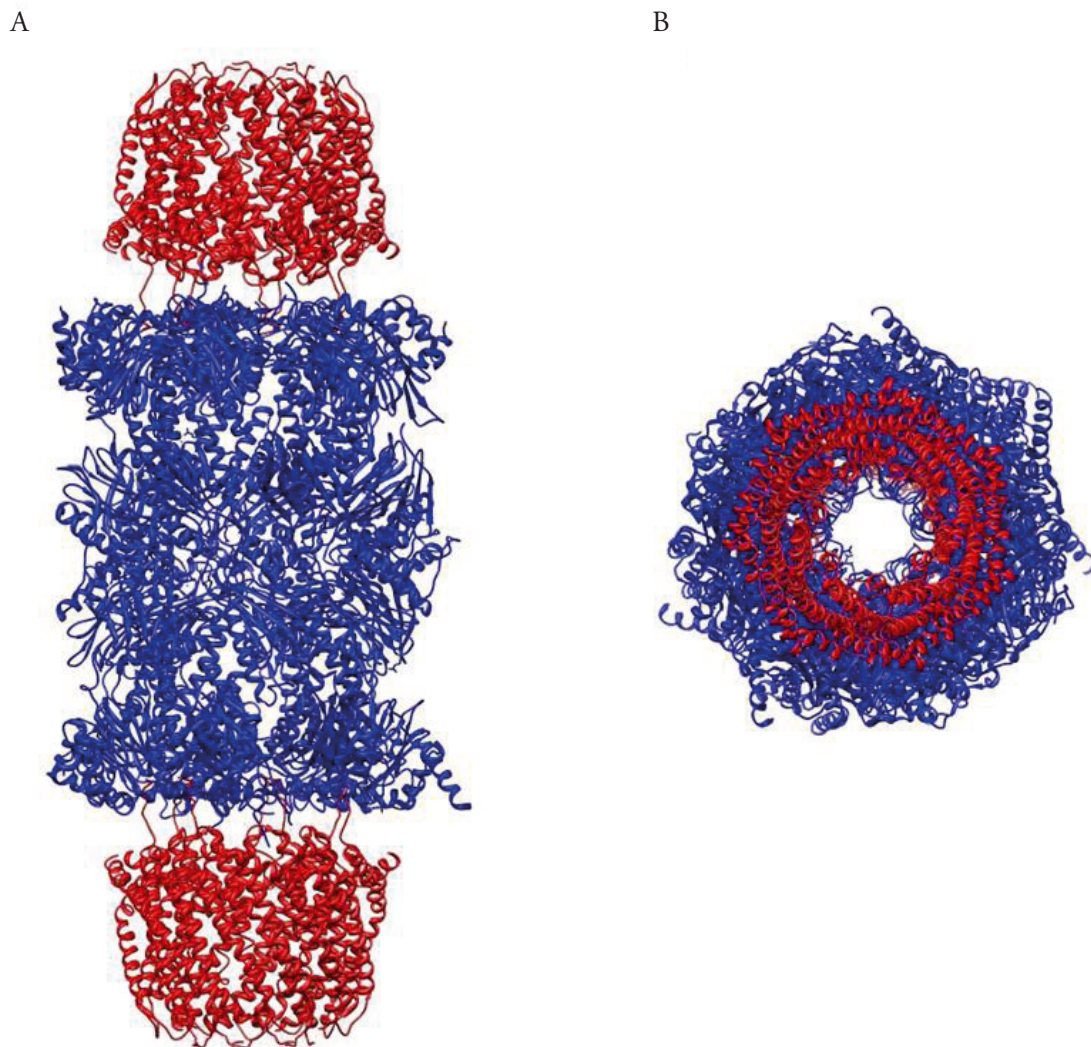


Fig. 1.7 Double capped 20S-PA26 complex. (A) Side view of a 20s (blue) complex with pa26 complexes (red) on both sides. Each pa26 binds to one alpha subunit. (B) Top view of the complex displays perfect heptameric symmetry of the pa26 complex. Nevertheless the entire complex only displays C2 symmetry.

1.5.3 Goal of this project

The goal of this project was to show, by 3D-EM, the structure of a PA28-20S complex purified from human blood. By single particle analysis a three dimensional model of the solitary 20S core particle itself and the PA28-20S complex should be produced. The proportion of single-capped and double-capped particles should be estimated, and the activation mechanism should be further elucidated.

1.6 The hepatitis B virus (HBV) capsid

The hepatitis B virus is a major threat to human health. With more than 350 million people being chronically infected worldwide it is among the most successful viruses. After infection an inflammatory response in the liver is observed, with 90% of the patients recovering. Currently, every third person carries antibodies against the virus stemming from a former infection (WHO: programs and projects: hepatitis B virus)(Fig. 1.8). The HBV carries a double stranded DNA which is located inside an icosahedral capsid. The capsid is surrounded by a membrane.

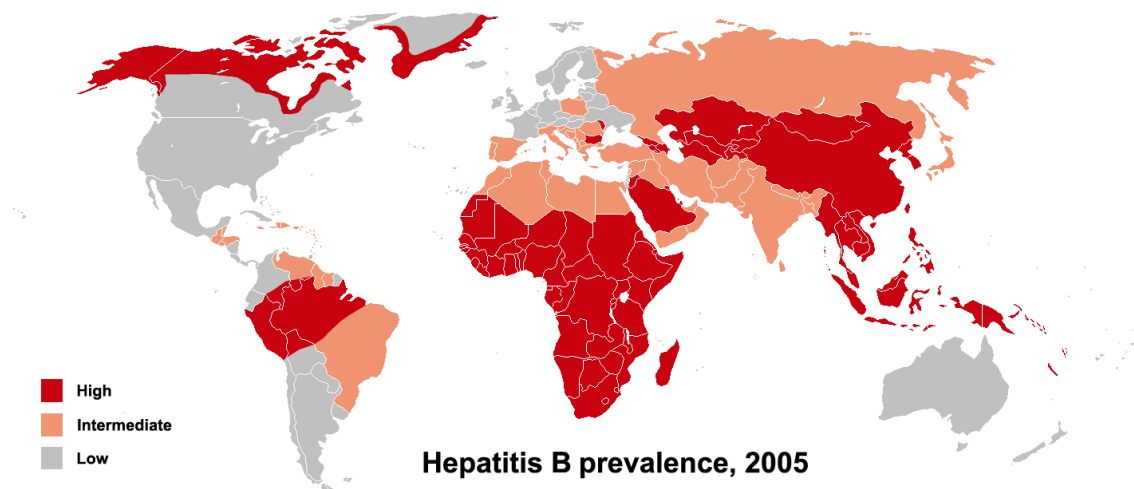


Fig. 1.8 Worldwide hepatitis B prevalence. In red are regions with high (>8%), light red medium (2%-7%) and grey low (<2%) prevalence of the HBV surface-protein antigen. (wikipedia:NPhillip)

1.6.1 Structure of the capsid

The icosahedral capsid of HBV is formed by a single protein subunit. Two monomers form a disulfide-bridged dimer. These dimers then form the capsid. The capsid itself occurs in two types, termed T3 and T4. The T3 capsid is formed by 90 subunit dimers whereas the T4 capsid contains 120 dimers. The atomic structure of a dimer was resolved at $\sim 3.3\text{\AA}$ resolution (Wynne et al., 1999). With the asymmetric unit present as two dimers forming a crystallographic tetramer. Previous studies have resolved the structure of a T4 capsid to subnanometer resolution by means of electron cryo-microscopy (Böttcher et al, 1997; Conway et al., 1997), showing that the protein exclusively consists of α -helices. The protein assembly in T3 and T4 is quite different; the arrangement of the different symmetry axes is visualised in Fig. 1.9.

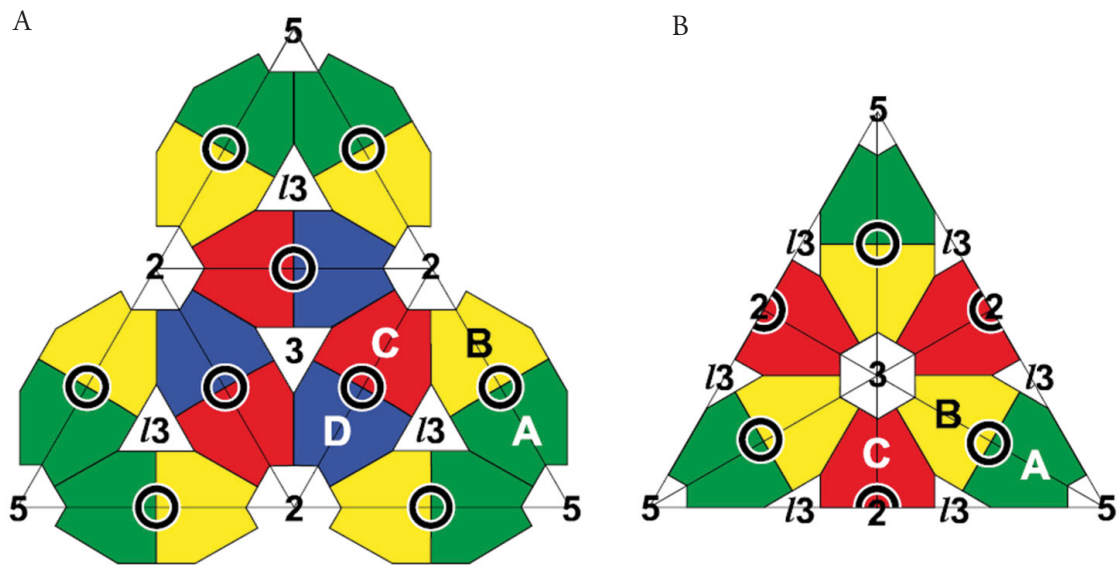


Fig. 1.9 Nomenclature of subunits in HBV capsids. (A) In the T4 capsid the principal subunit positions are termed A,B,C and D. Together they form the asymmetric unit of the core structure. (B) In the T3 capsid the principal subunit positions are termed A,B and C. The 5-fold axis of symmetry is formed by subunits A and B in both capsid types. The other symmetry axes (C2 and C3) are formed by partially different subunits. The symmetry axes are numbered according to their symmetry fold. The pseudosymmetry axis is termed 13. (Image modified from Roseman et al., 2012).

From the crystal structure of the subunit dimer some molecular interaction have been described that stabilize the monomer and the dimer. An important connection between the two dimers is the disulfide bridge between cysteines-61 (Fig. 1.10 (A) and (B) green residues). Moreover, a hydrophobic core is described to stabilize the monomer (Fig. 1.10 (C) red residues). Interactions between dimeric subunits involve arginine-127 were mutations to glutamine or leucine reduced the yield of intact capsids (König et al., 1998; Ponsel and Bruss, 2003). Furthermore, residues in helix $\alpha 5$ and the adjacent proline-rich loop are involved (Fig. 1.10 (B) black circles)(Wynne et al., 1999).

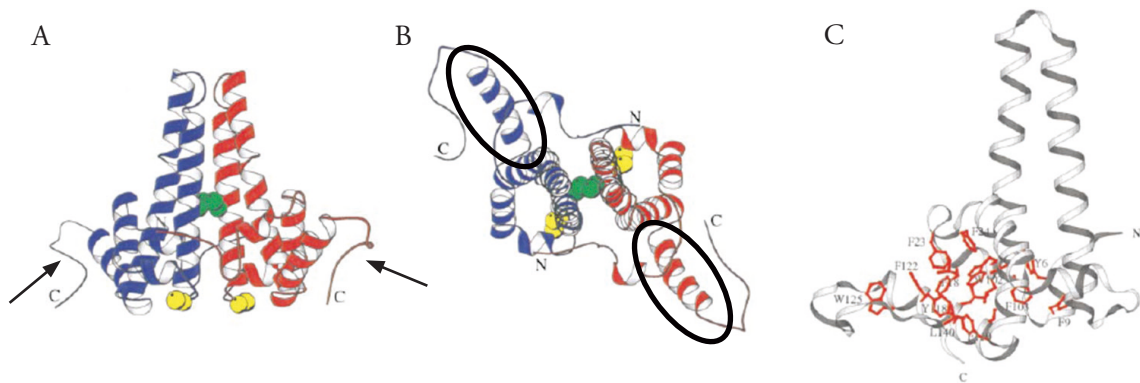


Fig. 1.10 Stabilizing structural elements in the HBV core protein. The dimer (A)(B) is mainly stabilized by a disulfide bond (green residues in (A) and (B)) formed by Cys-61. Cys-48 on the other hand is not involved in disulfide bond formation (yellow residues in (A) and (B)). Note the long C-terminal end adjacent to helix $\alpha 5$ (elips in (B)) and the proline rich loop (arrow in (A)). (C) The monomer is mainly stabilized by the hydrophobic core that is formed by a large number of hydrophobic residues (adapted from Wynne et al., 1999).

1.6.2 The HBV capsid as antigen carrier

As the capsid of HBV is highly immunogenic (e. g. Vanlandschoot et al., 2003) it is used as an antigen carrier. Usually the antigen of interest is inserted into the spike region and thus presented at an exposed position in a high amount of copies (240 (T4) or 180 (T3) per capsid). It has been shown that insertion of further gene products into this region does not affect the formation of capsids, but the capsids seem to have high plasticity (Roseman et al., 2012) (Böttcher et al., 2006), meaning that the structure displays a certain degree of flexibility. In cooperation with the group of Prof. Dr. Sahin (Medical Center of the JGU Mainz, Germany) our group has already performed 3D reconstructions of wild type (wt) and genetically altered HBV capsids (Klamp et al., 2011). The main question was to find out whether or not the inserted region shows a specific protein fold. As T4 capsids dominated the preparation, they were used for subsequent analysis. At a resolution of $\sim 10\text{\AA}$ all α -helices were clearly resolved, but the inserted region did not appear as a clear structure. Therefore it was assumed that the inserted peptide is highly flexible. Nevertheless, it appeared at the expected region of the capsid structure as unresolved extra mass (Fig. 1.11).

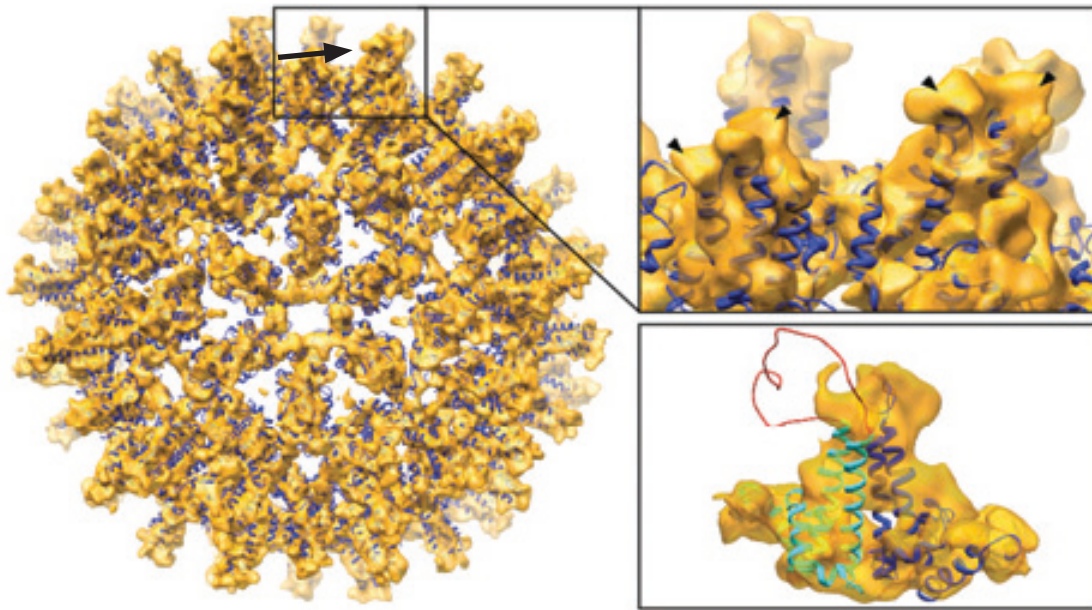


Fig. 1.11 3D reconstruction of a T4 HBV capsid. Automated docking of the crystal structure into the density map is possible. At the top of each spike structures (one marked with arrow), extra mass appears. Although this is the expected position of the inserted peptide it appears to be badly resolved. In the close up (bottom) the density map is shown with opacity and to demonstrate that the helices are well accounted for, but the mass at the top seems disordered (from Klamp et al., 2011).

1.6.3 Goal of this project

The present study was performed to resolve the T3 capsid to the same resolution as that of the published T4 structure (or better) and to see if there is a defined extra structure in the region of the inserted epitope. Moreover it was interesting to see if the structure of the spike itself was altered by the insertion of the epitope maybe even displaying a DNA/RNA filled state (compare Roseman et al., 2012). The last question to be answered was to look at the contacts between subunits and see if there are differences explaining the formation of T3 and T4 capsids.

2 Material and Methods

2.1 Animals

Astacus leptodactylus

Astacus leptodactylus (Eschscholz, 1823), a freshwater crayfish, is classified in the animal kingdom as follows

Arthropoda, Crustacea, Decapoda, Astacura, Astacidae.

At a size of 16-18cm (25cm max.) *A. leptodactylus* belongs to the largest freshwater crayfish. The colour ranges from dark yellow to brown and can partly even go towards green. As a habitat *A. leptodactylus* prefers warm and nutrient-rich lakes and slow flowing rivers in the flat lands. It is more tolerant towards muddy or polluted water than its close relative *Astacus astacus*. Therefore it is used in the food industry as primarily bred crayfish species.

We kept *A. leptodactylus* in large basins. Hemolymph (~300µl) was taken ventrally between the cephalothorax and the abdomen using a syringe.



Fig. 2.1 The freshwater crayfish *Astacus leptodactylus*.
(©wikipedia: Ulrich Mühlhoff)

Homarus americanus

Hommar americanus, (Edwards, 1873), better known as North American lobster, classifies in the animal kingdom as follows:

Arthropoda, Decapoda, Astacura, Homaridae

With a size of 20-60cm and weights from 0.5-4kg lobsters belong to the largest arthropods. Their main distribution area is the North American east coast from Labrador in the North to North Carolina in the South. It prefers shallow and cold water with rocky ground.

We bought the animal in a fish store (Fisch Jakob, Mainz, Germany). Hemolymph was taken by a syringe ventrally between the cephalotorax and the abdomen.



Fig. 2.2 The lobster *Homarus americanus*. (© wikipedia: U.S. Oceanic and Atmospheric administra)

Carcinus maenas

The shore crab *Carcinus maenas* (Linnaeus, 1758), is placed in the animal kingdom as follows:

Arthropoda, Crustacea, Decapoda, Brachyura, Protunidae

With a carapax width of up to 9 cm and a length of up to 6 cm *C. maenas* belongs to the larger crabs. Living in the littoral region of the sea with original habitats in the European north-east Atlantic Ocean and the Baltic Sea, it has colonized similar habitats around the world. As a predator *C. maenas* feeds on bivalve molluscs and crustaceans.

We obtained *C. maenas* from the island of Helgoland off the German coast. They were kept in 300l sea water aquariums, and hemolymph was taken at the coxal joints using a small syringe. 100-200µl were usually extracted.



Fig. 2.3 The shore crab *Carcinus maenas*. (© wikipedia: Hans Hillewart)

Odontodactylus scyllarus

The Peacock mantis shrimp *Odontodactylus scyllarus* (Linnaeus, 1758) has the following position in the animal kingdom:

Arthropoda, Crustacea, Stomatopoda, Odontodactylidae

The mantis shrimps are a group of ~400 species and separate into two groups according to their claw morphology. On one side there are the spearkers and on the other side there are the smashers. The spearkers possess appendages equipped with thin spear-like protrusions used to stab animals of prey. The smashers have thick appendages that they use to hit their animals of prey and thereby injure or kill them. *O. scyllarus* belongs to the spearkers. With sizes of up to 30 cm and a wide range of colors they belong to the favorite crustaceans in aquariums.

We received a sample of fresh and cell-free hemolymph from Prof. T. Burmester (University of Hamburg, Germany).



Fig. 2.4 The mantis shrimp *Odontodactylus scyllarus*. (© wikipedia: Jenny)

2.2 Protein samples

2.2.1 2x6meric hemocyanins

The hemolymph samples obtained from the animals were purified by centrifugation for 15 minutes at 4500g to remove the blood cells. To stop proteolytic activity the sample was treated with *Complete EDTA-free* (Roche, Mannheim, Germany), a protease inhibitor cocktail. According to the product description, one tablet was diluted with 2ml of H₂O_{dest} and then added to the sample at a concentration of 4μl per 100μl. Further purification of the samples was not necessary, as the main part of the hemolymph proteins was hemocyanin. Not only do they out-number the other proteins, but they are by far the largest. The protein concentration was assessed photometrically assuming that an absorption of 1OD at 280nm equals 1mg/ml. The apparent concentration was between 10 and 15mg/ml. For electron microscopy, samples were diluted to 0.1-0.05mg/ml.

2.2.2 HIV-Env proteins, CD4 and mABs

HIV-Env, CD4 and mABs were obtained from [\[1\]](#). They were delivered in different stock concentrations and were diluted to fit EM requirements. HIV-Envs were diluted to ~0.02mg/ml. With CD4 they were mixed in a ratio 1:1.2 and with mABs they were mixed in a ratio 1:3.

2.2.3 20S and 20S-PA28 proteasome complex

The 20S and 20S-PA28 proteasome complexes were purified from human blood samples by [\[2\]](#). They were delivered in stock solution at ~2mg/ml. Samples were diluted to ~0.1 mg/ml for negative staining electron microscopy.

2.2.4 Hepatitis B virus capsids

Recombinant HBV capsids were obtained from [\[3\]](#) as a stock solution of 2.4mg/ml and diluted to 1.2mg/ml for cryo EM images and 0.1mg/ml for negative staining EM. They were produced under GMP conditions.

2.3 Electron microscopes (EM)

A **Tecnai12** (FEI, Eindhoven, Netherlands)(Fig. 2.5) equipped with a LaB₆ electron source operated at 120kV was used to acquire negative stain images from Hc-2x6mers and the HIV-Env proteins. The spherical aberration of the microscope (Cs) is 6.3 and therefore it provides a very good contrast. As it was used for negative stain the high Cs value does not effect the resolution obtainable, as it is below the 15Å resolution achievable with negative staining.

A **TecnaiF20** (FEI, Eindhoven, Netherlands) equipped with a field emission gun operated at 200kV (The Scripps research institute, La Jolla, USA) was used for the proteasome samples. This microscope, with a Cs value of 2.3, was engineered for cryo-EM purposes. It has a cryo-cage, to prevent contamination of the specimen it operates under LEGINON (Potter et al., 1999)(Carragher et al., 2000) making it convenient to run long sessions.

A **Polara** (FEI, Eindhoven, Netherlands) equipped with a field emission gun operated at 300kV (MPI for Biophysics, Frankfurt a. Main, Gemany) was used for the HBV capsids cryo samples. With a Cs value of 2 and 300kV it provides very good contrast for the rather thick (50nm) sample. Moreover the samples are loaded from the top and they are detached from the outside during image acquisition making it very stable and drift resistant.

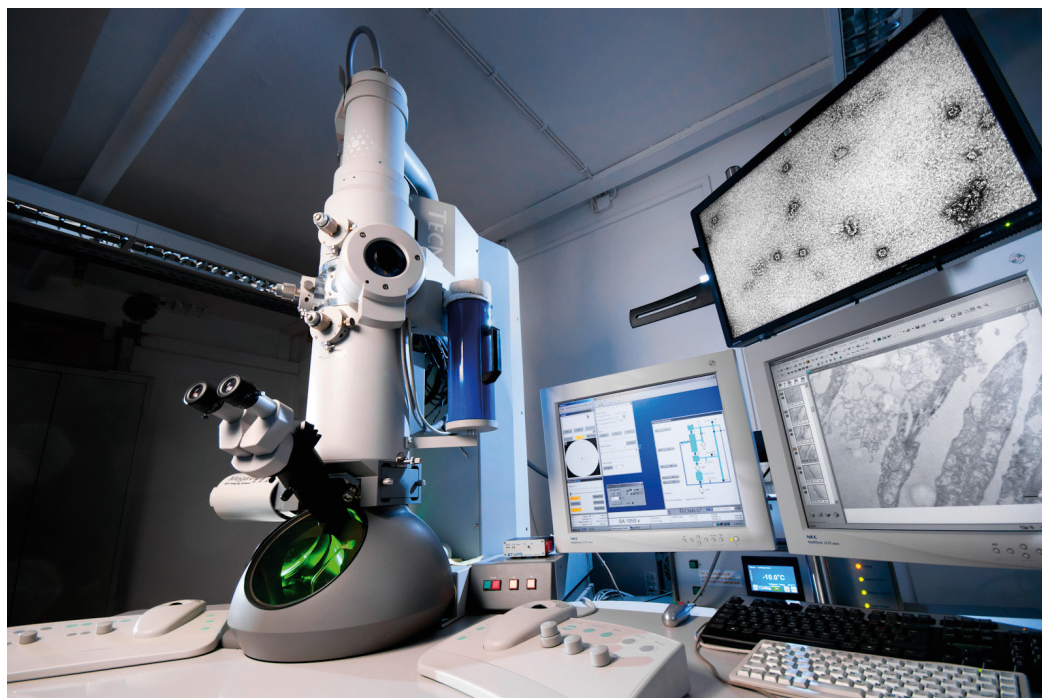


Fig. 2.5 Tecnai12 electron microscope. Operated at the Institute of Zoology at the JGU Mainz (Germany) (image courtesy of Christoph Kuehne).

2.4 Electron microscopic detection devices

A **MegaviewIII** (Olympus Deutschland GmbH, Hamburg, Germany) 1kx1k CCD camera that was operated under the Tecani12 microscope. The primary microscope magnification was chosen to have $6.4\text{\AA}/\text{pix}$ resolution on the camera. The camera was used for the 2x6mer project.

A **TemCam-F416** (TVIPS, Munich, Germany) 4kx4k CCD camera was purchased during my PhD time and mounted onto the Tecnai12 microscope. As it was mounted post column it has a post magnification of 1.46 with a pixel size of $15\mu\text{m}$. It was used to acquire images from the HIV-Env proteins and operated with a two times binned chip during this project for better contrast. To be able to make full use of the camera the magnification was chosen to have $4.36\text{\AA}/\text{pix}$ as the final resolution.

A **direct electron detector** (DED) (Direx, San Diego, USA) was used for imaging the proteasome samples. This detector quantifies the incoming electrons directly and they are not converted into photons first. This helps to detect lower electron dose and a smaller pixel size (here $8\mu\text{m}$) can be used as there is no point spread function present anymore.

Kodac SO-163 film was used to image the HBV capsids. After development of the negatives they were digitised using a Primscan 7100D (Heidelberger Druckmaschinen, Heidelberg, Germany) to a final resolution of $1.3\text{\AA}/\text{pixel}$. This means that the images were scanned with 3175dpi.

2.5 Computer hardware

Image processing was mainly performed on a 358 core AMD Opteron computer cluster (Fig. 2.7) purchased from Transtec AG (Tuebingen, Germany). This computer cluster allowed fast parallel processing of large data sets. As it was exclusively used in the 3D-EM group of

accessibility was excellent and the waiting times between the several image processing steps were reduced to a minimum. All nonparallel processes, such as modelling, graphical display or docking of crystal structures into density maps, were performed on a Intel Core2 Quad processor at 2.4GHz (4GB RAM) personal computer.



Fig. 2.6 Beowulf cluster at the JGU Mainz. A 358 core AMD Opteron computer cluster located at the Institute of Zoology at the JGU Mainz Germany (image courtesy of Christoph Kuehne).

2.6 Computer software

Appion is a server based database that connects different image processing packages and stores the results in a database. This makes data management very convenient and it is very easy to share projects and data with other researchers (Lander et al., 2009).

IMAGIC-5 is an image processing software package. It was designed to reconstruct single particles from electron microscopic images. The single steps necessary will be described later. The software was purchased from Image Science Software GmbH (Berlin, Germany) (van Heel and Frank, 1981)(van Heel et al., 1996)

EMAN1.9 is a free software package for image processing (<http://blake.bcm.edu/eman-wiki/EMAN/>). Its main focus is on single particle reconstruction of TEM images. As for IMAGIC-5 special functions are described later. (Ludtke et al., 1999)

CTFFIND3 is a computer program to determine the defocus values of electron microscopic images by comparing the experimental Thon rings (Thon, 1966) with theoretical ones. The defocus value is vital for CTF correction. CTFFIND3 is freeware and can be down-

loaded (<http://emlab.rose2.brandeis.edu>) (Mindell and Grigorieff, 2003)

ClustalX is a program that performs multiple sequence alignments of protein or DNA sequences. It provides a graphical user interface (GUI) and is available for free (www.clustal.org) (Higgins and Sharp, 1988) (Thompson et al., 1994) (Thompson et al., 1997) (Larkin et al., 2007).

EM-Menu and **EM-Tools** are programs to operate (EM-Menu) and automate (EM-Tools) the TemCam-F416 at the Tecnai12. Both programs were delivered with the camera from TVIPS (Munich, Germany).

GeneDoc is a displaying, analyzing and editing program for multiple sequence alignments. It is freeware and can be downloaded (www.nrbsc.org/gfx/genedoc) (Nicholas et al., 1997).

IMOD is a software package for reconstruction of tomographical tilt series from the electron microscope. It provides a graphical user interface and covers all steps from the initial alignment to the segmentation of the final reconstructed tomogram. It is free of charge and can be downloaded from <http://bio3d.colorado.edu/imod/> (Kremer, Mastronarde and McIntosh; 1996) (Mastronade, 1997).

Modeller is a program for comparative modeling of protein sequences based on a template structure. It uses previously aligned protein sequences of a protein with a known structure and a target protein of unknown structure to model the unknown protein onto the known structure. Modeller is free of charge and can be downloaded from the internet at <http://salilab.org/modeller/> (Sali and Blundell, 1993) (Fiser et al., 2000) (Eswar et al., 2008).

Swiss-Model is a web server based modeling program that is accessible to all users. It has different possibilities to offer. The easiest one is to provide it with a sequence and let it search for the best template by itself. For more sophisticated models one can provide a template or even a sequence alignment to be used. The server can be reached at <http://swissmodel.expasy.org/> (Guex and Peitsch, 1997) (Arnold et al., 2006).

Molprobity is a web server offering programs for quality assessment of atomically resolved structures. It offers analysis of all steric and angular properties of a model, whether from a real experiment or from a modeling approach. It is accessible to anyone over the internet and can be reached at <http://molprobity.biochem.duke.edu/> (Chen et al., 2010) (Davis et al.; 2007).

UCSF Chimera is a multi-modular program used to work with 3D protein structures regardless if atomically resolved from X-ray crystallography or low resolution models derived from electron microscopic images. It offers many functions such as docking of crystal structures into EM densities, segmentation of structures and many more. It is freely available for everyone at <http://plato.cgl.ucsf.edu/chimera/> (Pettersen et al., 2004) (Goddard et al., 2007)

2.7 EM grids

In principal all EM grids have the same basic architecture. They are composed of a solid support structure (mostly copper, but iron, gold and other metals are possible) that forms a mesh and a thin support layer above that is electron permeable. This layer is usually carbon, but there are new developments with silicon as well. This layer can now have different functions. In the case of continuous carbon grids the layer functions as support for the sample and the EM image is taken through it. In the case of holey carbon there are holes in this layer and the sample is kept in these holes in vitrified buffer for cryo-EM (Quispe et al., 2007) or a thin trehalose-negative stain film (Harris, 2008). To lower the influence of the carbon background it is possible to use holey-carbon-supported-thin-carbon grids. These are holey carbon grids with an additional thin layer of carbon on top. This thin layer of carbon would not be strong enough to cover a pure copper grid, but is able to cover the area of one hole without rupturing. This method is especially used if the sample is tilted within the microscope during tomography or random-conical-tilt (Radermacher et al., 1987) (Radermacher, 1988). Fig. 2.7 gives an example for the architecture of a holey carbon grid.

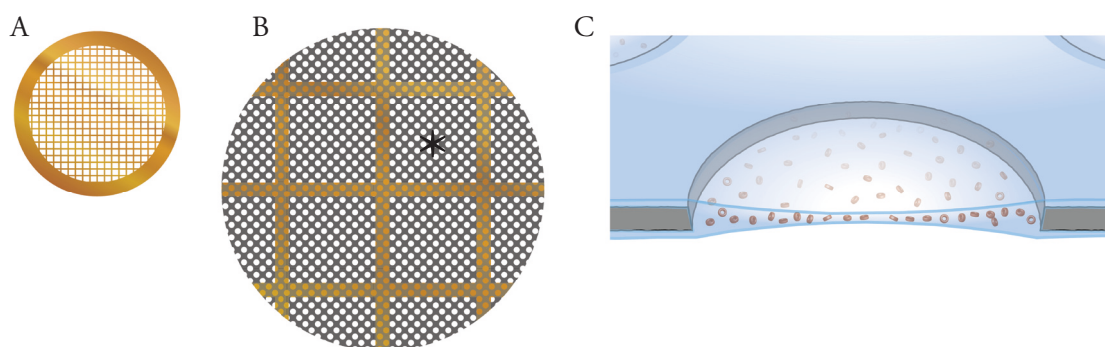


Fig. 2.7 Grid architecture. From left to right different magnifications of an EM grid are shown. Usually a grid is 3.05 mm in diameter (A) and different mesh sizes are possible. For the HBV capsids project 300 mesh grids were used. This means that there are 300 squares (marked with asterisk (B)) per grid. In (C) a vitrified sample is visualised (images courtesy of Christoph Kuehne).

2.8 Negative staining

2.8.1 Basic principles

To visualize proteins in the EM there are multiple possibilities of which two are regularly used. The first one is to vitrify them (stained or unstained) in a liquid environment (McDowell et al., 1983) and the second one is to negatively stain them with heavy atoms, dry them

and look at them at room temperature (Brenner and Horne, 1959). There are some heavy atom-containing salts that are routinely used for negative staining of protein samples. These are for example uranyl acetate, uranyl formate, ammonium molybdate, sodium phosphotungstate and sodium silicotungstate (Harris et al., 2001). Nevertheless it should never be forgotten, that resolution is limited by negative stain, but contrast is enhanced. This is extremely helpful for small and/or flexible assemblies (e. g. Burgess et al., 2004) or time resolved visualization of macro molecular complexes (e.g. Mulder et al., 2010). Negative stain cannot be used if resolution below 15-20Å is required, as this is the resolution limit (Ohi et al., 2004). Nevertheless it is of great use for all questions that can be answered at this resolution, as it is fast to prepare and subsequent image processing is mostly easier compared to images from unstained vitrified samples.

The goal of a negative staining procedure is to fully cover a protein sample in a heavy atom environment. To achieve an optimal result for image acquisition in the EM it is necessary to receive an evenly thick staining layer with an equal protein distribution on the grid (Fig. 2.8 (D)). As shown in Fig. 2.8 there are some results possible that do not resemble a perfectly stained sample. This might be due to partially embedded proteins in stain (Fig. 2.8 (A)), a stain gradient within an image or a local stain gradient around the single proteins (Fig. 2.8 (B)).



Fig. 2.8 Different staining results. (A) Protein samples are not fully embedded in stain. As a result the protein information is incomplete and a trustworthy reconstruction is not possible. (B) The protein is fully embedded. Nevertheless there are differences in the stain thickness and distribution. The result could be a stain gradient or no clear contrast between the proteins and the background. (C) Perfectly embedded sample. This results in light particles and a dark background.

2.8.2 The stain solutions

In my studies I used 1% uranyl acetate and 2% uranyl formate for negative staining. The uranyl acetate solution was kindly provided by _____ and the uranyl formate solution was produced by myself (appendix).

2.8.3 The single droplet method

This method (Harris, 1969)(Harris, 1991)(Harris, 1999)(Harris, 2007) uses an hydrophobic surface (e.g. Parafilm,) as layer for the solutions. For the Hc-2x6mers this method was used for staining and a protein concentration of $\sim 0.1\text{mg/ml}$ was used. At first the sample was picked up with the carbon side of the grid and the sample was given a 10sec incubation time. Then the grid was washed three times with the H_2O dest and the droplet was taken from the grid with a filter paper (e. g. Whatman No1). Then the stain solution was again picked up with the carbon side and another 10sec incubation time was given. Then the stain solution was removed from the side of the grid with filterpaper again and the grid was air dried for several minutes (5min at least). Fig. 2.9 shows an typical setup of this method.

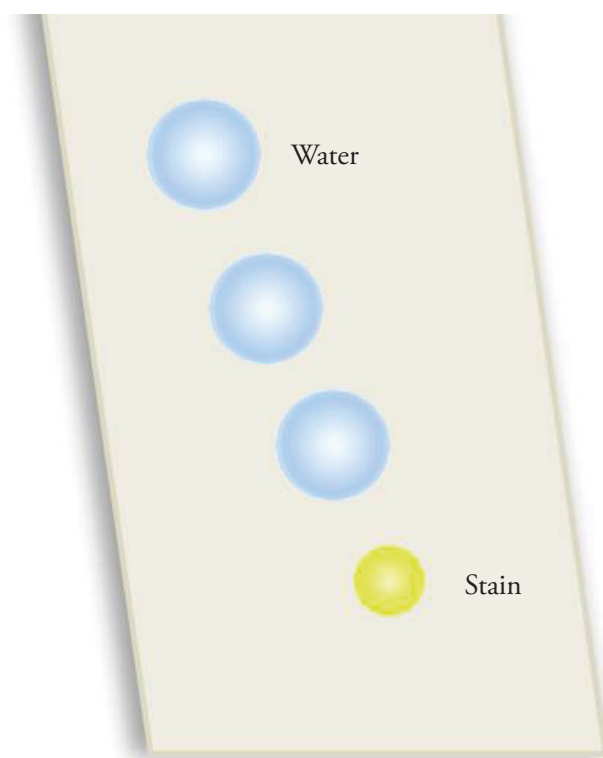


Fig. 2.9 The single droplet method. The sample is adsorbed to the carbon support film and then washed with water ($\sim 20\mu\text{l}$, blue) multiple times (1-3). Afterwards the surplus liquid is removed with a filter paper and the stain solution is applied on the grid ($\sim 5\mu\text{l}$, yellow). After a given time period (e.g. 10sec) the stain solution is again removed and the sample air dried.

2.8.4 The Teflon block staining method

This method does not make use of a hydrophobic surface, but all steps of the staining process are transferred to a plastic block. As seen in Fig. 2.10 this block has holes of different size and depth. The smaller ones (4mm diameter; 2mm deep) take the sample solution (~20 μ l) and the bigger ones (5mm diameter; 4mm deep) the staining reagent (~110 μ l). The advantage of this method is that the sample concentration is unimportant for the stain procedure as the sample is put into the holes and the grid can then be placed on top of it. It can sit there for several hours or even over night, to allow protein attachment to the carbon surface. After incubation with the sample the grid is placed on the stain solution, which forms an even surface on one of the bigger holes. After removal of the grid there is an even stain result on the grid and there is no supernatant that has to be removed. This leaves the protein untouched and there is no danger of artefact formation from this point of view. As all the samples I used had high enough concentration, they were applied to the grid directly and the grid was then put on the even stain surface for staining. In the case of the HIV-Env proteins a staining time of 30 seconds was found to be best and for the proteasome samples two minutes produced the best results.



Fig. 2.10 Block staining. The smaller holes take the sample solution and the bigger ones take the staining reagent. At first the grid is placed on the sample and in a second step the grid is placed on the stain. The individual times have to be tested for sample concentration and stain result.

2.9 Preparation of unstained vitrified samples

The vitrification of specimens is not trivial (Dubochet and McDowell, 1981) (Dubochet et al., 1982). The formation of ice crystals is highly dependent on the freezing rate with which the sample is frozen. Under perfect conditions samples up to 20 μm thickness can be frozen at sea level pressure (Cryo-EM of vitrified samples, Book). The goal of a perfect sample preparation is to obtain thin vitreous water with an equal sample distribution. Having more protein particles is not only convenient, because one needs fewer images it also helps with later image processing, especially CTF estimation (see 2.10.2), but overloading has to be avoided. As shown in Fig. 2.11 it is not only sample dependent whether the preparation is successful, but it depends on many things. As both specimen grids were produced with the same sample on the same day and handled in the same manner there must still have been a difference in the process as one sample shows heavy ice contamination.

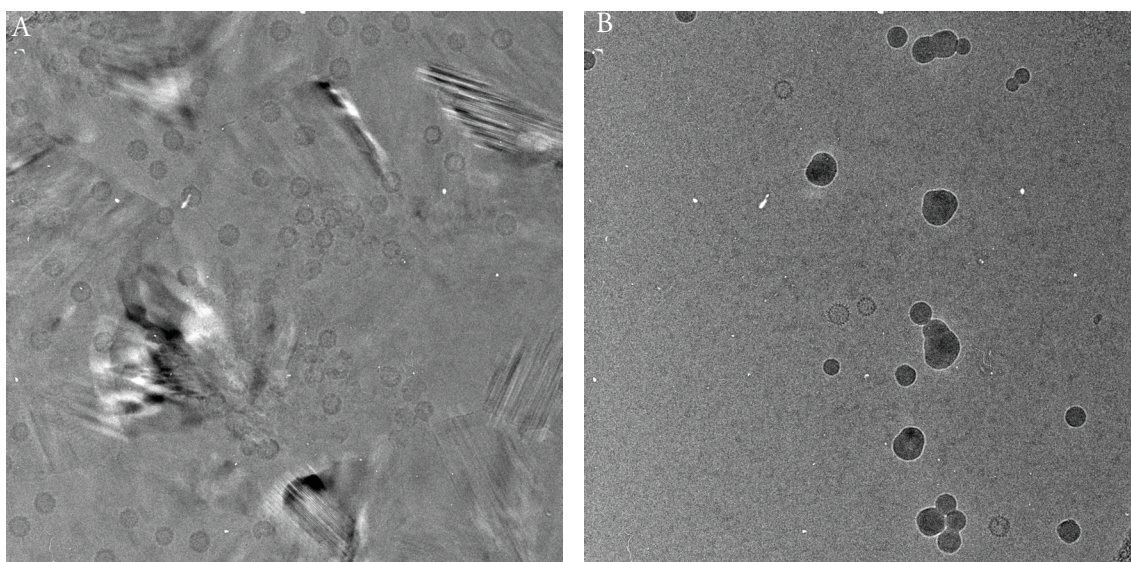


Fig. 2.11 Ice quality of vitrified samples. (A) Ice crystals (arrow) formed during sample preparation or handling. Although there are proteins (HBV capsids) visible, this sample can not be further used as the crystals may deform the protein structure, but would certainly impair later image processing. (B) Protein complexes can be seen and the ice quality is much better, still there are some impurities (black spots).

Normally the samples are plunge-frozen in liquid ethane or propane because their heat capacity is low enough to freeze the samples at the required speed. To keep the ethane liquid it is cooled using liquid nitrogen. To standardize the preparation of vitrified samples to a certain level companies developed plunge freezing machines. The one used in our laboratory is called CP3 (Gatan, Munich, Germany) with in-house modifications (Fig. 2.12). These modifica-

tions allow to control of the atmosphere throughout the entire preparation process. This is important for proteins that are sensitive to changing amounts of oxygen (e.g. hemocyanins). Nevertheless there are plunge freezers available from other companies (e.g. FEI or Leica), too. At the end all follow the same protocol. At first the sample must be applied to the grid. Then the surplus sample is removed during the blotting process. The blotting has a large impact on the later result. If the blotting time is too long there is no more sample in the holes and if the blotting time is too short there is too much sample and ice crystals form. The advantage of automated plunge freezers over manual blotting is the exact blotting time that can be adjusted. This should lead to a higher reproducibility of the obtained results.



Fig. 2.12 Gatan plunge-freezer CP3. The CP3 as it was used in our laboratory. The displays show ethane temperature, relative humidity and current blotting time. The entire procedure is under controlled atmospheric conditions (image courtesy of Christoph Kuehne).

2.10 Image processing methods

2.10.1 Particle selection

Prior to image processing particles have to be singled out (picked) from the acquired EM micrographs. This is done by cutting out boxes of appropriate size around the molecules. Different programs were used during my PhD. These include manual selection tools as well as automated or semi-automated ones. Manual selection was performed using *boxer* (Ludtke et al., 1999) and the *manual picker* implemented in Appion (Lander et al., 2009). (Semi) automated selection was performed using *boxers* autobox option or *DOG picker* (Voss et al., 2009) and *template picker* (Lander et al., 2009) both implemented in Appion.

2.10.2 CTF correction

During data acquisition in the EM the image function is convoluted with a point spread function (PSF) within the objective lens system. This results in the modulation of the image function around the x-axis and is dependent on different factors (e.g. defocus and Cs). This modulation becomes obvious in the fourier transform of the image and the areas of positive values become visible as Thone-rings (Thon, 1966). The convolution of the image function and the PSF is called contrast transfer function (CTF). If the CTF is not corrected and images with different CTF are combined the amount of information is limited to the first root of the function all other information will be averaged out. To correct for the CTF one has to determine the root positions for all images and multiply the negative values with -1. This will transfer the image information that became negative values during convolution, to the positive side of the x-axis and make it valuable for subsequent image processing.

In the presented studies FindCTF2D (unpublished programm from the group) and CTFfind3 (Mindell and Grigorieff, 2003) were used.

2.10.3 Bandpass filtering

Bandpass filters (Fig. 2.13) are applied to the reconstruction process to exclude information above and below certain resolution levels from the reconstruction. This helps to exclude e.g. noise from the reconstruction process. A bandpass filter is always a combination of a low-pass and a highpass filter, and can be described as a Gaussian filter. Nevertheless it provides independent low pass and high pass value adjustment. The filter values have to be adapted throughout the reconstruction process as high frequency information is normally excluded at the beginning of a reconstruction.

The resolution can be measured from the fourierspacetransform of an image. As the information is displayed inverse in Fourier space, the highest frequency information can be found at the edge of the transformed. The highest frequency information displayed there is the Nyquist-frequency. This frequency is described by $\frac{1}{2 \cdot \text{pix}}$. To filter a data set to a certain resolution the filter value can be easily calculated with: $\frac{\text{Nyquist}(\text{\AA})}{\text{resolution}(\text{\AA})}$. High pass filter values are under debate and a general value cannot be given. To highpass filter a reconstruction is referred to as “sharpening” within the community. Nevertheless there is a possibility to calculate a B-factor (Rosenthal and Henderson, 2003) thus enhancing higher frequencies. This leads to the emphasis of finer details in the 3D density map. Nevertheless this program only works properly if resolutions below 10Å are reached. If the reconstruction is over-sharpened, meaning to much low-resolution information is filtered away, artefact formation is possible.

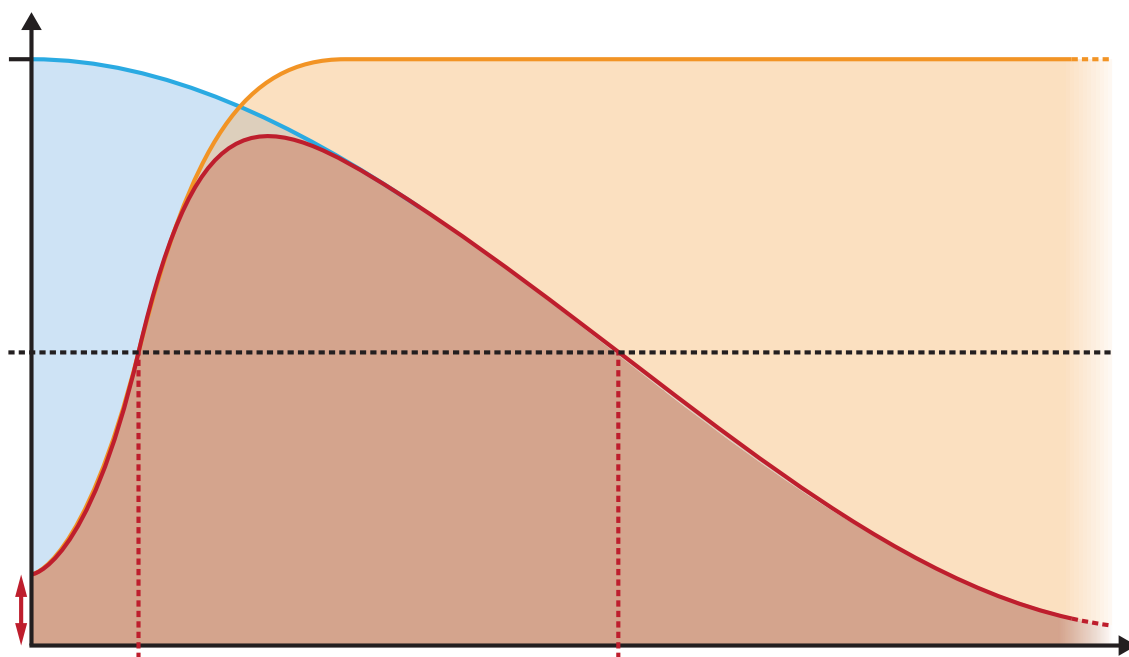


Fig. 2.13 Bandpass filter. A bandpass filter consists of a high-pass filter (orange) and a low-pass filter (blue). Together the resulting filter is a bandpass filter that restricts the information to certain frequencies. It is used to eliminate low frequencies that describe very coarse structures above the molecular information (high-pass filter) and to eliminate high frequencies (low-pass filter) describing structure features below the resolution level. The high- and low-frequency cut off describes the point where a certain spacial frequency drops to 0.5 of its original value. (Image courtesy of C. Kühne Uni Mainz)

2.10.4 Particle alignment

During the alignment the particles are shifted (translational alignment) and rotated (rotational alignment) with respect to a reference. However the first alignment during a reconstruction process is always reference free and centers the mass of each particle to the center of the image plane.

To perform a translational image alignment all images and references are transformed to Fourier space (this holds true for cross correlation methods, maximum likelihood will not be described). The transformed images are then multiplied and the resulting cross correlation function (CCF) (Saxton and Frank, 1977) is back transformed. In the resulting real image a peak is visible. The vector from that spot to the center of the image describes the translation needed to become the best overlay between the images compared.

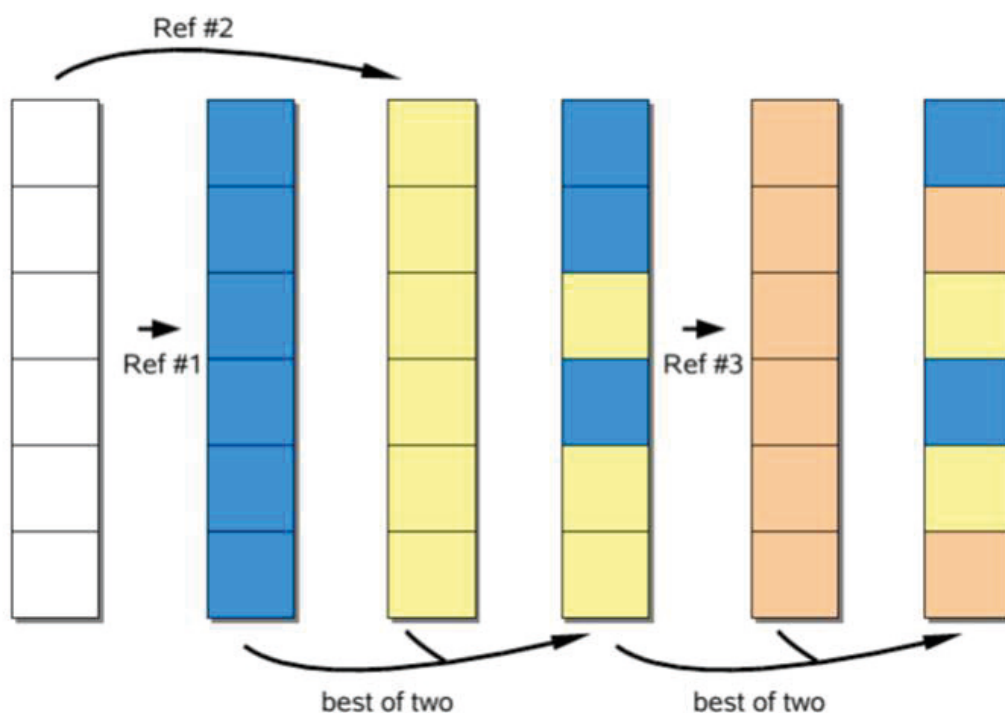


Fig. 2.14 **Multy-reference-alignment (MRA).** In a first step all single particles are compared to all references and the cross correlation value is stored. Then all single particles are compared to the second and if a better cross correlation value is found it is updated for the respecting image. At the end all single particles are individually assigned to the reference with the best cross correlation value.

To perform a rotational alignment images and references are transferred to a polar coordinate system. Then they are 1-D Fourier transformed and multiplied. After revers-transformation one or more spots (symmetrical particle views) are visible. From the polar coordinate the rotation angle can be seen. Fig. 2.14 shows how particles and references are compared.

2.10.5 Multivariate statistical analysis (MSA)

Once particles are aligned, similar views of the molecule have to be found. This is necessary, because similar views are summed up to increase the bad signal-to-noise ratio (SNR). This bad SNR comes from the fact, that biological samples are very beam sensitive and electron doses used are rather low ($\sim 20e/\text{\AA}^2$). One statistical method that is used to find similar orientations within the dataset is the MSA.

In a first step all images are projected into an n-dimensional hyperspace (n=# of pixels within the image). Therefore each pixel from each image is projected along adjacent axes with the respective grey value defining the length of each axis. This means that pixel number one is projected along the x-axis, number two along the y-axis, number three along the z-axis and so on. The result are n-vectors that can be described by one vector from 0,0,0. To reduce the amount of information a new vector space is spanned. The first axis of this space is described by the largest distance found between two spots in hyperspace, as this is the biggest difference in the data set. The second vector is orthogonal to the first one and describes the second largest differences found. The more vectors are used the finer differences can be described. Nevertheless the more vectors are used the more CPU time expensive it is.

The next step is a hierarchical ascendant classification (HAC) (Fig. 2.15). Once the desired amount of new vectors are defined (three at least) the distances between the image spots are calculated. The points are now organized in a manner to receive small intra-class distances and large inter-class distances. The result can be displayed tree-like and the amount of classes defined by the user determines how many branches are grouped into one class. The last step of the classification process is the summation of all images grouped in the same class (Simes, 1994)(van Heel et al., 2000)(Ward et al., 1983)(Schatz et al., 1990).

The MSA is not only good for classification of homogeneous data sets, but it can be used to separate particles with different structural features (van Heel, 2000).

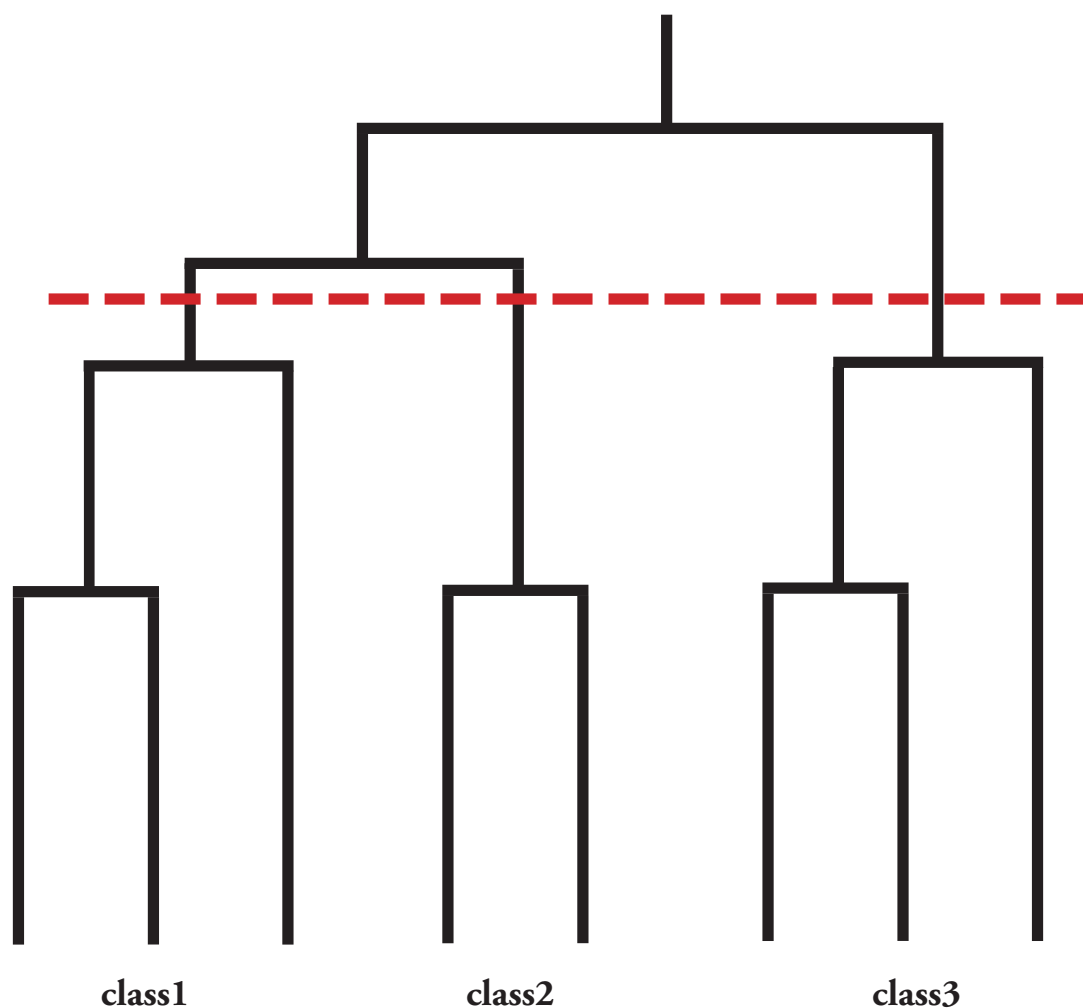


Fig. 2.15 Hierarchical ascendant classification (HAC) tree. Example of a HAC tree with the red line indicating the level where single particles are separated into different classes (modified from Schatz et al., 1990).

2.10.6 Orientation determination

To determine the orientation of the generated class sum images in 3D space the “euler angles” have to be determined. These angles describe, together with the translational vectors, the exact orientation of each class sum image. The “euler angles” are α , β and (γ). The α -angle is the in plane rotation angle of the class sum image and in the ideal case all images contained in a class sum have the same rotation angle as it is determined and adjusted during the rotational alignment. The β -angle describes the tilt angle of the molecule. A β -angle of 0° describes the view along the c-symmetry axis and a β -angle of 90° describes a view perpendicular to the c-symmetry axis. The (γ)-angle is an out of plane rotation angle that describes orientations with the same β -angle, but with different α -angles (e.g. Heyman et al.,

2005). Fig. 2.16 displays the different angles and axis that have to be determined for every class sum image and therefore for every single particle.

2.10.6.1 Orientation determination for single particles

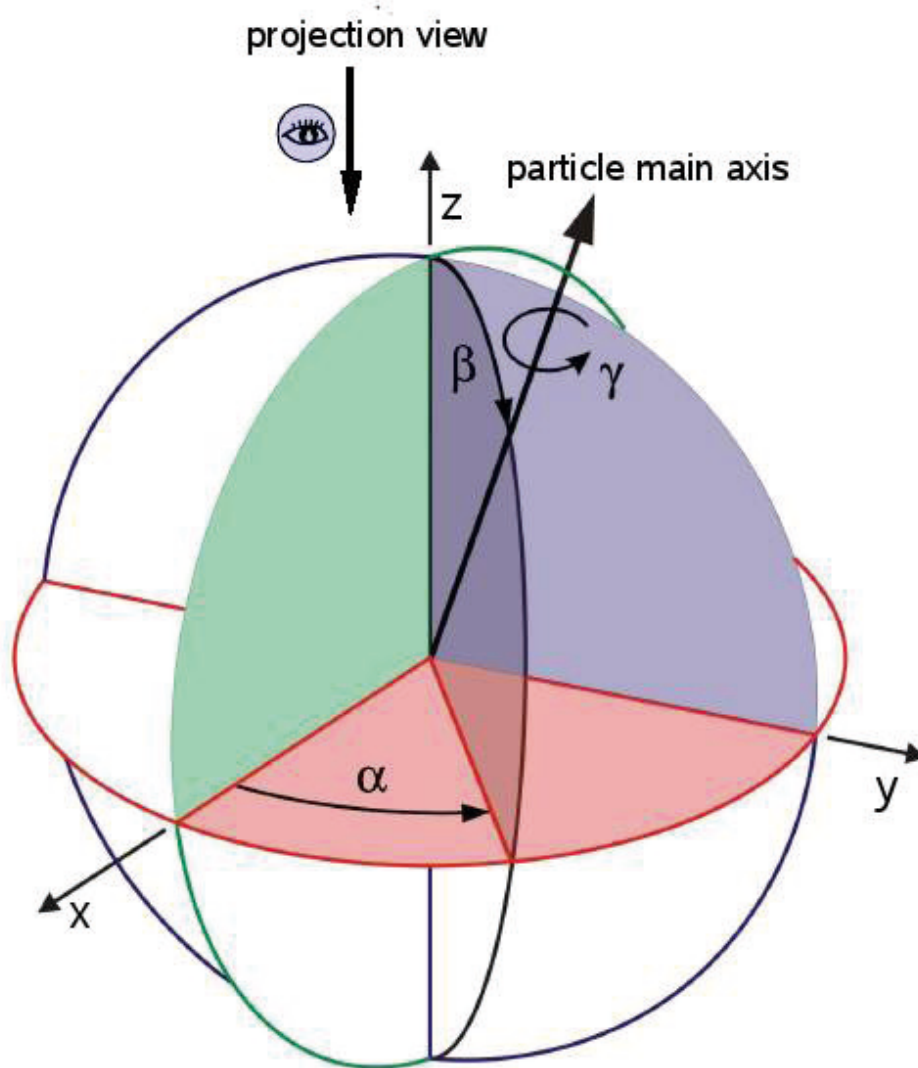


Fig. 2.16 Euler angles representation. Distribution of the different angles and axis within 3D space. The z-axis normally represents the main symmetry axis and a view along this axis is then called “top view”. The x-or the y-axis describes the secondary symmetry axis and a view along these axes is called “side view”

To determine the orientation of different class sum images without any further information on their 3D orientation is rather difficult. To solve this problem the common line projection theorem was developed (Kiseler, 1968) (van Heel, 1987). This states that two 2D projections of the same 3D object always share one common 1D projection line.

This theorem is implemented in the IMAGIC-5 software (module *angular-reconstitution*) and requires for asymmetric particles (normally all particles at the beginning) at least three different class sum images displaying three different angular representations of the molecule. Then these three class sum images are transferred into sinograms. Then two of these sinograms are correlated and the position with the highest correlation coefficient determines the angular relationship between the corresponding class sum images. The third sinogram is then compared to the other two and “fixes” the three class sum images in 3D space. For asymmetric particles there is always one correlation peak between two sinograms for higher symmetry structures there are multiple correlation peaks. In the case of the proteasome (calculated with C7 symmetry) for example there are seven correlation peaks, describing the heptameric symmetry. Adding a new class sum image to the set of class sum images is performed over all possible angles within the asymmetric triangle (Schatz et al., 1995).

The asymmetric triangle describes the region of the entire sphere that is unique within the reconstruction. For the proteasome this region is for example from the $0^\circ, 0^\circ, 0^\circ$ top view to the $0^\circ, 180^\circ, 0^\circ$ bottom view and covers $\sim 51.5^\circ$ around the equator.

The first 3D reconstructed model from these class sum images can then be used to create re-projections with defined Euler angles. These re-projections can then be used as references for further orientation determination (anchor set in *angular-reconstitution* from IMAGIC-5) (Schatz 1995) (Serysheva et al., 1995). The advantages of an anchor set are the exact knowledge of each angle, the higher SNR and the perfect consistency with each other.

2.10.7 Projection matching

In later stages, after the creation of a reliable initial model, it is possible to use the projection matching approach to determine the orientation of single particles. Therefore re-projections from a reconstructed structure are generated and the single particles are aligned against these using m-r-a. Therefore the re-projections act as references for the alignment procedure. Then all images aligned to one reference are summed and the angle of the reference is given to the new class sum. All class sums are 3D reconstructed and the new 3D structure is then again re-projected. To enhance the resolution of the reconstructed model the angle of the re-projections is lowered and therefore more and more views are available (van Heel, 2000).

Different image processing software packages have different options for projection matching. In EMAN projection matching is already implemented and can be easily used with the

refine option. IMAGIC5 on the other hand is rather modular and there is no automated refinement implemented. Therefore a script was generated (Mario Dejung, JGU, Mainz) that removed all unoccupied class sum images (grey picture) prior to the 3D reconstruction process. Meanwhile a command was implemented (remove-zero-images in *ex-copy* from IMAGIC5) that allows to perform projection matching in IMAGIC-5 without external scripting or programs.

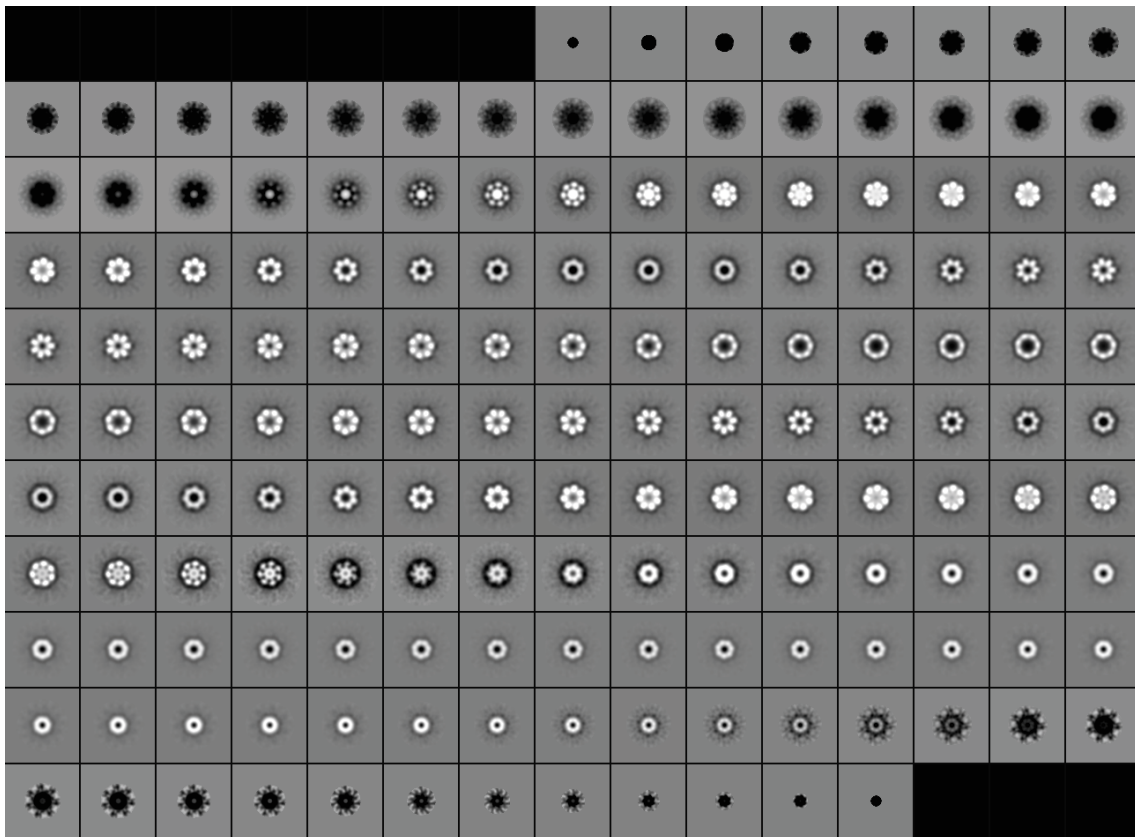


Fig. 2.17 Slices through a 3D volume. Slices through a volume of the 20S-PA28 complex from the bottom, (upper right corner) to the top (lower left corner). Note that there are 168 slices as the single particle dimensions were 168x168 pixels. The presence of black slices at the top and the bottom indicates that the box size was chosen right as there is no mass reaching out of the volume.

2.10.8 3D reconstruction of class sum images

After the formation of class sum images and the orientation determination of these, they have to be combined into one 3D object. This process is described as three-dimensional-reconstruction.

During this procedure the 2D class sum images are back projected into 3D-space and filtered. Therefore this process is called “exact filter back projection” (van Heel and Harauz, 1988) (Radermacher, 1988(Schatz et al., 1995).

The class sum images are projected into a 3D- space with the size corresponding to the number of pixels in each direction (x and y) and a z-height of the same value (for the proteasome 168 pixels in each direction). After the formation of these “3D pixels” they are referred to as voxels. To avoid the domination of certain spacial frequencies by overpopulated class sum images, all class sum images are filtered and basically normalised against each other. This helps to avoid the domination of the later 3D model by eventually preferred views.

After the projection of all class sum images available into the 3D space the grey values resting in every voxel are averaged out and this value is then assigned to it. Fig. 2.17 displays the section through the proteasome model displaying the different layers of the model. Each layer has a thickness of 2.14Å. To increase the resolution of the individual slices a finer Å/pixel value has to be chosen for the original single particles.

2.10.9 Refinement as an iterative process

As described in the previous paragraphs many of the methods used for single particle reconstruction depend on references and compare data, to enhance the quality of the output. Therefore it is important to understand the processes starting with the multiple-reference-alignment up to the final reconstruction as part of an iterative process that is highly interdependent (see Fig. 2.18). For different molecules different numbers of cycles have to be calculated (for the proteasome ~100) until the model is stable and no further improvement is seen in resolution.

2.10.10 Resolution determination of the reconstructed model

To assess the resolution of a reconstructed model a Fourier-shell-correlation (FSC) has to be calculated (Harauz and vanHeel, 1986) (Orlova et al., 1997). Therefore the class sum images available are split into two individual data sets and a 3D reconstruction of both is performed. The FSC then measures in dependency of the spacial frequency the normalised correlation between both models.

The spacial frequencies are displayed reciprocal and there are different criterion at which the resolution can be read. The 0.5 criterion for example measures the value at which the correlation has dropped to 50%. But there were more criterion introduced. The 3σ -criterion (Orlova et al., 1997) or the 1/2bit-criterion (van Heel and Schatz 2005). These measure the intersection between the individual criterion curves and the assessed FSC.

2.10.11 Filtering and 3D masking

To remove the noise around the reconstructed models for better visualisation it is possible to apply a 3D mask to it. Therefore the reconstruction is multiplied with a mask, leading to the result that all parts inside the mask are multiplied with one and all parts outside the mask are multiplied with zero. It is important to apply a Gaussian filter to the mask to prevent sharp edges, that would cause distortions within Fourier space. On more thing that can be done to a 3D reconstructed model is to filter it to its actual resolution. This helps to reduce artefacts and only structural features are displayed expected at the resolution. Therefore the model is low-pass filtered and all frequencies describing information above a certain resolution are omitted.

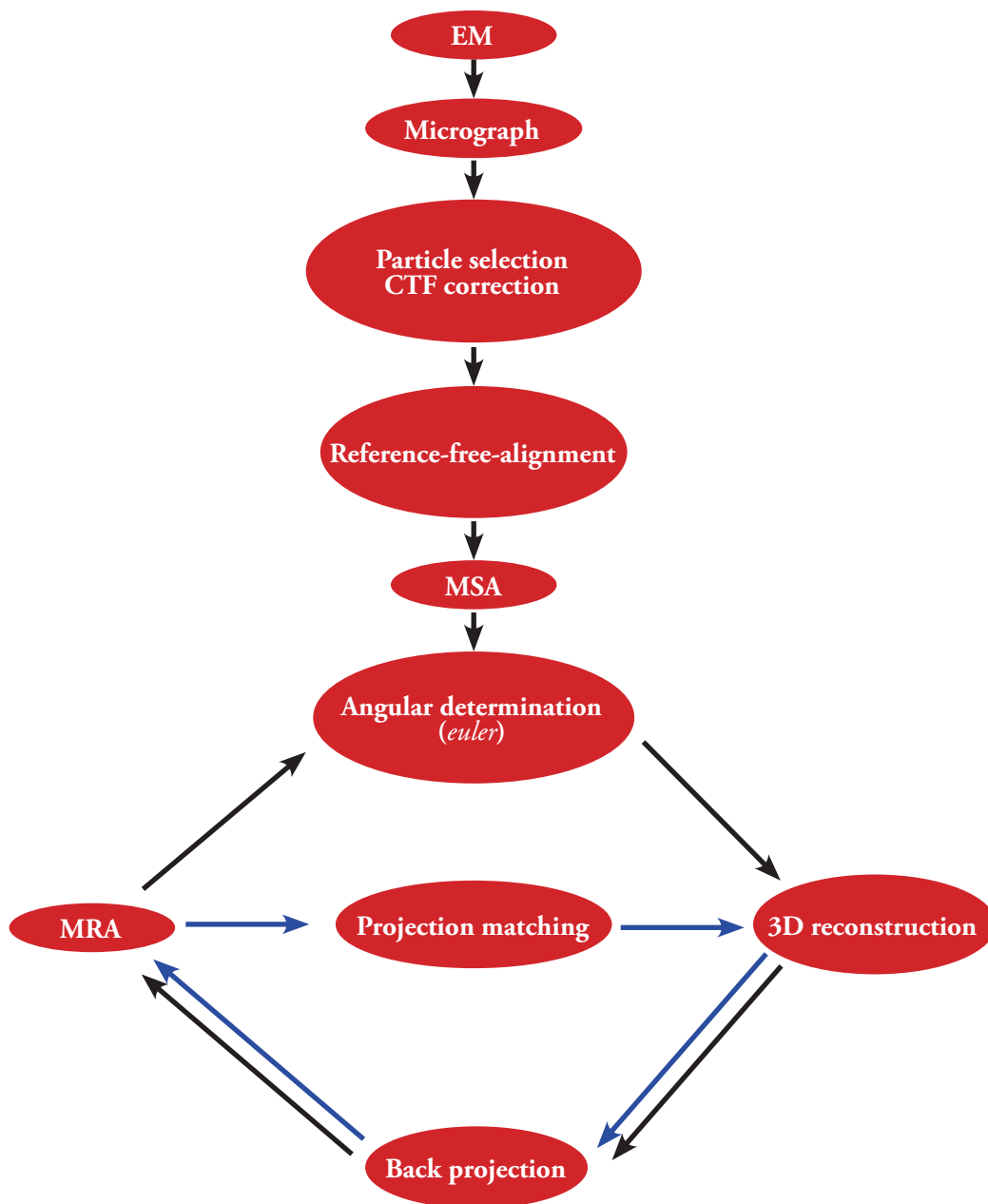


Fig. 2.18 Iterative refinement process. The process of single particle reconstruction starts with the acquisition of micrographs of the protein sample in the EM. Then the single particles have to be selected and the CTF has to be determined and the images must be corrected for it. After a first reference free alignment were the particles are mass centred they can be statistically sorted using MSA. After the summation of all images belonging to one class angles can be assigned to the best class sums and a first 3D reconstruction can be calculated. The back projections of this reconstructed model can then be used for quality control (comparison to the original class sum images) and as references for MRA. After MRA there are two possibilities for angular assignment. Either the angles are assigned via the sinogram correlation method or through projection matching. Both cases, nevertheless resemble the last step of this iterative process and the cycle starts again. The black arrows follow the reconstruction part from the beginning and the blue arrows resemble the short projection matching loop.

3 Results

3.1 Crustacean 2x6mer hemocyanins

The 2x6mer hemocyanins from the three decapods *Astacus leptodactylus*, *Carcinus maenas* and *Homarus americanus* are comprised of two hexamers which are rotated with respect to each other. In Fig. 3.1 the development of a 3D reconstruction from the raw-image to the final model is presented for *Astacus leptodactylus* hemocyanin AleHc.

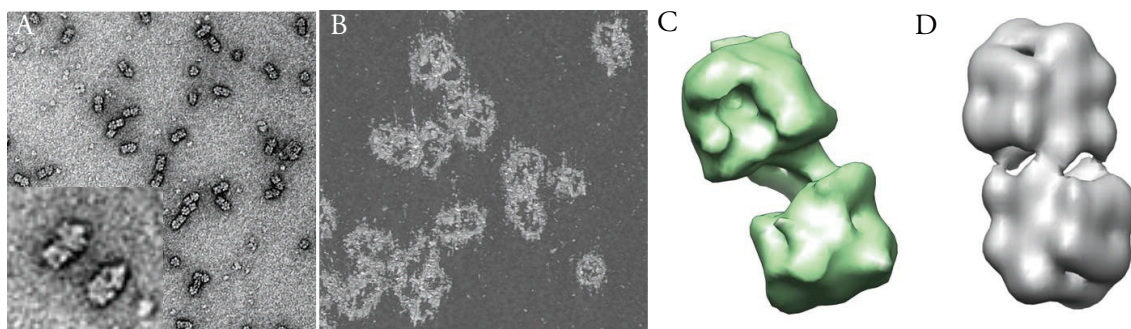


Fig. 3.1 Development of a 2x6mer hemocyanin reconstruction. (A) Images were taken at an Tecnai12 EM. For single particle analysis 3000-5000 particles and for tomography 5-9 particles were recorded on the Olympus CCD camera. (B) Tomographic tilt series were reconstructed using iMod and were then transferred into UCSF Chimera for subsequent processing. The quality of a single tomogram was very low. (C) After subtomogram clipping, alignment and averaging they produced a more detailed reconstruction. It was then used as a starting model for single particle analysis. It had enough features to ensure good alignment results. (D) The final reconstruction was calculated using C2-symmetry and a near mass threshold was calculated for display.

The negative stain image displayed (Fig. 3.1 (A)) is representative for the quality of all images for 2x6mer hemocyanins. The final tomographic reconstruction shows a rather low quality (Fig. 3.1 (B)). Nevertheless it was possible to extract single subtomograms and align them. After averaging the subtracted tomograms, the final tomographic reconstruction showed already good features (Fig. 3.1 (C)). Both hexamers show a square like and a roundish view and they are connected by a bridge. To improve this reconstruction it was refined against the single particles selected from the negative stain images. Finally C2 symmetry was applied to

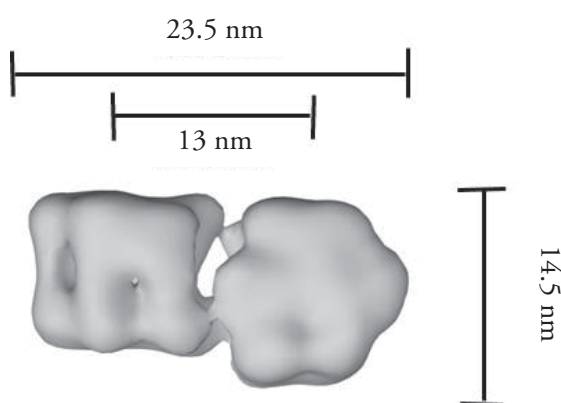


Fig. 3.2 Dimensions of the decapod-type 2x6mer hemocyanin. The 2x6mer hemocyanin is ~ 23.5 nm long and 14.5 nm wide/high. The distance between the two symmetry axes is ~ 13 nm.

the density map (Fig. 3.1 (D)). Afterwards both hexamers showed the same shape and threshold level. For interpretation and analysis of the obtained reconstructions, a crystallographic hexamer (pdbentry1H-CY) was docked automatically (fit in map; UCSF Chimera).

For all 2x6mer hemocyanins studied, a resolution of 25-30 Å was assessed. The dimensions of the three 2x6mers are ~ 24 nm by ~ 15 nm. The center of both hexamers is ~ 13 nm apart (Fig. 3.2). The shape of one hexamer can be described according to its orientations as hexagon (top view) or square (side view), if rotated by 90°.

Both hexamers are oriented almost orthogonally and they are connected by individual bridges. The interior of the hexamer is rather hollow, and after increasing the threshold value six distinct masses appear (Fig. 3.3). The view perpendicular to the symmetry axis (Fig. 3.3 (A)) reveals that there is only one connecting bridge left between the two hexamers.

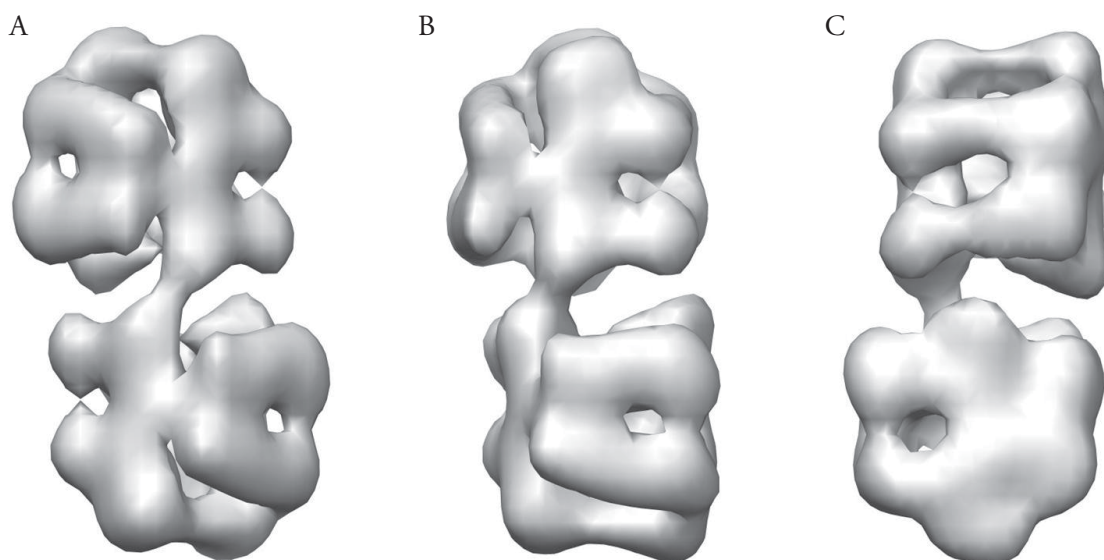


Fig. 3.3 *Astacus leptodactylus* 2x6mer hemocyanin shown at high threshold. (A) View perpendicular to the symmetry axis reveals individual pillars within the hexamer. (B) and (C) Perpendicular view towards the upper and lower hexamer reveals an almost orthogonal rotation between both, moreover revealing an empty inside.

3.1.1 *Astacus leptodactylus* 2x6mer hemocyanin (AleHc)

As described in the previous section, AleHc 2x6mer hemocyanin contains two hexamers that are almost in orthogonal orientation. Exact measurement yielded a rotation angle of 100° between both (Fig. 3.4). The orientations seen correspond to the orientations described in Fig. 3.3. For the 2x6mer AleHc one major bridge and two minor bridges were found. In the docked reconstruction (Fig. 3.4 (D)) one sees that the major bridge is between two 7-stranded β -barrel domains. For the two minor bridges no distinct structural feature can be described. There is a shift between the hexamer centres of $\sim 5\text{nm}$ (Fig. 3.4 (E) and (F)).

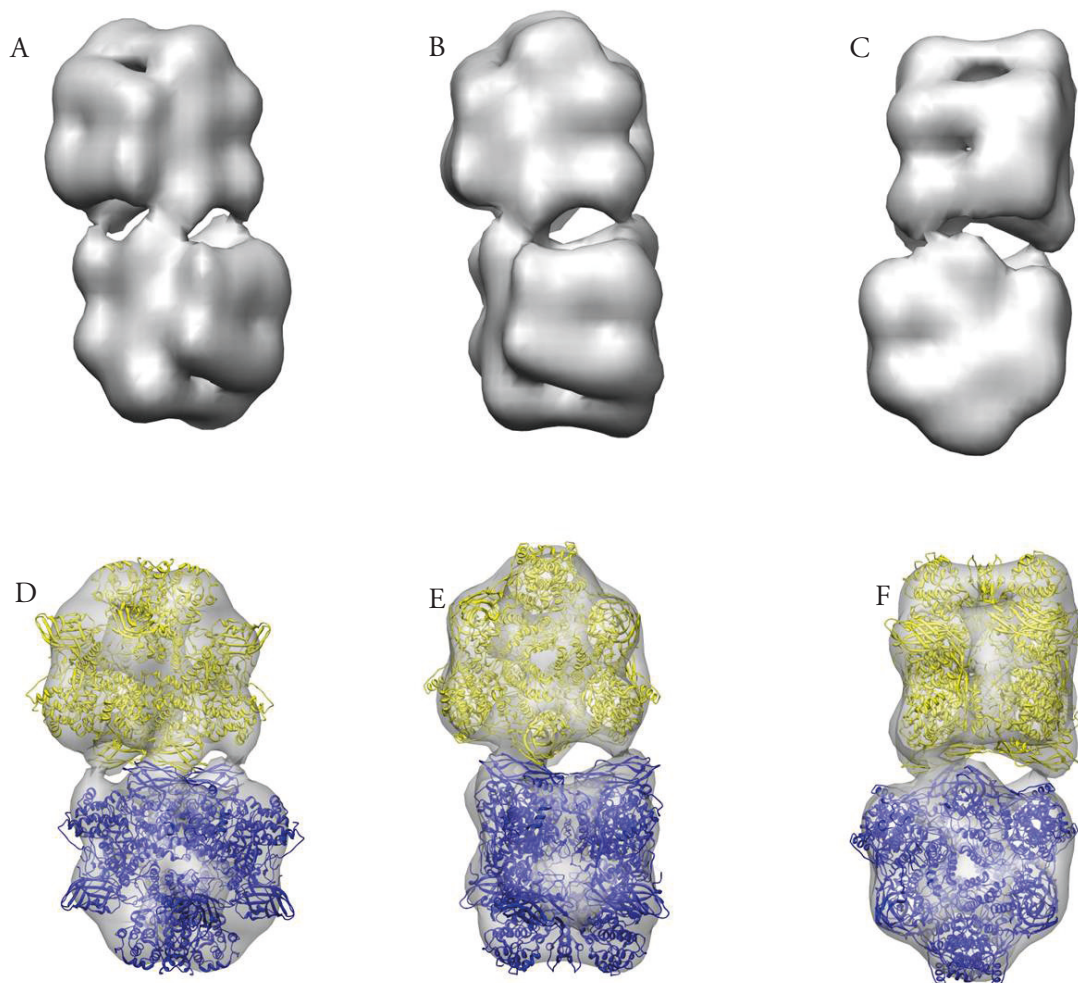


Fig. 3.4 *Astacus leptodactylus* 2x6mer hemocyanin. A)-C) Surface view of the reconstruction from the AleHc 2x6mer. A) Perpendicular view on the symmetry axis displays one main bridge and two smaller bridges. B) Perpendicular view on the upper hexamer. The lower hexamer appears to be rotated by 100° with respect to the upper hexamer. C) Perpendicular view on the lower hexamer. D)-F) Same as A)-D) with additional docking of two copies of an atomically resolved hexamer (pd-bentry1HCY).

3.1.2 *Carcinus maenas* 2x6mer hemocyanin (CmaHc)

The hexamers from *C. maenas* 2x6mer hemocyanin are rotated by 85° towards each other. There is a main bridge visible that is, as in AleHC, filled with 7-stranded β -barrel (Fig. 3.5 (D)). In the reconstruction two smaller bridges are visible, which are more prominent than in *A. leptodactylus*. Again the centres of the two hexamers are shifted by approximately $\sim 5\text{nm}$ (Fig. 5.3 (E) and (F)).

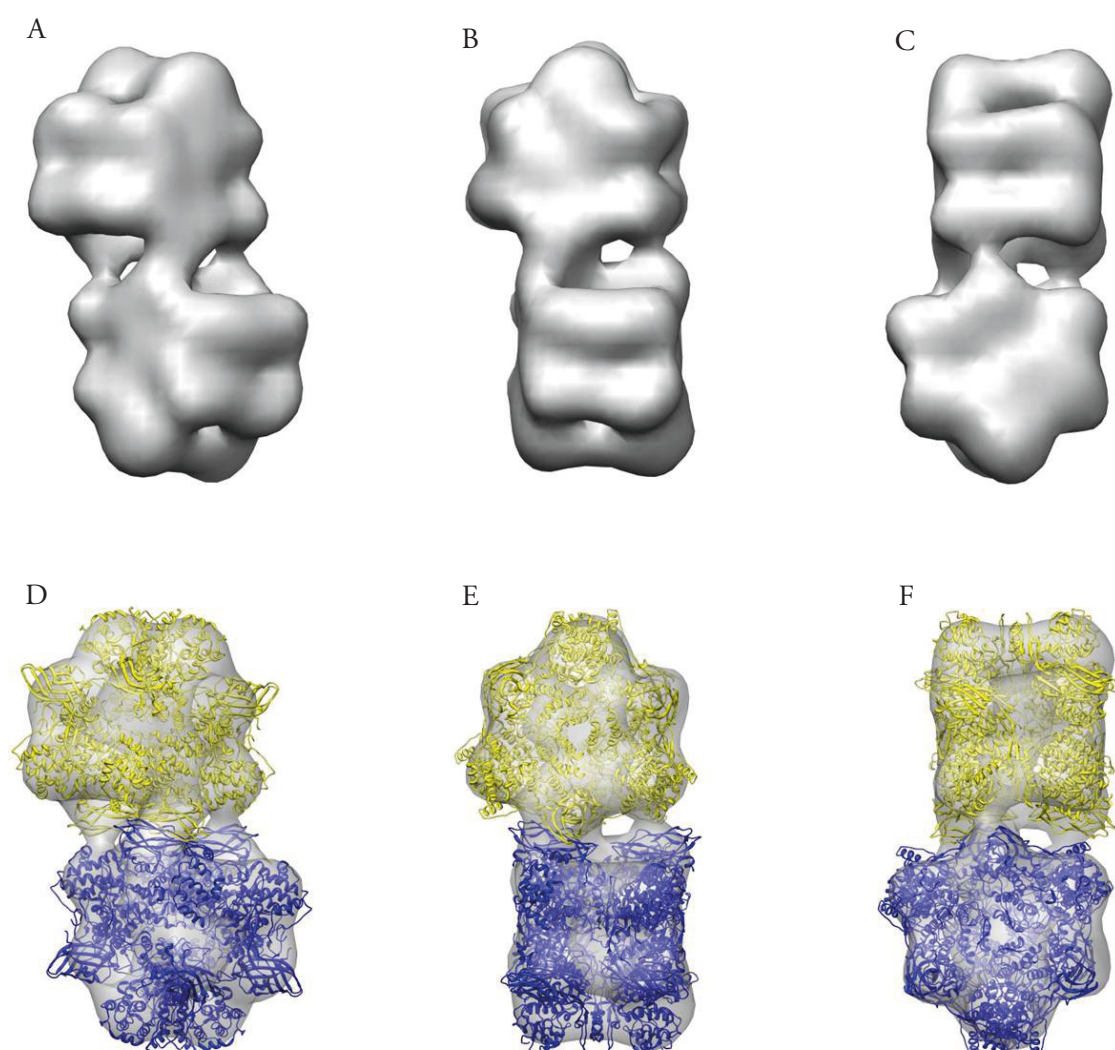


Fig. 3.5 *Carcinus maenas* 2x6mer hemocyanin. (A)-(C) 3D-reconstruction of the 2x6mer hemocyanin from *C. maenas*. (A) Perpendicular view on the symmetry axis displaying one main bridge and two smaller bridges. (B) Perpendicular view on the upper hexamer the lower hexamer appears to be rotated by 85° . (C) Perpendicular view on the lower hexamer. (D)-(F) Same as A)-(C) with additional docking of two atomically resolved hexamer structures (pdbentry1HCY). The major bridge is again partly filled with the 7-stranded β -barrel (D).

3.1.3 *Homarus americanus* 2x6mer hemocyanin (HamHc)

As for AleHc and CmaHc, C2 symmetry was used for reconstruction. In Fig. 3.6 the reconstructed models with and without docking of the molecular structures can be seen. There is again one major bridge visible in perpendicular view towards the symmetry axis (Fig. 3.6 (A)). Other than in AleHc and CemHc there is only one further bridge visible (Fig. 3.6 (B) and (C)).

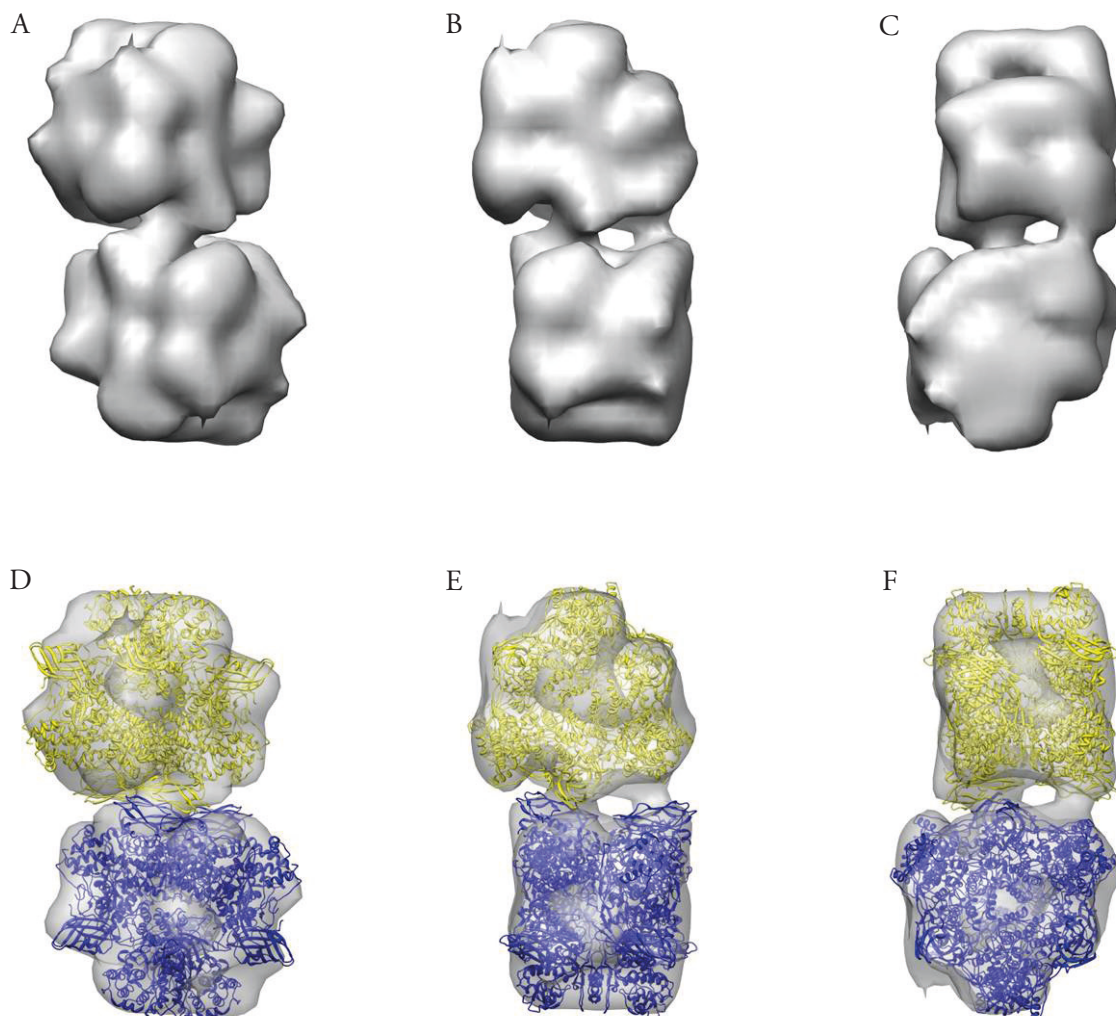


Fig. 3.6 *Homarus americanus* 2x6mers hemocyanin. (A)-(C) Surface view of the 3D-reconstruction of the 2x6mer hemocyanin of *H. americanus*. (A) Perpendicular view on the symmetry axis displays one main bridge and two smaller bridges. (B) Perpendicular view on the upper hexamer the lower hexamer appears to be rotated by 85°. (C) Perpendicular view on the lower hexamer. (D)-(F) Same as (A)-(C) with additional docking of two atomically resolved hexamer structures (pdbentry-1HCY). As for AleHc and CemHc the major bridge is filled with the 7-stranded β -barrel (D).

The main bridge is again filled with two 7-stranded β -barrel that are in very close proximity (Fig. 3.6 (D)) and the other bridge is not filled with mass after automated docking of the 1x6mer crystal structure (Fig. 3.6 (E) and (F)). The rotation between both hexamers is 83° and the two hexamer centres, as in AleHc and CemHc, appear not to be in line (Fig. 3.6 (B), (C), (E) and (F)). Nevertheless the shift is not as strong as in AleHc and CmenHc, were it is $\sim 5\text{nm}$, but it is only $\sim 2\text{nm}$.

3.1.4 *Odontodactylus scylarus* 2x6mer hemocyanin (OscHc)

As *O. scylarus* does not belong to the decapods, but to the stomatopods, and whether the 2x6mer hemocyanin has a different architecture (Bijlhold and vanBruggen, 1986; Scherbaum

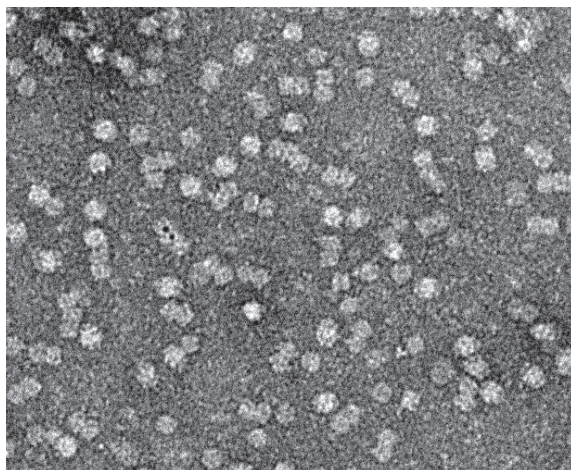


Fig. 3.7 Negative stain image of *O. scylarus*. The negative stain image already reveals a different architecture compared to decapods. Two main views are visible. One step like view and one described as elongated hexamer.

et al., 2010; Micetic et al., 2010). It was therefore interesting if differences appear in negative stain. In EM images two major views can be seen that can be described as “step like” and as “elongated” (Fig. 3.7).

As there was no good starting model available, a tomographic model was generated (Fig. 3.8 (A)). After asymmetric single particle reconstruction, it became clear that C2 symmetry could be applied (Fig. 3.8 (B)). The dimensions of the protein complex were assessed to be $\sim 20\text{nm}$ by $\sim 16\text{nm}$ and that the symmetry axes are $\sim 4.5\text{nm}$ apart. Furthermore a rotation of 16° around the upper symmetry axis is necessary to bring the two hexamers into the same rotational orientation (Fig. 3.8 (C)). The interior of the hexamers is empty

as described for AleHc, CmaHc and HamHc.

Looking at the reconstructed models from different views reveals two major bridges between the two hexamers that are perpendicular to the symmetry axis (Fig. 3.9 (A) and (B)). Looking at these bridges after docking of the molecular structures (pdbentry1HCY) reveals that they are filled with mass, bringing the two hexamers in close proximity (Fig. 3.9 (E) and (F)). Looking at the density map from the top one can see the rotation between the two hexamers described above (Fig. 3.8 (C)). Moreover it is easy to assess from where the elongated views in the EM originated. For the 2x6mers from decapods there were six pillars described (Fig. 3.3) that can be seen at lower threshold levels. For the OscHc 2x6mer it seems as if there

were more distinct masses, that correspond to one monomer after docking of the 1x6mer crystal structure (Fig. 3.9 (A)-(C)). Especially in Fig. 3.9 (B) and (C) the separated masses within the hexamers can be seen. After docking these parts are filled with one monomer from the hexamer.

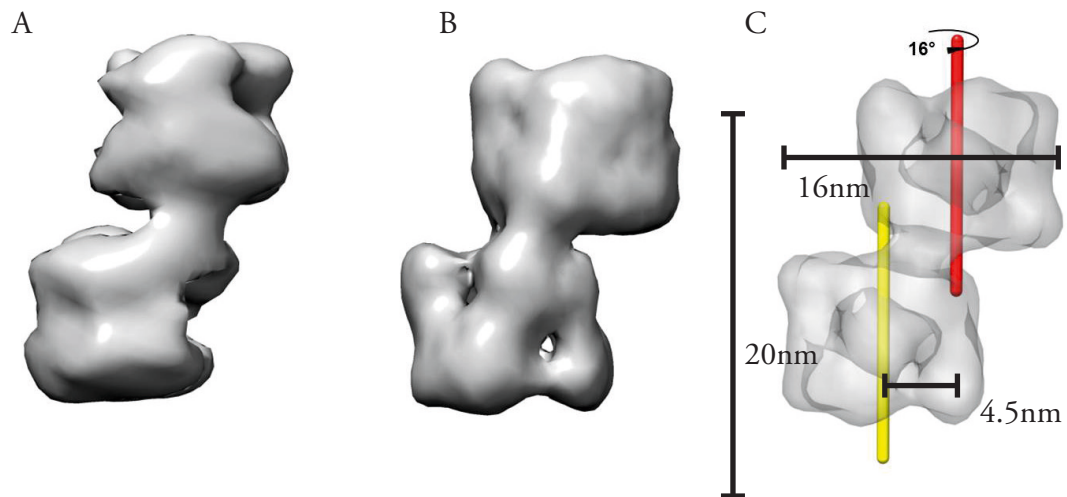


Fig. 3.8 Development of the 3D density map from the 2x6mer OscHc. (A) Tomographic reconstruction after sub tomogram averaging. (B) Asymmetric reconstruction after refinement of A against the selected single particles. (C) Dimensions of the final reconstruction are ~20nm by ~16nm. The rotation of the upper hexamer by ~16° around the symmetry axis brings both hexamers in into the same rotational orientation.

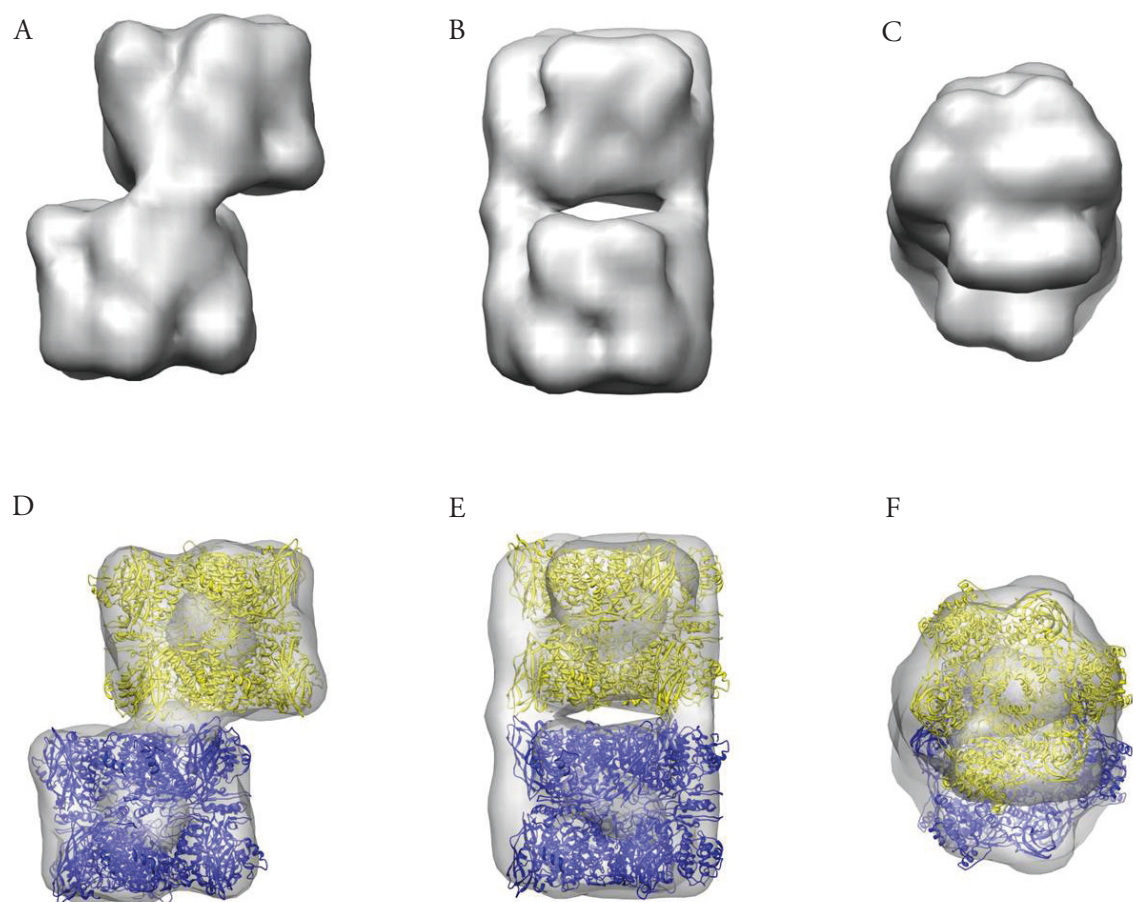


Fig. 3.9 *Odontodactylus scylarus* 2x6mer hemocyanin. (A)-(C) Surface view of the 3D-reconstruction of the 2x6mer hemocyanin of *O. scylarus*. (A) Perpendicular view on the symmetry axis displays one major connection. (B) Orthogonal view on the symmetry axis reveals two major connections between the hexamers. (C) Top view on the molecule reveals a 16° rotation of the hexamers against each other. (D)-(F) Same as (A)-(C) with additional docking of two atomically resolved hexamer structures (pdbentry1HCY).

3.2 The gp140 proteins from HIV X4- and R5-strands

3.2.1 3D reconstruction of NL4-3 (X4) and Ada (R5)

The 3D reconstructions from NL4-3 and Ada were all performed using negatively stained images with protein samples obtained from

. At a size of ~ 420 kDa negative stain is faster and easier than vitrification and as it was unclear, whether there are substantial differences, the first goal was to receive a model at 25\AA resolution for both strands.

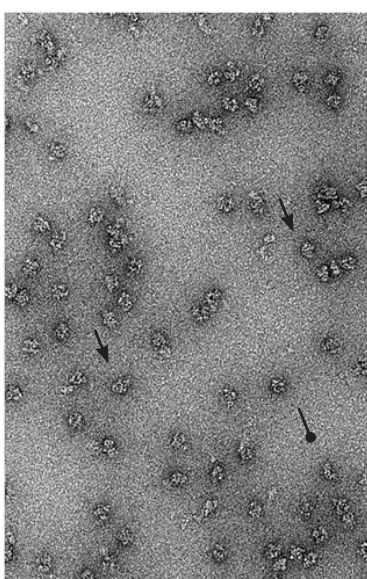


Fig. 3.10 Negative stain of NL4-3. Particles of the expected size are marked with an arrow and to small particles with a round arrow.

The image from negatively stained NL4-3 (Fig. 3.10) showed particles that had the expected size and smaller ones. According to previous work (Chen, et al., 2005; Pancera et al., 2010; Zhu, P. et al, 2008) gp140 was believed to form trimeric protein complexes. The smaller particles seemed to be monomers from dissociated proteins. After selection of single particles, class sum images were generated using MSA. These were then used to create a first starting model with the module *euler* (IMAGIC-5) that uses the common line technique. As seen in reference free class sum images the gp140 proteins display C₃ symmetry and it was therefore applied on the starting model (Fig. 3.11). This starting model shows an empty inside and three stalks connect the bottom with the top. From the side it has a triangular shape and on the top three small bumps are visible. The stalks are not orthogonal to the top or the bottom, but the model seems to be twisted. This model was then used to refine both data sets against it, which should prevent starting model bias. The surface representations of the

two final models (NL4-3 and Ada) that were stable after ~ 30 iterations of refinement then reveal significant differences between both molecular complexes (Fig. 3.12). For NL4-3 about 8000 particles were manually selected and a resolution of 25\AA was ultimately achieved. For Ada, 16000 particles were selected to reach the same resolution.

NL4-3 in side view (Fig. 3.12 A) can be described as rather open in the upper region of the molecule, smaller connections in the middle forming a more compact particle and a rather long stalk at the bottom. On the top the mass ends with a thin protrusion. From the top (Fig. 3.12 (B)) the trimeric shape of the molecule becomes obvious and there are no connections visible between the three upper parts of the reconstruction. Moreover a central mass can be ob-

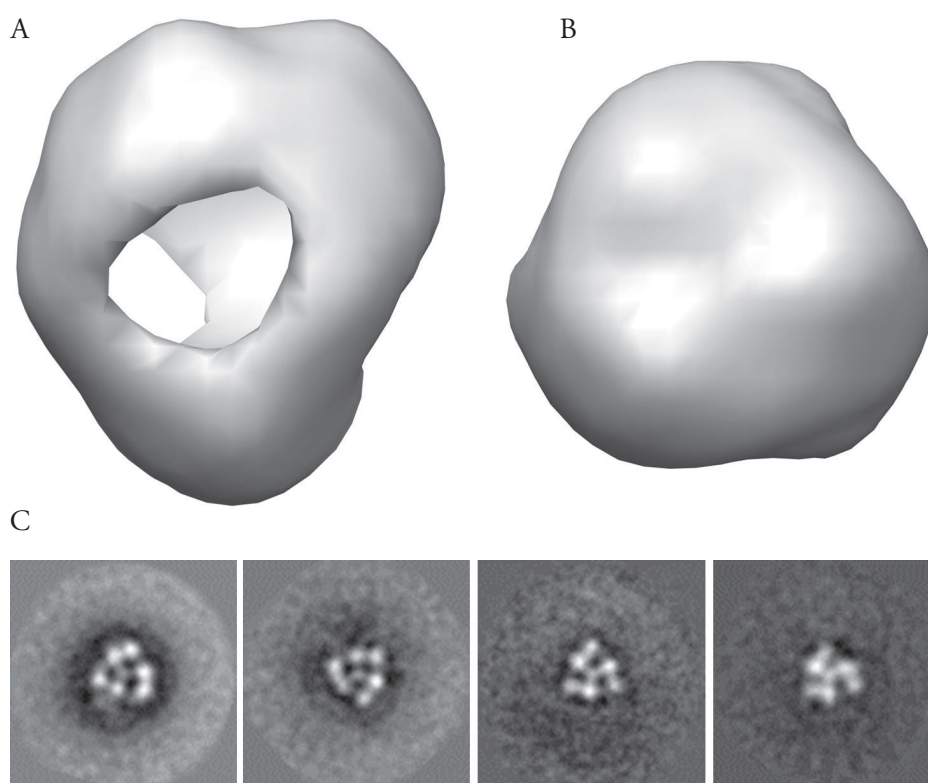


Fig. 3.11 Initial gp140 model. (A) Side view and (B) top view of the starting model used for gp140 reconstruction. (C) Reference free class sum images from NL4-3.

served that connects all three spikes in the middle of the protein. The side view representation from the Ada reconstruction (Fig. 3.12 C) is shorter than the one from NL4-3. The upper part seems to be more dense and there are three protrusions from a plateau-like surface. At the bottom the structure does not protrude, but forms a compact mass that is connected by bridges to the remaining structure. From the top (Fig. 3.12 D) there is again the symmetrical shape and the central mass. Unlike in NL4-3 the upper part masses are not separated, but connected. If one compares both reconstructions (docked with *fit in map*, UCSF Chimera) (Fig. 3.12 (E) and (F)), more differences emerge. As described NL4-3 appears to be stretched and less compact. From the top both reconstructions seem to be rotated towards each other by $\sim 40^\circ$. Nevertheless the lower masses are in good agreement. Moreover the steep protrusions seen in Ada appear to be tilted towards the symmetry axis.

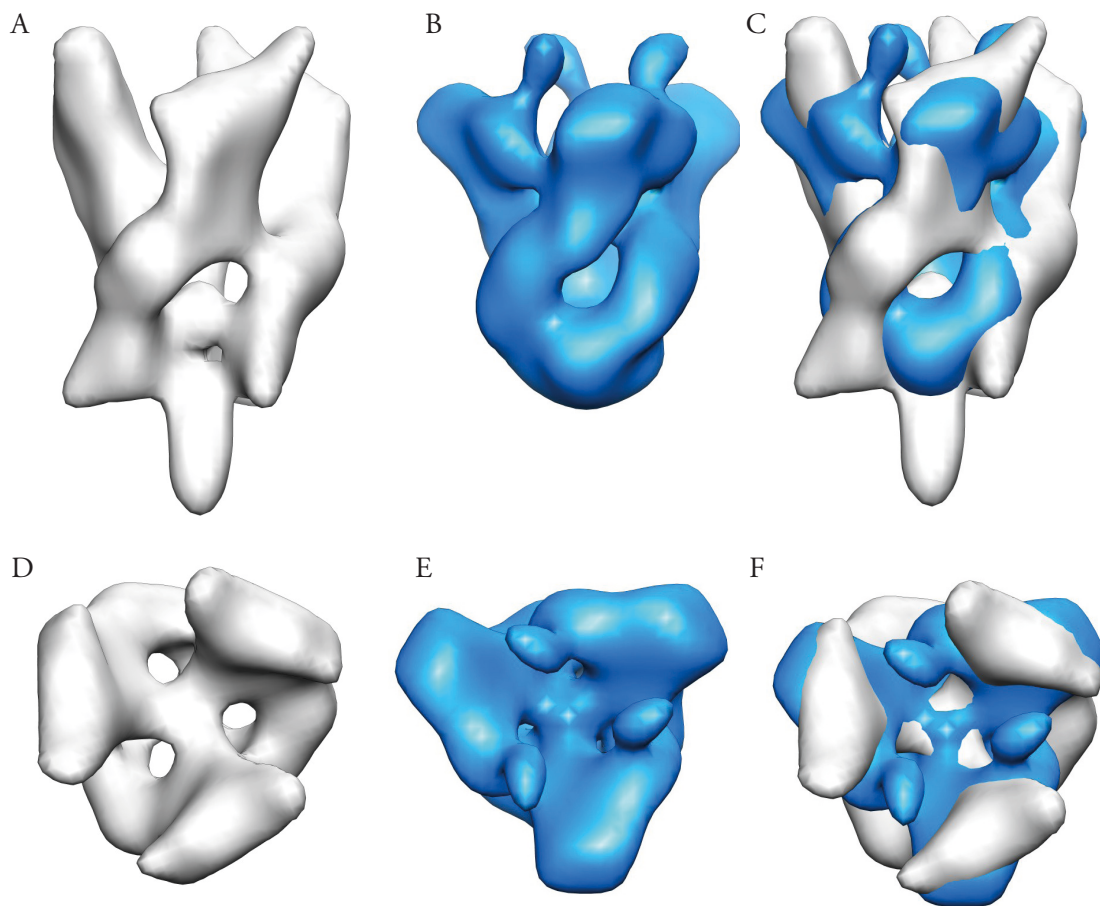


Fig. 3.12 3D reconstruction of NL4-3 and ADA gp140 trimers. (A) NL4-3 gp140 trimer (grey) viewed perpendicular to its threefold symmetry axis (side view); note that the three masses are mainly connected in the lower part. (D) NL4-3 gp140 trimer viewed along the threefold axis (top view), showing the three major protrusions pointing outwards. (B) Side view of the Ada gp140 trimer (blue), exhibiting connecting masses in the upper and lower part, respectively. (E) Top view of the ADA gp140 trimer, showing the three steep protrusions pointing slightly inwards. Superposition of both structures in (C) side view and (F) top view, as obtained by automated fitting. Note fitting of the oblique masses in the lower parts, and counterclockwise rotation of the R5 by $\sim 40^\circ$ with respect to the X4 structure in the upper part. In the side views, the target cell would be on the top and the viral membrane at the bottom.

3.2.2 Molecular model building and immunoelectron microscopy

To interpret the 3D-reconstructions it was necessary to develop a molecular model with the available crystal structures. To generate an almost complete gp120 structure (V4/V5 and C- and N-terminal ends missing) three different crystal structures were combined. On the core part, pdbentry 2NY7 (Zhou et al., 2007) was used and the missing V3-loop (pdbentry 2B4C) (Huang et al., 2005) was fused to the overlapping ends of the structure. As for

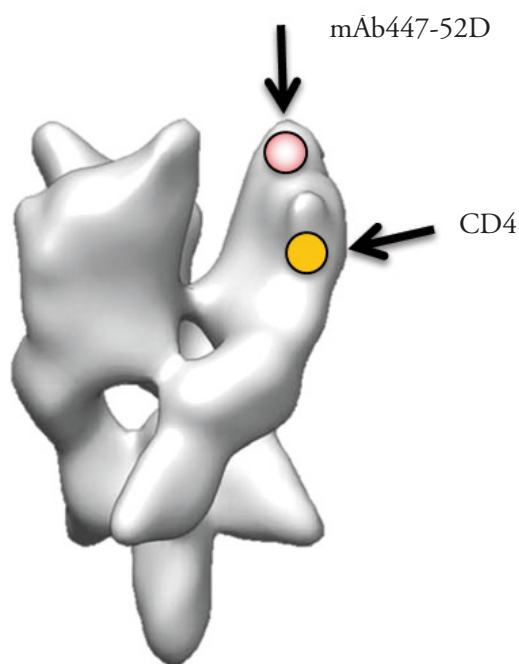


Fig. 3.13 mAbs binding epitops. Binding sites of mAbs used in the experiments indicated with red circles and CD4 binding site with yellow circle.

the V1/V2-loop (pdbentry 3U4E) (McLellan et al., 2011) the overlapping parts were only a few amino acids long and had no secondary structure elements, it was not used here. Moreover, the crystal structure was produced from a mini-prodomain, making arrangement and docking very difficult. As the gp41 part is not resolved at higher resolution, the fusion peptide and the N- and C-terminal heptat repeats (NHR and CHR) were not docked as individual structures. Although the fusion peptide was resolved to atomic resolution (pdbentry 2ARI; Jaronec et al., 2005) as were the NHR and CHR (pdbentry 2X7R; Buzon et al., 2010) the exact localization in the density map is unclear. As the fusion peptide must be covalently connected to gp120 it was placed as rod (orange) into the structure as were the NHR and the CHR (green rod). Both rods are at the expected size of the missing structures.

To assign gp120 mAb447-52D was used as it targets the V3-loop. This was done to find the correct orientation of gp120 in the reconstruction and to show the localization of V3.

3.2.3 Docking of the molecular model into NL4-3 and Ada

As the orientation and localization of the single parts of the molecular model are now clear, they were together docked into the unliganded structure of NL4-3 (Fig. 3.15 (A) and (C)). From the side (Fig. 3.15 (A)) it appears as if nearly all masses are filled with the molecular model, except for the parts marked (asterisk). The center is formed by the gp120 (blue; later bridging sheet light blue). The upper protrusions are filled with the V3 loop (red) and the V1/V2 loop (purple sphere). The gp41 part is formed by the fusion peptide (orange rod). As the structure of gp41 is not clearly resolved the NHR and the CHR are accounted for by a single rod.

For Ada the gp120 part of the NL4-3 molecular model was fitted automatically (*fit in map*, UCSF Chimera). The gp41 part was then manually docked into the empty space available. As for NL4-3 the V3 loop occupies the steep protrusions reaching to the top of the

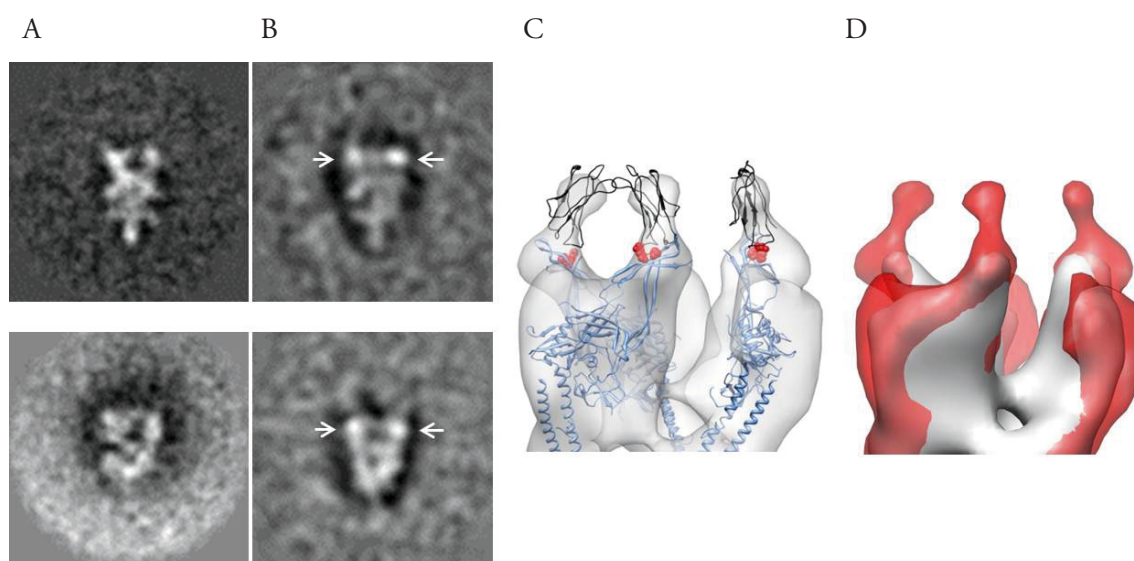


Fig. 3.14 Docking of mAb 447-52D. (A) Two different side views from the class sum images of unliganded NL4-3. (B) Same view as in (A) but sample was incubated with mAb447 and extra mass appears in the upper region of the molecular complex (arrows) (C) 3D reconstruction of the incubated sample with fitting of the molecular model (blue) and the binding epitope (red). Epitope binding domain was docked into the extra mass (black). (D) Superposition of unliganded (grey) and mAb447 incubated reconstruction (red).

molecule. From the top (Fig. 3.15 (D)) the three molecular models appear in closer proximity as in NL3-4, which is not very surprising as the reconstruction seems to be more compact.

3.2.4 Activation of NL4-3 with CD4

As CD4 is the primary receptor for native HIV Env proteins and interaction leads to large changes in the quaternary structure. NL4-3 was activated with a soluble four domain CD4. From negative stain images ~ 59000 single particles were selected and despite all efforts only an inferior resolution of $\sim 30\text{\AA}$ was reached. We also found that in our C3 symmetry reconstructions no extra mass, accounting for CD4, appeared in the density map. For gp140 from the simian immunodeficiency virus (SIV) it was suggested that only one CD4 molecule binds to the trimer (Zhang et al., 2001; Kim et al., 2001). Therefore no symmetry was applied during the further reconstruction process and in fact only one extra mass appeared in the trimer (Fig. 3.16).

The reconstruction shows a cage like structure with one mass centre connecting the three main masses at the bottom. From the top (Fig. 3.16 (B)) it appears that there exist connections at the top and that the central mass is missing here. For interpretation the molecular model of unliganded NL4-3 was docked into the free masses of the density map. To account for the molecular changes the gp120 core structure (pdbentry 2NY7) was changed to a CD4

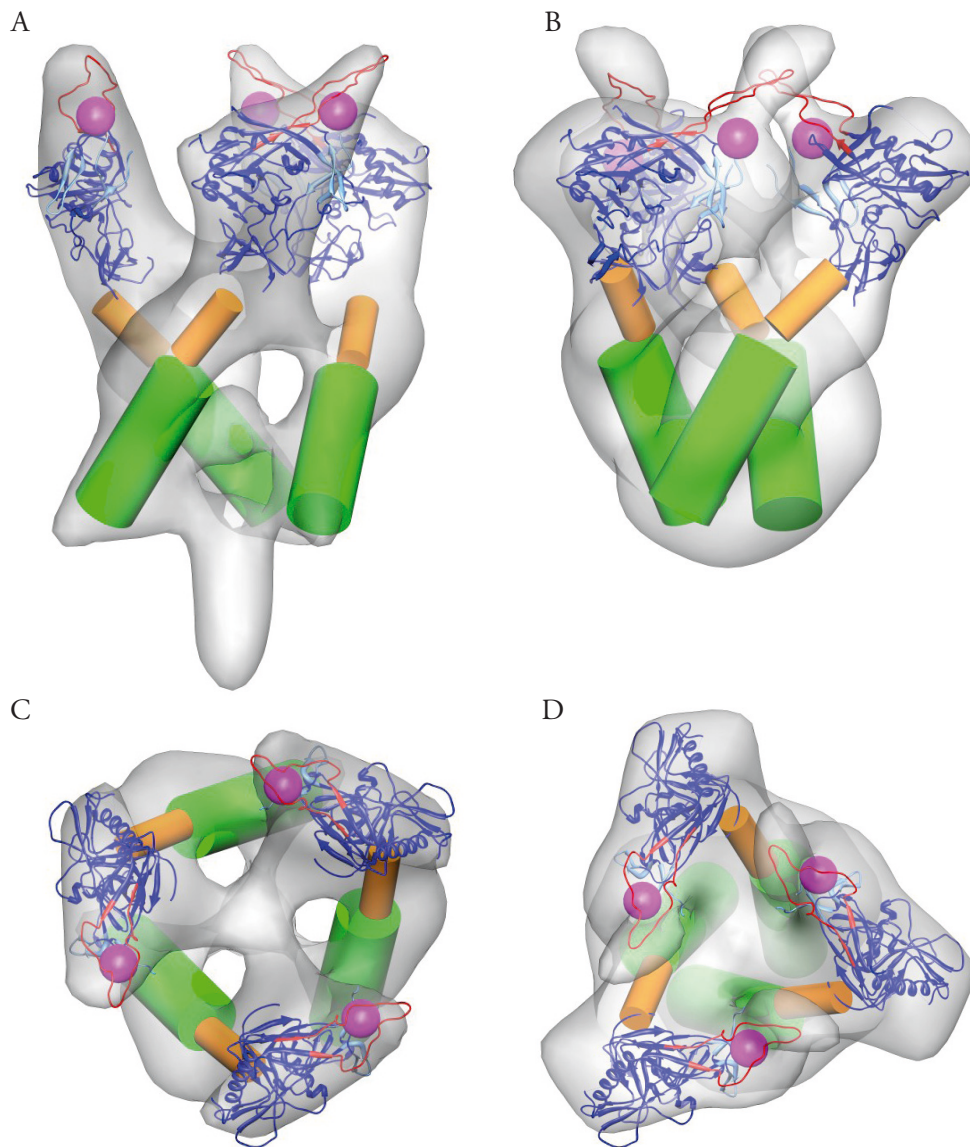


Fig. 3.15 Molecular models of NL4-3 gp140 and ADA gp140 trimers. (A) Side view and (C) top view of the final molecular model of the unliganded NL4-3 gp140 monomer obtained by docking of the substructures to the 3D reconstruction, taking into account the results from immunoelectron microscopy and CD4 labeling. In the color-coded molecular model, the V3 loop (2B4C, red) and the V1V2 loop (magenta) extend into the protrusions of the 3D reconstruction. The gp120 core (2NY7; blue) fills most of the upper part (bridging sheet in light blue). The fusion peptide (orange) covalently links the C-terminus of gp120 and the N-terminal heptad repeat (NHR) of gp41. As the NHR and CHR could not be assigned they were docked as one stalk (green). (B) and (D) as (A) and (C) but with the density map from Ada.

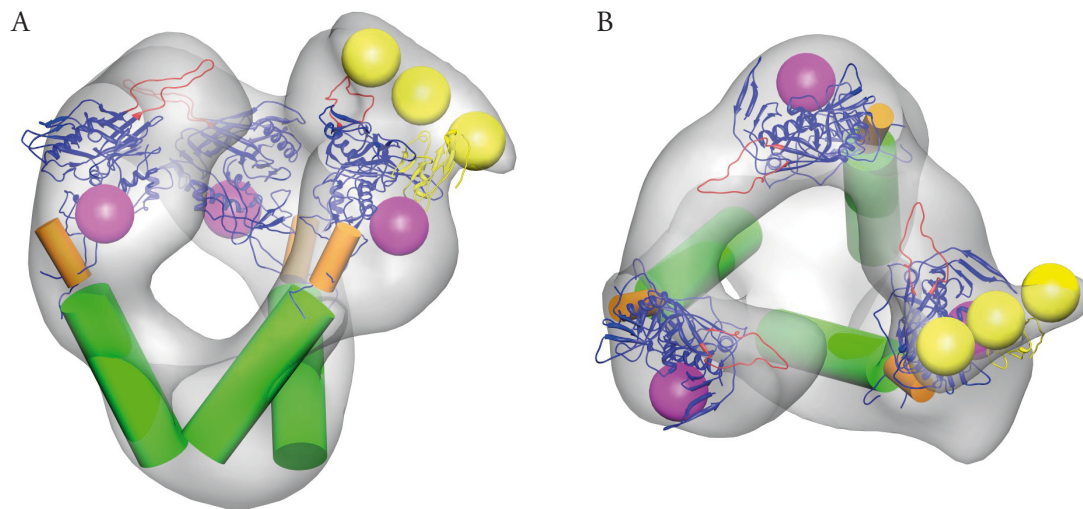


Fig. 3.16 3D reconstruction of CD4-liganded NL4-3 gp140 trimers. (A) Side view and (B) top view of the CD4 liganded state of the NL4-3 gp140 trimer, including the molecular model of the liganded NL4-3 gp140 (same colour code as in Fig. 3.15). Bound four domain CD4 is indicated in yellow ribbon (domain 1) and yellow spheres (domains 2-4).

bound form (pdbentry 3JWD; Pancera et al., 2010). Moreover the V1/V2 loop (magenta sphere) was moved to further connect to its C- and N-terminal partners (Fig. 3.16). From the CD4-bound crystal structure only one CD4 domain was left and the others were replaced with yellow spheres. After docking of the gp120 part of the structure it was obvious that there was only one major mass unoccupied that could be filled with CD4. To receive a fully filled density map the gp41 parts were again docked as rods (see 3.2.3).

3.3 The 20S-PA28 proteasome complex

3.3.1 Raw data acquisition and class sum formation

As described in the introduction (1.4), the 20S proteasome can be activated by PA28. This protein complex consists of seven monomers forming a ring-like structure that can dock on both ends of the 20S particle (Cascijo et al., 2002; Whitby et al., 2000).

In negative staining images (Fig. 3.17) clear identification of particles with a single PA28 was only possible in side view, in which PA28 appeared as extra mass on one side of the 20S molecule. There were no particles detected that showed activator complexes at both sides. As there were only one or two capped side view particles per EM image, 1200 images were recorded. After automated particle selection and CTF-correction, a data set with ~170.000 particles was available. This data set was then subjected to MSA to sort the particles. Although this produced a well presorted data set it was manually cleaned from all uncapped side views. At the end of this procedure, a set of ~2000 side view 20S-PA28 particles (Fig. 3.18 (A)) was generated. Although a multitude of 20S uncapped side views was available, there were only 2000 particles selected for better comparability (Fig. 3.18 (B)).

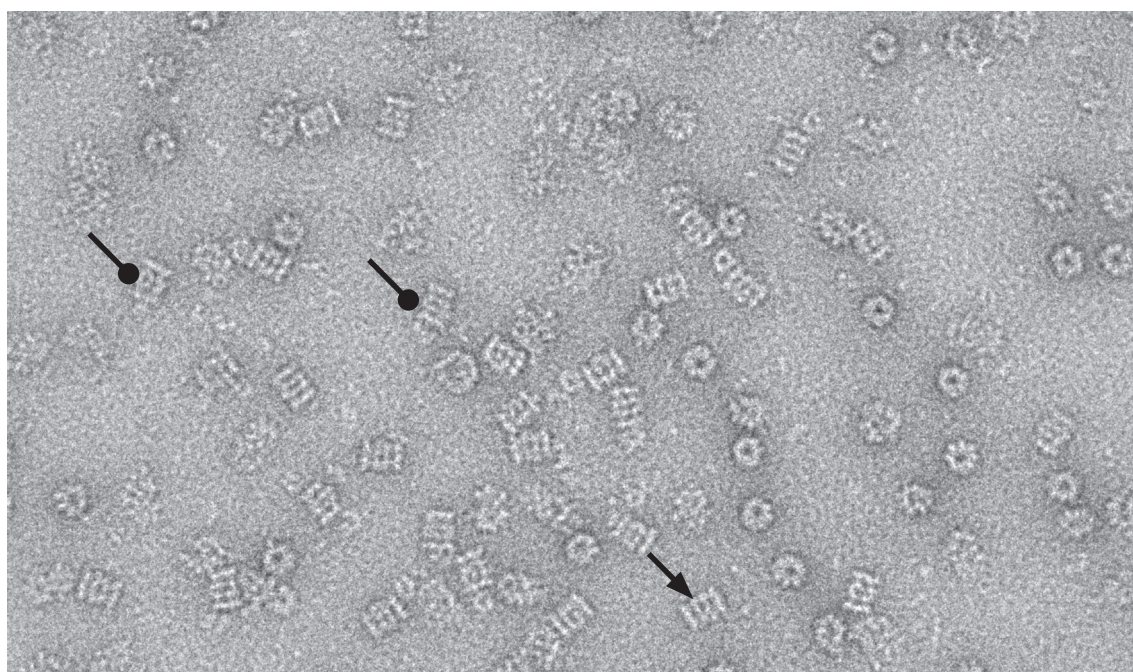


Fig. 3.17 Negative stain image of 20S-PA28 and 20S. Negative stain image of the sample with uranyl formate. Note the large surplus of uncapped particles (arrow) in comparison to the single capped 20S-PA28 complexes (round arrow)

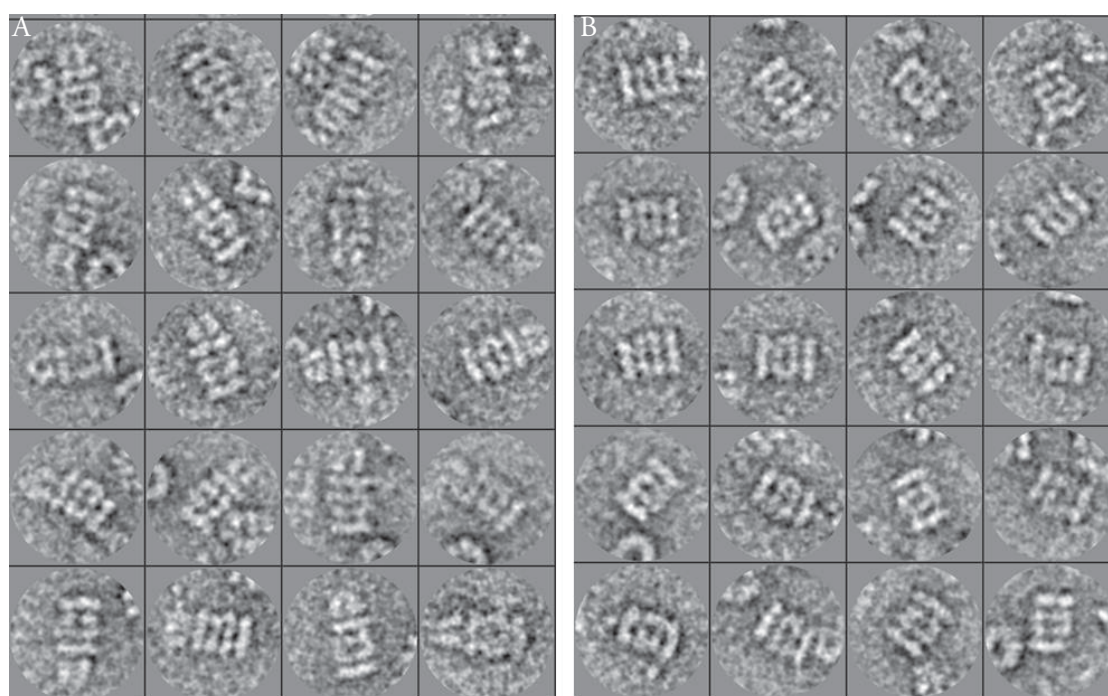


Fig. 3.18 Single 20S-PA28 and 20S particles in negative stain. (A) 20S-PA28 complex and (B) uncapped 20S proteasome.

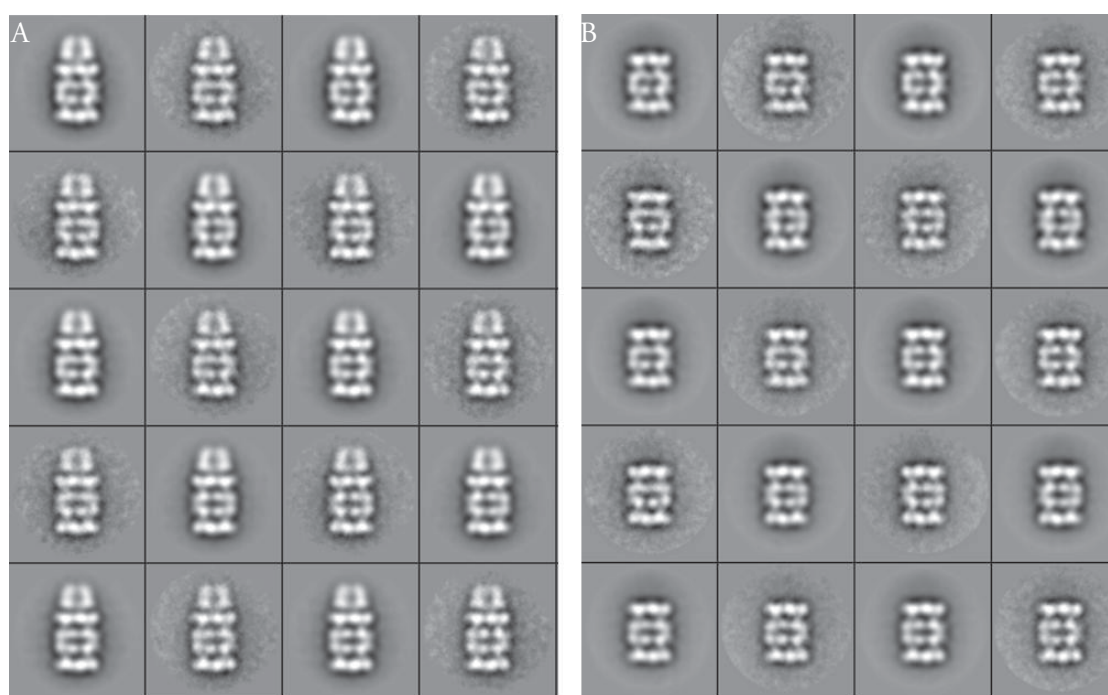


Fig. 3.19 Class sum images from 20S-PA28 and 20S particles. (A) Class sum images of the 20S-PA28 complex and (B) class sum images of the uncapped 20S proteasome. Note that the 20S part of the 20S-PA28 complex is in good accordance with the solitary 20S particle. Moreover there is a channel through the PA28 activator visible.

After generating an initial model it was refined until it was stable. This was done in EMAN and about 50 iterations were calculated. At the end a resolution of $\sim 18\text{\AA}$ was reached. An angular increment of the references of 5° was used and the reconstructed models were normalised (*norm-filt*, EMAN). Comparing the class sum images from the 20S-PA28 and the 20S proteasome with the corresponding forward projections reveals their good accordance (Fig. 3.19). For the 20S-PA28 complex the 20S part and the PA28 part are equally well resolved. For the 20S part of the complex four “stripes” can be seen and the PA28 part displays a channel. For the 20S proteasome the class sum images display the same features as for the 20S part of the 20S-PA28 complex.

3.3.2 Density map and molecular model of the 20S-PA28 complex

As seen in the class sum images the reconstruction of 20S-PA28 displays some interesting features. Looking at it in side view with different threshold values reveals that the first parts of the reconstruction disappearing are the connections between the 20S core and the PA28 activator (Fig. 3.20). Displaying a near mass threshold (Fig. 3.20 (B)) shows that these connections are missing. Looking from the top at the near mass threshold reveals a channel through the PA28 activator complex, and an opening of the 20S particle can be seen (Fig. 3.20 (C)). Looking at the molecule from the bottom shows no opening, but a closed structure (Fig. 3.20 (D)). It was described that PA26 opens the central pore of the 20S proteasome by shifting the N-terminal ends to the side (Whitby et al., 2000). In the bovine 20S particle these ends reach into the center and close the central pore (Unno et al., 2002). Therefore a combined model was produced here consisting of half a bovine 20S (Fig. 3.21 (green)) with a closed central pore and half a yeast 20S (Fig. 3.21 (blue)) with the *Trypanosoma* PA26 activator on top (Fig. 3.21 (red)).

The combined molecular model produced fitted the density map well in size and shape. In side view at lower threshold value the faint connection between the 20S core and the PA28 activator is filled with the N-terminal ends moved away from the central pore (Fig. 3.21 (A)). At near mass threshold the connections between the activator and 20S proteasome are not accounted for by mass (Fig. 3.21 (B)). Nevertheless all main masses are in good correlation with the 3D reconstruction. From the top the opening of the molecular complex can be seen in good agreement with the docked molecular model. From the bottom the docked molecular model and the density map are in good agreement, too (Fig. 3.21 (C) and (D)).

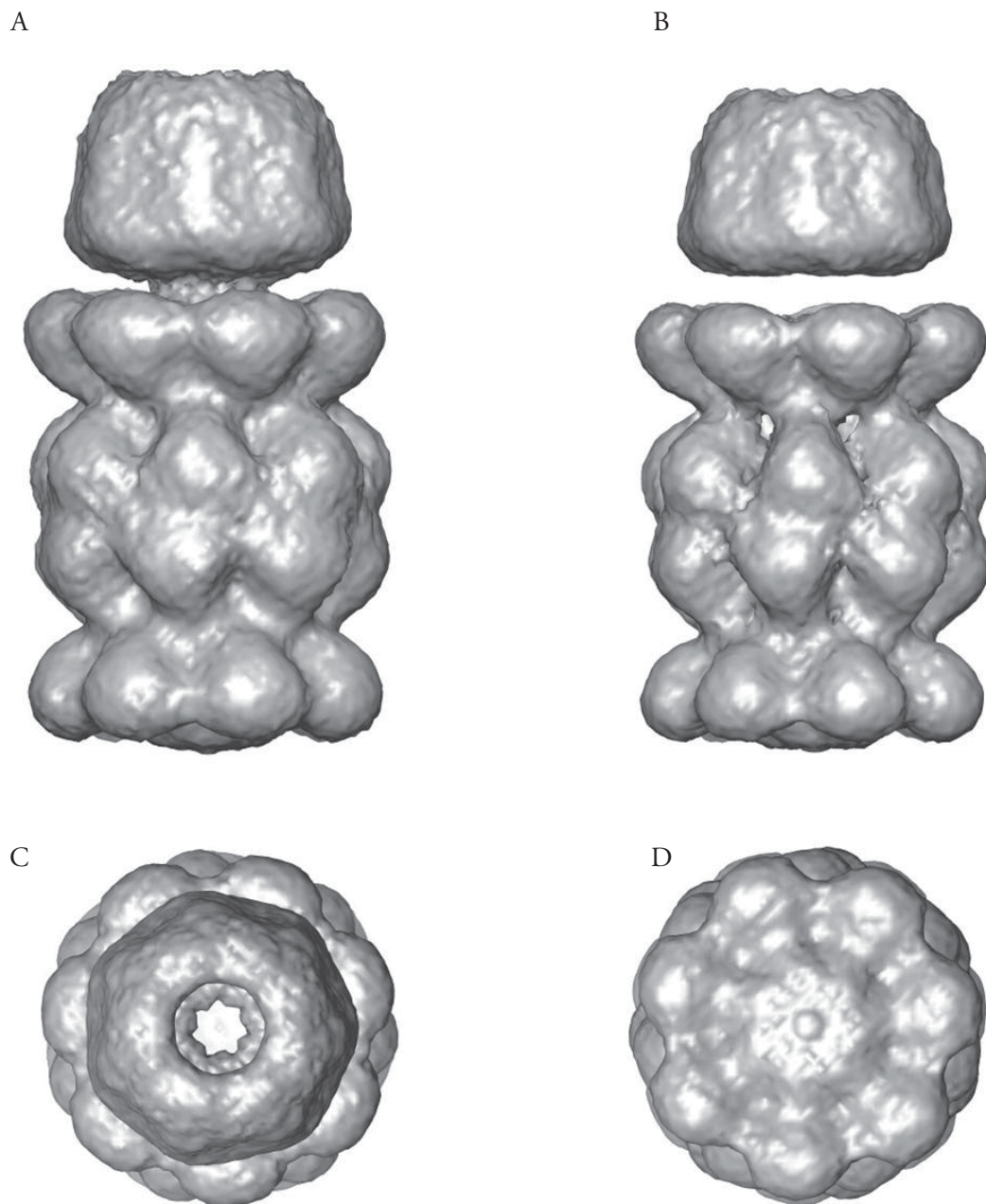


Fig. 3.20 3D reconstruction of the 20S-PA28 complex. (A) Side view at lower threshold at which faint connections between 20S and PA28 emerge. (B) Side view at approximately mass-corrected threshold; note disappearance of the thin connections between 20S and PA28. (C) Top view at approximately mass-corrected threshold; note tentative open state. (D) Bottom view at approximately mass-corrected threshold; note tentative closed state. The resolution reached is $\sim 18\text{\AA}$.

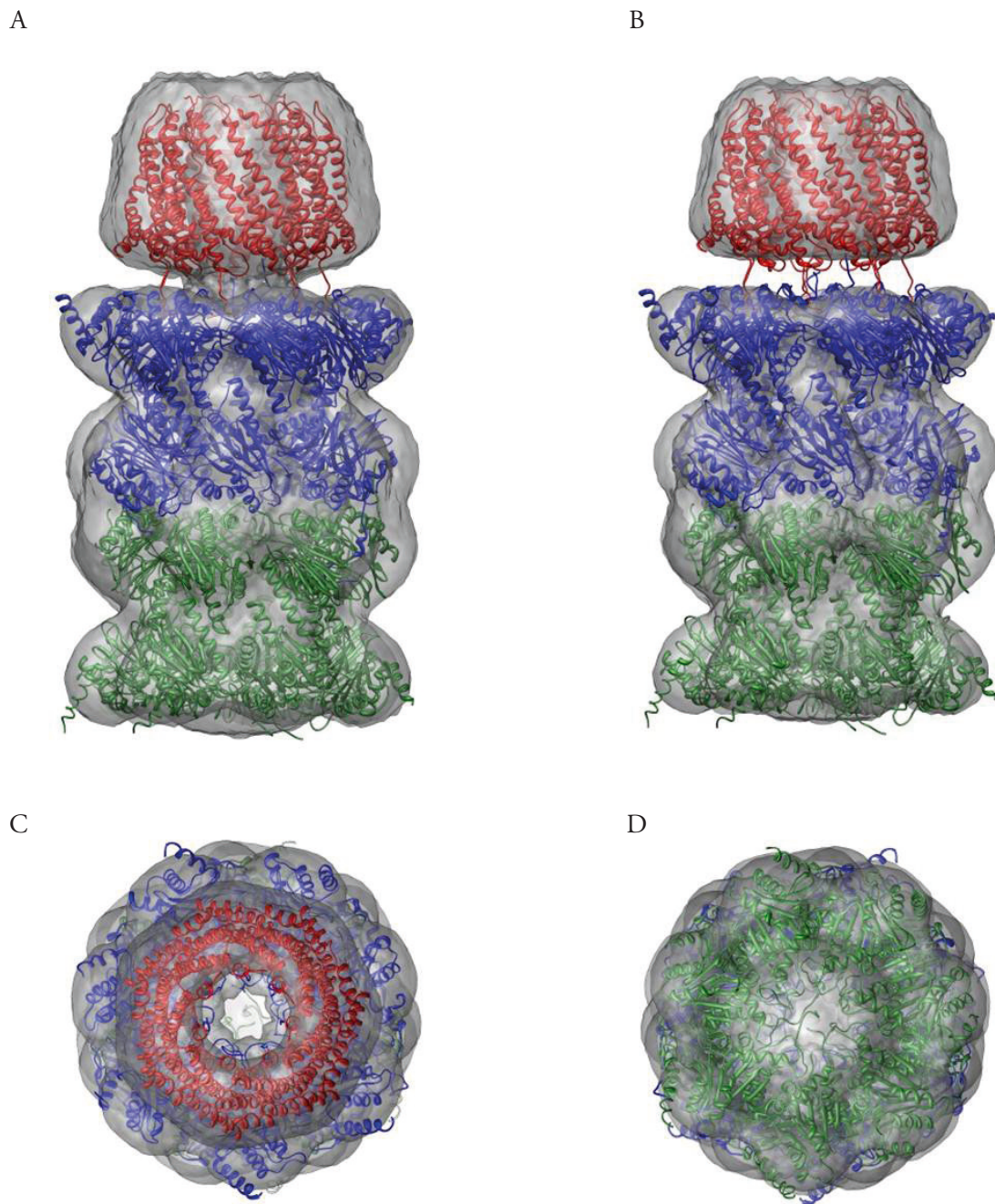


Fig. 3.21 3D reconstruction of 20S-PA28 with docked crystal structures. For the closed state we used the crystal structure of the bovine 20S proteasome (pdbentry 1IRU; green). For the open state we used the crystal structure of a PA26 activated 20S proteasome (pdbentry 1FNT; blue and red). (A), (B) Side views as in Fig. 3.24. (C) Top view as in Fig. 3.24; note fitting of the open state crystal structure. (D) Bottom view as in Fig. 3.24. Note that in the crystal structures, the center in (D) is occupied by the N-terminal ends of the subunits that in (C) are shifted away from the center by the activator. The 3D reconstruction conforms to that situation.

3.3.3 3D density map and docked molecular model of the 20S particle

As for the 20S-PA28 complex a model was reconstructed from the same data set for quality control and reliability of the produced data. From the selected and CTF corrected side view images a reconstruction at the same resolution level was produced (Fig. 3.22). Looking at the reconstructed model from the side reveals the barrel like shape seen in the class sum images with four distinct layers of mass (Fig. 3.22 (A)). From the top and the bottom the reconstructed model shows no opening (Fig. 3.22 (B) and (C)) as seen in the 20S-PA28 complex.

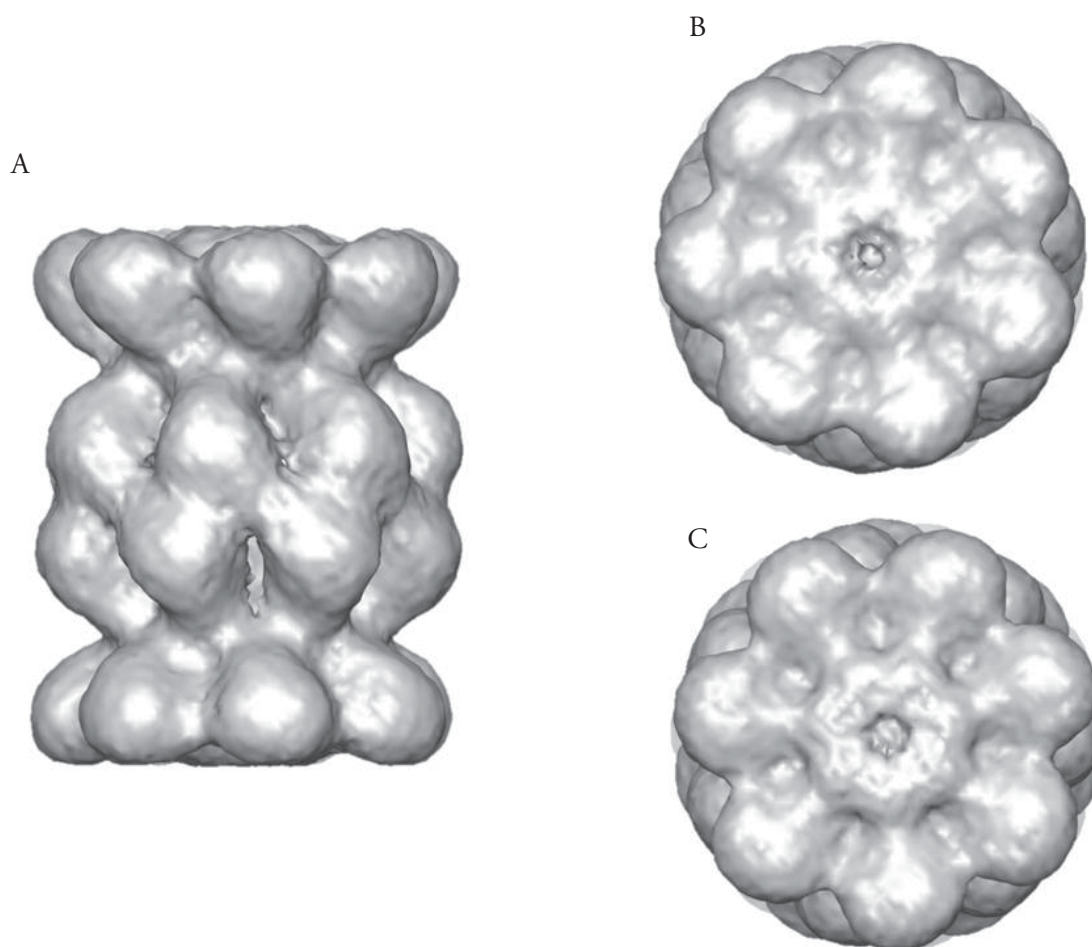


Fig. 3.22 3D reconstruction of the 20S proteasome. As with the single-capped 20S-PA28 proteasome, ~2000 side view images were used for the reconstruction, applying C7-symmetry and 5° references. (A) Side view. (B) Top view, suggesting a closed state. (C) Bottom view, suggesting a closed state.

Fitting of the crystal structure of the bovine 20S particle (pdbentry 1IRU) into the 3D reconstruction from the human 20S proteasome shows good correlation in size and shape (Fig. 3.23). From the side one sees that the α - and β -subunits convincingly fit the space available very good (Fig. 3.23 (A)). From the top and the bottom one sees that the N-terminal ends of the α -subunits fit into the mass that closes the central pore of the 20S proteasome (Fig. 3.23 (B) and (C)).

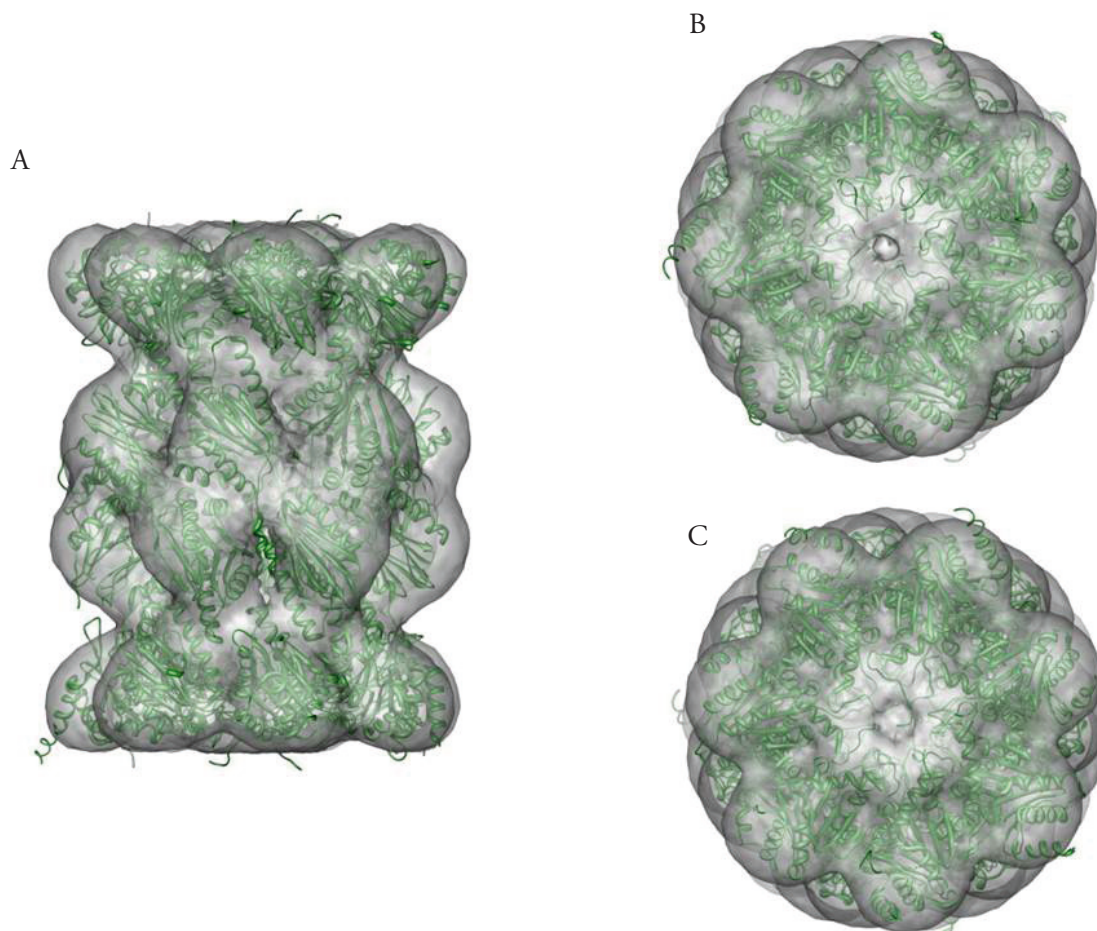


Fig. 3.23 Docking of the 20S proteasome with docked crystal structure. (A)-(C) Orientations as in Fig 3.26, but with the bovine 20S proteasome crystal structure (pdbentry 1IRU) docked.

3.4 Hepatitis B virus capsids

3.4.1 3D reconstruction of T3- and T4-assemblies

To assess the quality of the sample protein obtained from Dr. Thorsten Klamp negative stain EM was performed and a first 3d model was calculated. In negative stain images T3- and T4-assemblies were seen (Fig. 3.24 (A)). The diameter of the T3-assemblies was $\sim 40\text{nm}$ and of the T4-assemblies $\sim 50\text{nm}$. This was the expected size and the two forms could be discriminated by eye. After the sample was successfully evaluated ~ 300 particles were selected easily from each form and 3D density maps were calculated (Fig. 3.25 (A) and (B)). These two 3D reconstructions already show the characteristic spikes (Fig. 3.25 (A) and (B) red tips). In both reconstructions the spikes were at the expected positions of the symmetry axis and had the same size comparing T3 and T4. Both reconstructions could be refined to a resolution of about $\sim 25\text{\AA}$. At this resolution they showed similarity with previously published structures (Roseman et al., 2012) in terms of size and shape and thus were used as starting models for cryo-EM. From vitrified samples ~ 90 micrographs were recorded (Fig. 3.24 (B)). They were digitised to a final resolution of $1.3\text{ \AA}/\text{pixel}$. After selection of all particles and stack formation (appion) two data sets were available. A T3 data set with ~ 1900 particles (~ 340000 asymmetric units) and a T4 data set ~ 900 particles (fewer particles on the original images) (~ 210000 asymmetric units). As there were fewer particles in the T4 set a lower resolution was expected.

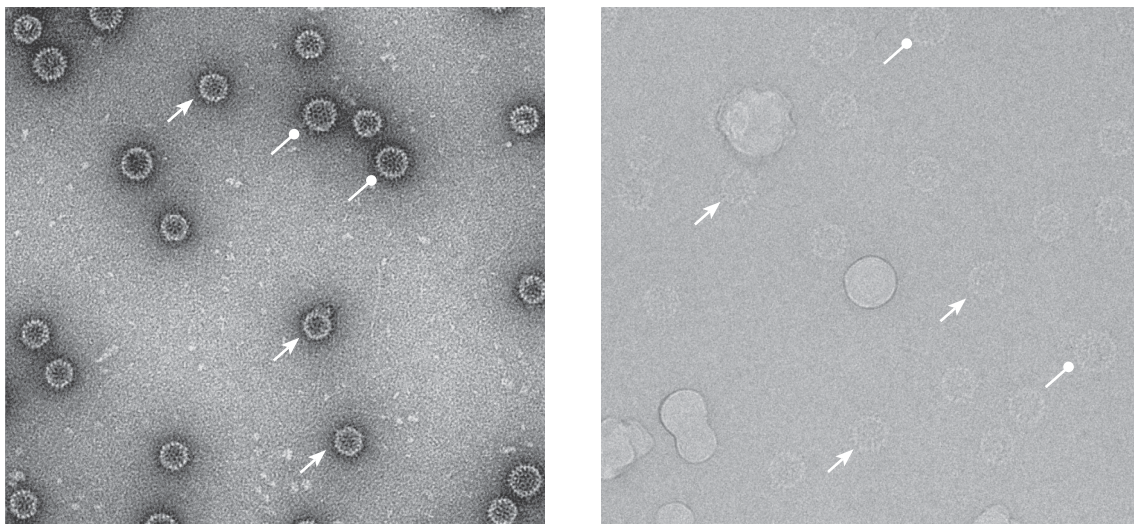


Fig. 3.24 Electron microscopy of HBV capsids. (A) negative stain clearly shows T3 (arrow) and T4 (round arrow) assemblies of the hepatitis B core proteins. The background seems to be very clean, indicating a high purity of the sample. (B) As in (A) but the sample was vitrified. Under vitrified conditions the particles could still be discriminated very well.

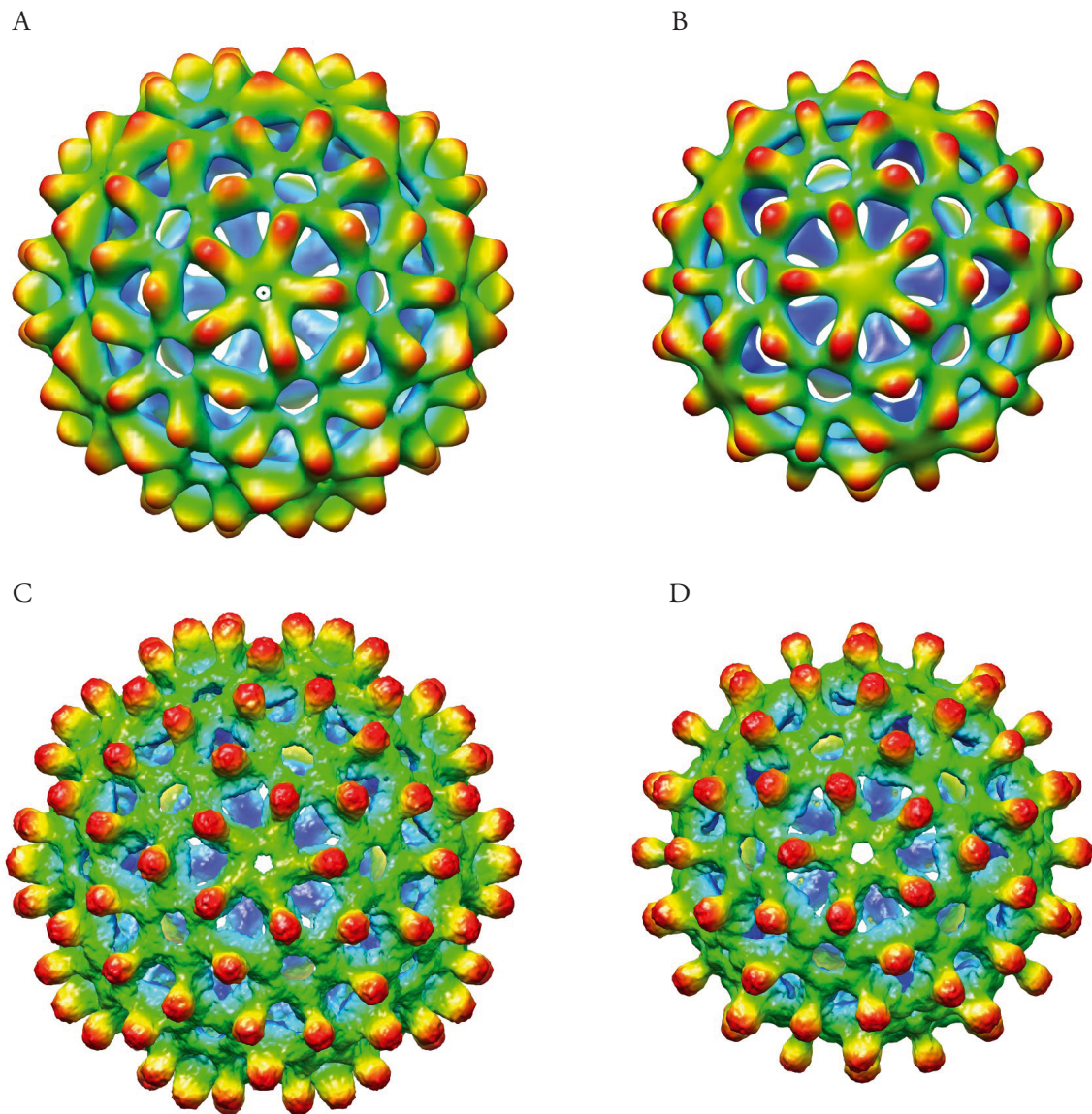


Fig. 3.25 Density maps from T3 and T4 HBV capsids. (A) and (B) 3D reconstruction of negatively stained samples of T4 (A) and T3 (B). Icosahedral symmetry was applied and the characteristic spikes appear. (C) and (D) Density map of a T4 capsid (C) and a T3 capsid (D) from vitrified sample. The spikes are more dominant and there are more structural features visible.

The cryo-EM particles were refined until no further improvement was seen (Fig. 3.25 (C) and (D)). The refined reconstructions show more elongated spikes and the overall structure seems to be more detailed. An additional pore can be seen in the center of the C_5 axis of the T3. However no rods can be seen. This would be expected as the protein complex consists of α -helices and loops only. Therefore an individual bFactor was applied (T3=-600, T4=-500) (Fig. 3.26 (A) and (B)), and rod like structures appeared especially in the T3 assembly. To evaluate if these rods are true α -helices, both models were automatically docked with the

crystal structure of a HBV core protein dimer (pdbentry1QGT; Wynne S. A. et al., 1999) (Fig. 3.26 (C) and (D)). It was found that all helices present in the crystal structure were accounted for with mass in the reconstructed models. Therefore I used the density maps and the resulting molecular models for further interpretation. To get a superior dimer the asymmetric units in the respective models were averaged (3.4.2).

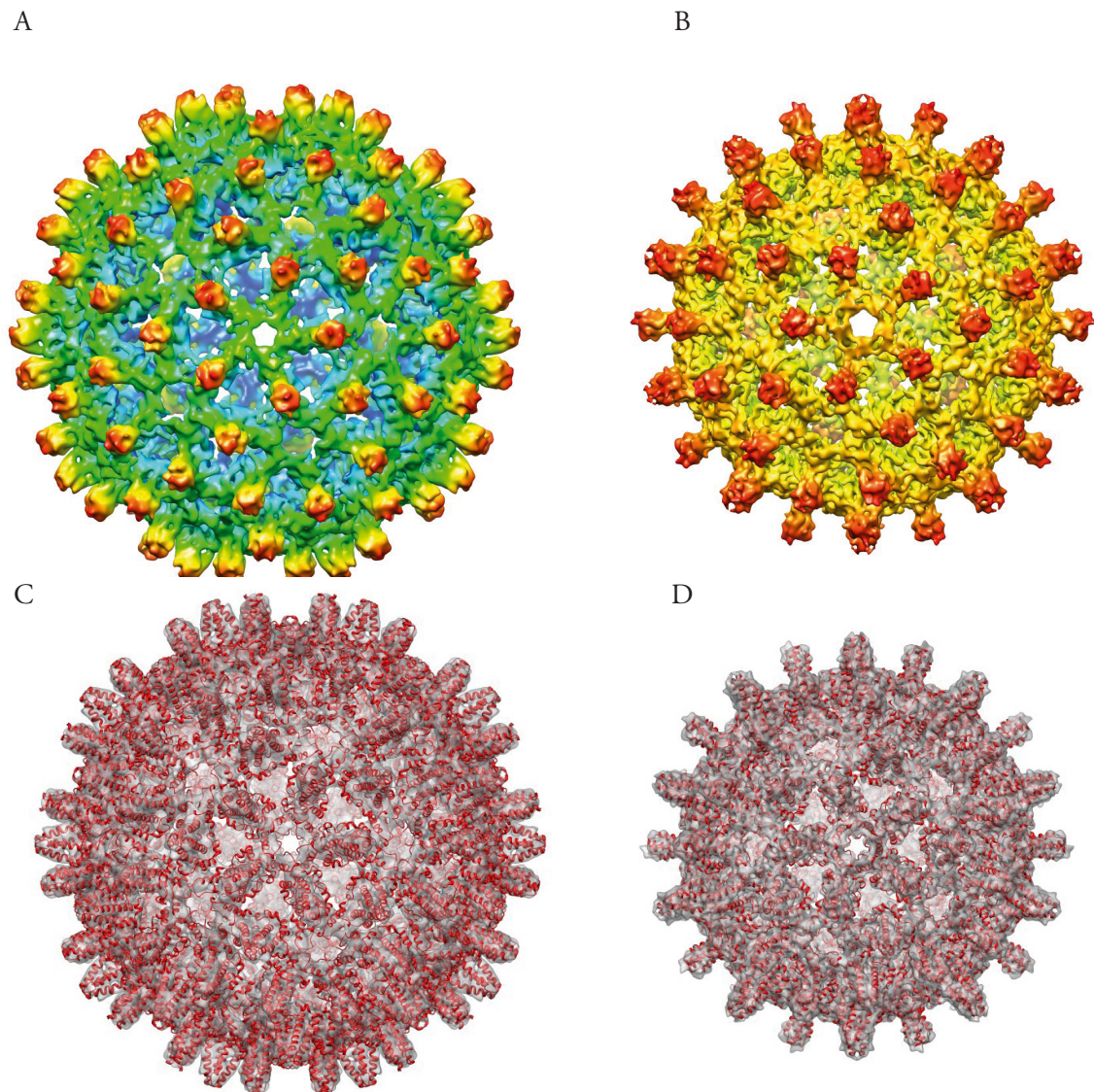


Fig. 3.26 Molecular model of T4 and T3 HBV capsids. (A) and (B) Density map of the T4 (A) and the T3 (B) capsid after application of a bFactor (T4=-500 to 8Å; T3=-600 to 7Å). (C) and (D) T4 (C) and T3 (D) docked with the molecular model. For T4 the molecular model published by Kramp et al., (2011) was used. For T3 an independent molecular model was developed (3.4.3).

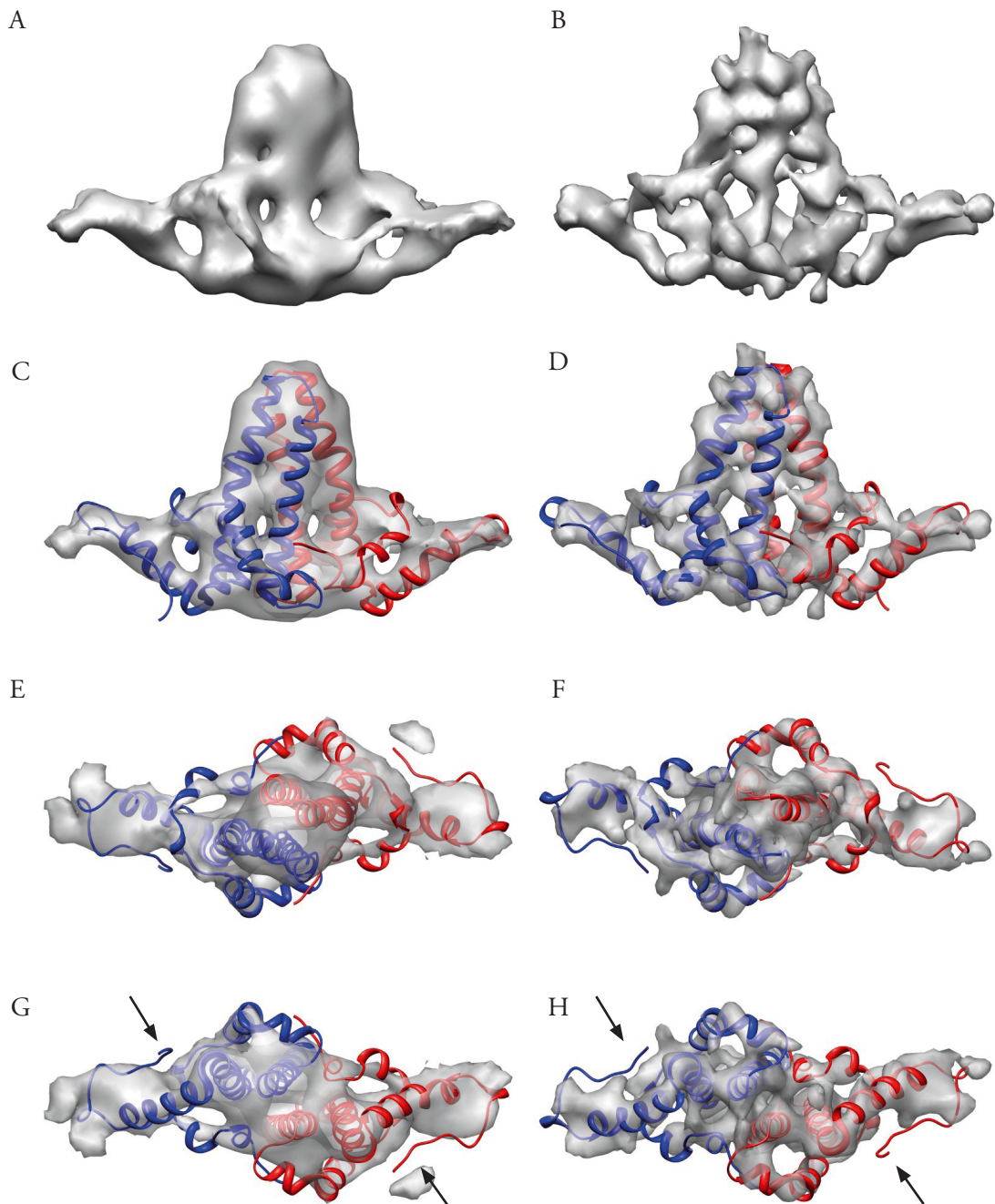


Fig. 3.27 Averaged dimer of T4 and T3. (A) Density map of the T4 capsid dimer after averaging all asymmetric subunits (UCSF Chimera *vop add*). There are rods and holes visible within the density map. (B) The T3 averaged dimer shows clear rods and very fine connections. After docking of the crystallographic dimer (pdbentry 1QGT) and looking at both dimers from different orientations (C)-(H) it became clear that the rods resemble alpha helices and the connections are not filled with proteins. Obviously the resolution of the T3-averaged dimer (right panel) is far better as all helical parts are clearly visible. Nevertheless it seems that the C-terminal part of the protein was not resolved (black arrow, (G) and (H)).

3.4.2 Averages of the asymmetric subunits

Comparison of the T4 and T3 capsid led to the assumption that the T3 assembly is better resolved than T4 as the rods are more elongated and the connecting bridges are thinner. To evaluate this and to receive a superior dimer the asymmetric subunits of the T3 particle and the T4 particle were averaged (UCSF Chimera). This resulted in better resolved structures with sausage like rods (Fig. 3.27 (A) and (B)). To evaluate the quality of the obtained structures the crystallographic dimer (pdbentry 1QGT; Wynne S. A. et al., 1999) was docked automatically. All helical parts of the crystal structure showed very good correlation with the rod-like structures from the reconstructed model. At various positions there are inter- and intra-domain bridges that are not filled with helices. As expected from the two capsid recon-

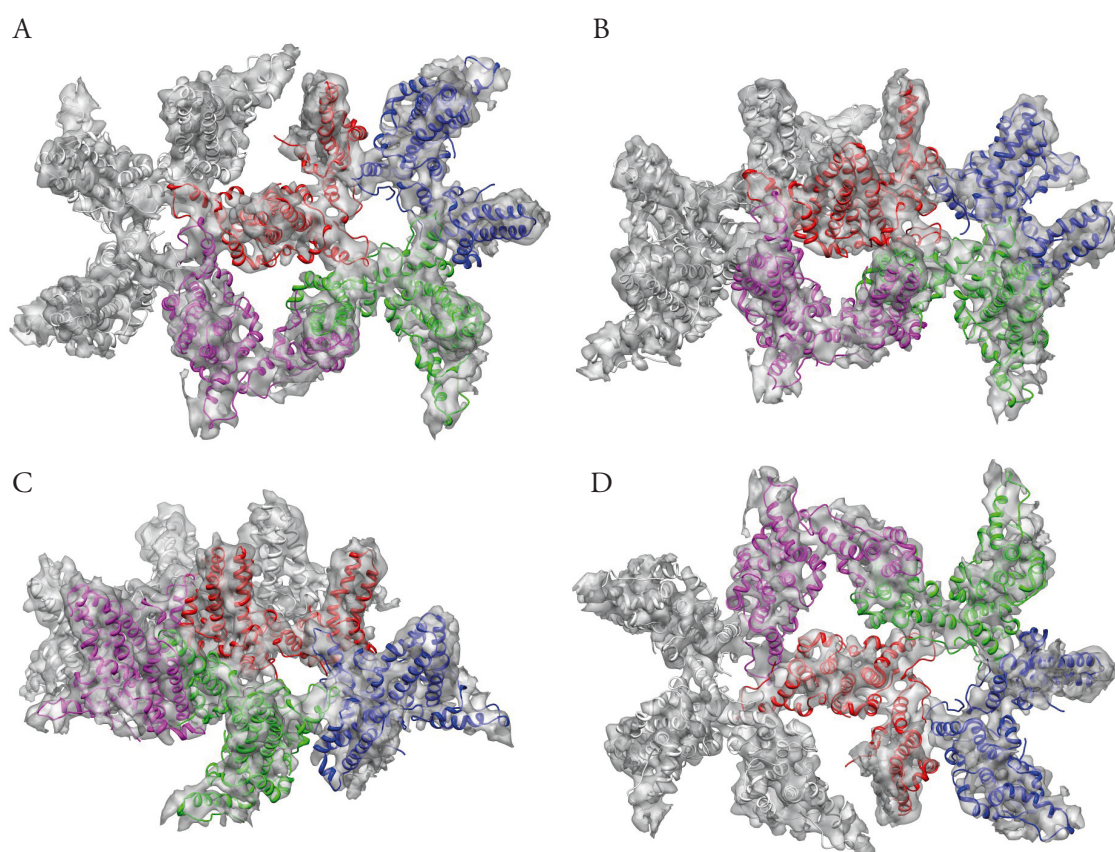


Fig. 3.28 Symmetry axes in the T3 capsid. (A)-(D) Different views of a cut out part of the T3 capsid with the C5 symmetry axis on the left and the C3 symmetry axis on the right (A). The spike docked with the red dimer resembles the C2 symmetry axis. The red, green and blue trimers form the basic building block of the T3 capsid and 20 of these form the entire capsid. The red, green and magenta trimers form (in parts) the asymmetric pseudo C3 axis. Note how well the crystal structures fit into the density map.

structions, the T3 dimer shows more details and is better resolved, although there were only three asymmetric units averaged in T3 and four in T4. But there are common features, too. Both dimers seem to be less good resolved at the tip where the inserted epitope is expected (Fig. 3.27 (A) and (B)) arrow) and at the position where the C-terminal end is expected (Fig. 3.27 (G) and (H) arrow). The most details seem to be resolved in the central part of the dimer. To study the extra bridges they were analysed according to interactions seen in the crystal structure (Wynne et al., 1999) or in mutation experiments (Ponsel and Bruss, 2003).

3.4.3 Structural details of the T3 capsid

As the T3 capsid showed higher resolution in comparison to the T4 capsid and its structure has not been solved experimentally as yet, all subsequent molecular analyses were performed on T3. As the crystal structure docked (pdbentry 1QGT) to evaluate the reconstruction (Fig. 3.26 (C) and (D)) does not contain a single dimer, but a tetramer. To determine the orientation of the crystallographic tetramer (pdbentry 1QGT) within the structure it was docked into the density map in different orientations and the cross correlation values (CCV) were measured. The orientation with the highest CCV was chosen, compared to the theoretical subunit arrangement described previously for T3 (Böttcher et al., 2006) and taken for further analysis. As there are only three monomers within the asymmetric subunit one monomer was removed from the crystal structure and individual trimers were docked into the T3 density map to form the entire assembly (see Fig. 3.26 (D)). Thereby a C3 axis was used as starting point for subunit docking.

Three trimers docked around the C3 axis form the basic building block for the entire T3 capsid and were used to produce the final molecular model. Automated docking (UCSF Chimera *fit in map*) of the basic building blocks resulted in CCVs over 90%. All helices of the crystal structures rest in rod like structures of the density map. Even turns are accounted for with mass. A docked C3 axis with a neighbouring C5 axis can be seen in Fig. 3.28. To enable further analysis of contacts between subunits docked as crystallographic trimer and non-crystallographic assemblies, the structure was further subdivided. The pseudo-threefold axis (formed by magenta, red and green trimers in Fig. 3.29) contains all three possible contact sites: within the C5 axis (magenta and red), within one crystallographic trimer (magenta and magent) and within the C3 axis (red and green). Looking at it in more detail reveals the interaction partners (3.4.5).

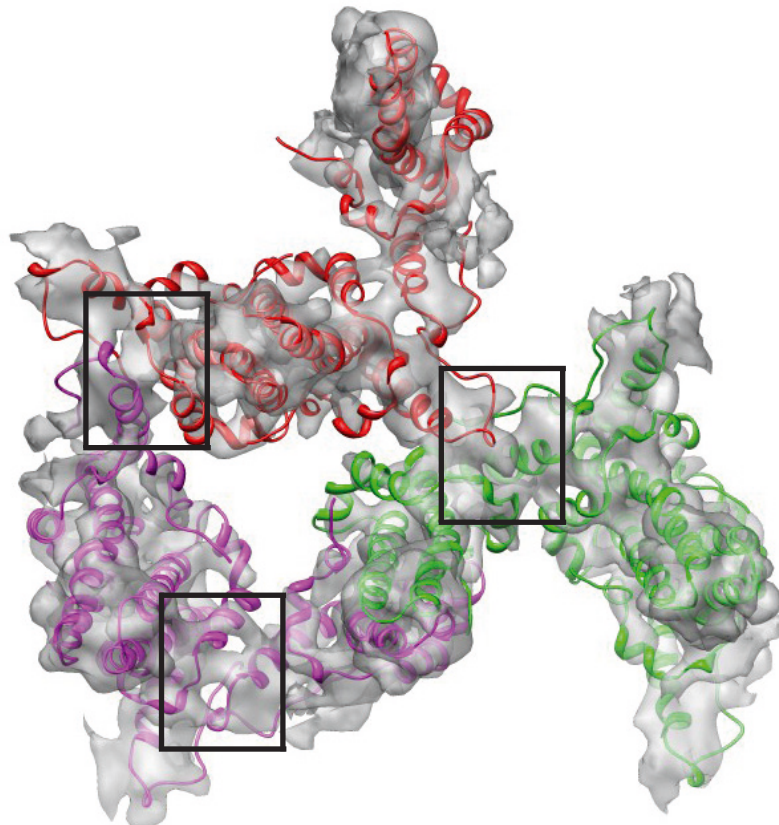


Fig. 3.29 Pseudo-C3 symmetry axis. View on the pseudo C3 symmetry axis that contains all contact sites formed by the dimers. The one in the C5 symmetry axis (magenta,red) and the two within the C3 symmetry axis (red,green and magenta, magenta) (boxes). These three contact sites are responsible for the non-covalent interactions taking place in the T3 capsid.

3.4.4 Connections between dimers in the T3 capsid

As direct interaction between neighbouring subunits is necessary for stability and capsid formation, the contact sites are of special interest. All three different connection types can be found in the pseudo-symmetry axis (Fig. 3.29). The connection in the C5 axis is found between the magenta and red subunit (Fig. 3.29 (A)). There is a big bridge (black arrow) that seems to be between to loop regions. In the magenta subunit this is the proline rich loop (Amino acids128-130) and in the red subunit this is the loop formed by Amino acids24-26. Moreover there seems to be a faint connection between the two helices present (round arrow). The helix in the red subunit is termed helix α_5 and the helix in the magenta subunit is termed helix α_2 (Wynne et al., 1999) and this nomenclature will now be further used as all contact sites are between these two helices. Without opacity one can see that all helices are well accounted for with mass (Fig. 3.30 (D)). The connection between two C3 axis trimers (red and green) seems to be of the same type C5 axis connection. There is a strong bridge be-

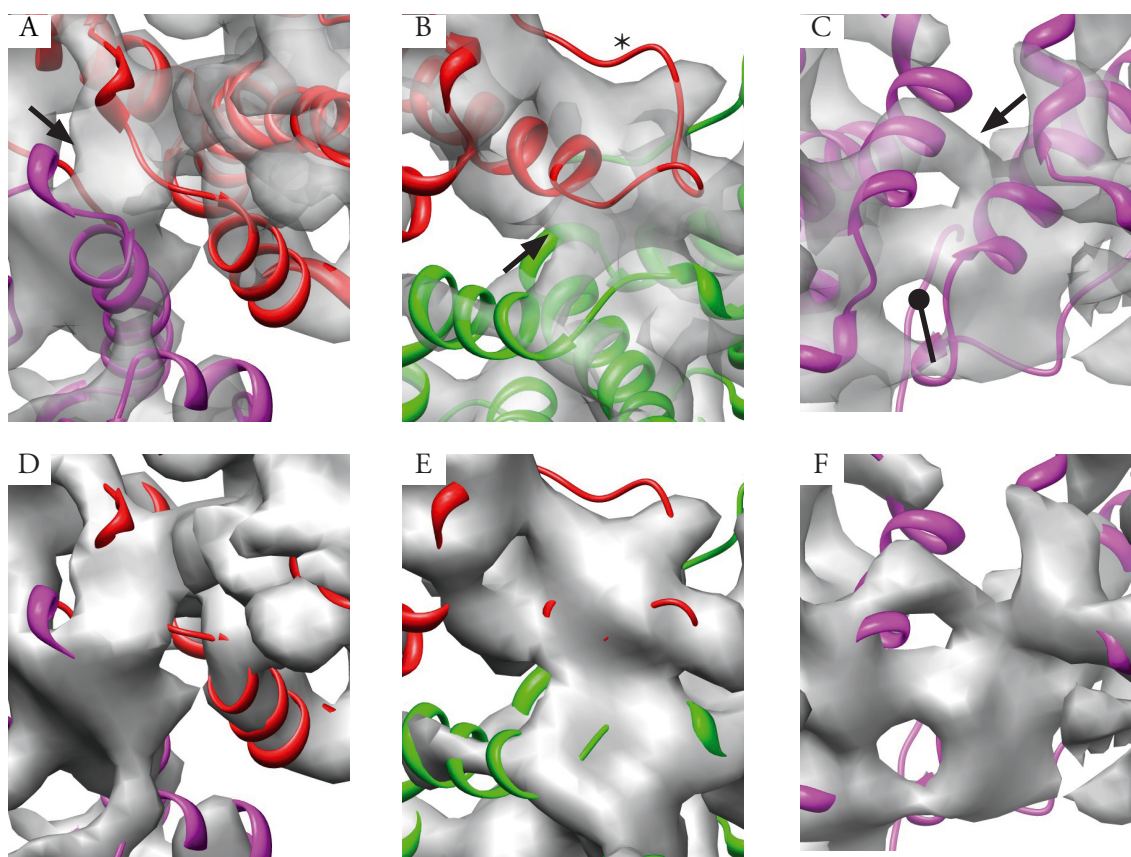


Fig. 3.30 Dimer connections in HBV capsids. (A) and (D) Connection between the subunits forming the C5 symmetry axis interface with and without opacity. There is one thick bridge (arrow) that is visible and there seems to be an other connection between helix $\alpha 5$ and $\alpha 2$ (round arrow). This bridge nevertheless is not very prominent as it is rarely seen. (B) and (E) The bridge that is formed within the C3 symmetry axis between subunits from non-crystallographic dimers is very prominent (arrow). In contrast to the C5 symmetry axis interface there is no further connection seen between $\alpha 5$ and $\alpha 2$. (E) and (F) Looking at the subunit interface formed in the C3 symmetry axis by dimers from the same crystallographic trimer reveals a different type. The connection in the loop region is thinner (round arrow) and there is a very clear connection between the two helices $\alpha 5$ and $\alpha 2$ (arrow). All close ups are in the same orientation and the same color code as in Fig. 3.29.

tween the two loop regions (arrow) and the upper regions of helices $\alpha 5$ and $\alpha 2$. Nevertheless at this threshold there is no further connection between the two helices detectable. Again all helices in the crystal structure are accounted for with density, except for the C-terminal end (asterisk)(Fig. 3.30 (E)). The third unique connection is in between two subunits from the same crystallographic trimer. It differs from the two others, as a clear connection between $\alpha 5$ and $\alpha 2$ (arrow) is present. Moreover the connection between both loops seems to be thinner (round arrow) and there is an extra connection at the end of the two loops. To further analyse these connections the Amino acids present in this region have to be looked at.

3.4.5 Resolution of the inserted epitope

One of the main questions was whether there is a defined structure found for the inserted tumor-like-epitope, or whether it is unstructured as in the T4 capsid (Klamp et al., 2011). Therefore it is necessary to look at the top of the spike (region of the insert; red tips in Figs. 3.25 and 3.26) at different threshold levels (Fig. 3.31). This was done using the three spikes found around the pseudo-C3-symmetry axis as all three monomers are present there. It seems as if extra mass is present in the upper region of the spike. Nevertheless it fades after increasing the threshold value. As in the averaged dimers (Fig. 3.27 (A) and (B)) it appears as if the upper region of the spike has a lower resolution.

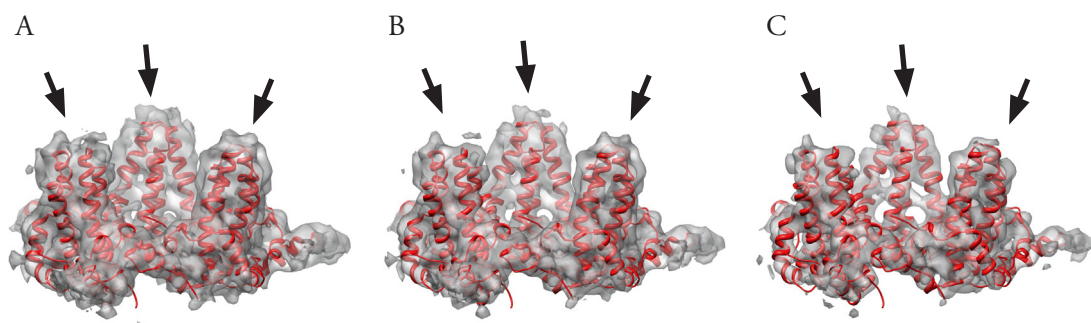


Fig. 3.31 Pseudo-C3-symmetry axis at different threshold levels. (A)-(C) At different threshold levels (A:low;B:medium;C:high) it becomes clear that at the expected position (arrows) only diffuse extra mass is visible. At low threshold there is a certain mass there, but it does not account for the expected ~30 amino acids that are present in the insert. At the highest threshold level only very faint masses are present and it almost appears as if no extra mass was there. Nevertheless the resolution in the upper parts of the spikes seems to be lower than in the central parts. This suggests that the extra peptides are very flexible.

4 Discussion

4.1 Arthropod 2x6mer hemocyanins

4.1.1 Decapod 2x6mer hemocyanins

In this work three hemocyanin 2x6mers from different decapods (*Astacus leptodactylus*, *Carcinus maenas* and *Homarus americanus*) were analysed. The obtained reconstructions are all in the same resolution range ($\sim 25\text{\AA}$) and can therefore be well compared. Although there are different offsets between the docked hexamer centres (1-5nm) this might not be significant at the present resolution. The rotation of the two hexamers towards each other was measured to be between 85° and 100° . To evaluate if the rotational differences can be described at the current resolution, the perimeter of a circle around the centre of a hexamer (radius = 5nm) was calculated. This perimeter is $\sim 155\text{\AA}$ and therefore one degree equals a distance of $\sim 2\text{\AA}$. At a rotation angle of 15° two points are 30\AA apart. This maximum difference is slightly above the present resolution limit (25\AA). Nevertheless it would be speculative at this point to state that different rotation angles exist between the three hexamers. This requires a higher resolution using cryo-EM images. Although the translation between the hexamer centers is slightly above the resolution limit staining artefacts can not be excluded and this would also require cryo-EM. Therefore I will refer to the “decapod-type” of 2x6mer if the major bridge is formed by two square faces and the two hexamers are rotated by about 90° with respect to each other. The docked density maps reveal that, in all three molecules, the connecting motive is the 7-stranded β -barrel (Figs. 3.4, 3.5 and 3.6).

Comparing the obtained orientation of the two hexamers with a previous study (Micetic et al., 2010) reveals that both models are in good concordance. As tomographic reconstructions were used as independent starting models from the respective species, starting model bias can be excluded. However the use of Chelicerata hemocyanin as starting models for crustacean 2x6mers as described (Micetic et al., 2010) is rather critical as these hemocyanin types evolved convergently from 1x6mer ancient hemocyanins (Burmester, 2001; Rhem et al., 2012). It is especially critical that only 380 particles were selected and no independent *ab-initio* model was calculated (Micetic et al., 2010). In contrast, the present 2x6mer hemo-

cyanins from different decapod species were calculated from unbiased starting models and can now be used as starting models for 3D-cryo EM approaches.

4.1.2 *Odontodactylus scyllarus* 2x6mer hemocyanin

The 2x6mer of *O. scyllarus* (Fig. 3.9) belongs to the mantis shrimp (stomatopod) hemocyanins. Previous studies already suggested the architecture of the 2x6mer hemocyanin of *Squilla mantis* (Bijlholt and van Bruggen, 1986; Micetic et al., 2010). For *O. scyllarus* EM images indicate the same 2x6mer arrangement (Scherbaum et al., 2010). From the 3D density map obtained during this work I was able to find similarities and differences to the previously published data. The contact interface, as described for *S. mantis*, is formed by two hexagonal faces (Bijlholt and van Bruggen, 1986; Micetic et al., 2010). In our 3D model the two particle centres show a distance of 4.5nm. This finding is in agreement with Bijlholt and vanBruggen (1986) where this distance can be measured in 2D class sum images, but does not fit with results of Micetic et al., (2010) where 6.6nm were measured. As they used a 2x6mer half-molecule (hexamer-hexamer distance 6.5nm) from the tarantula *Eurypelma californicum* as starting model this might have effected the structure obtained.

As the 3D model presented in this work was obtained from an tomographic starting model, starting model bias can be excluded. This and the good agreement with previous data (Bijlholt and van Bruggen, 1986) indicates that the 2x6mer hemocyanin from stomatopods shows a different architecture than the 2x6mer half-hemocyanin from *E. californicum*. Nevertheless, to fully elucidate the structure at higher resolution 3D-cryo EM has to be conducted.

The 2x6mer from the isopod *Ligia oceanica* solved in our group showed a distinct architecture (Fig. 4.1). Again, the contact is formed by the hexagonal faces of the hexamers. However, the hexamers are not shifted against each other, but overlap completely. They are tilted so that the contact is formed by two subunits from each hexamer only.

4.1.3 Comparison of the studied 2x6mers to a crustacean 4x6mer

Another crustacean hemocyanin structure solved in our group was the 4x6mer from the thalassinid ghost shrimp *Callinassa truncata* (C. Kühne and J. Markl, unpublished). Previous studies already suggested a different 4x6mer architecture in crustaceans to that in chelicerates (Cavellec et al., 1989; Martin et al, 2007; Markl and Decker, 1992). It was therefore interesting to see if single 2x6mers from crustaceans fit into the higher oligomer. All three 2x6mer architectures defined here (decapod-type, stomatopod-type and isopod-type) were compared to the 4x6mer structure. Surprisingly, the decapod-type and the isopod-type both showed good correlation with different aspects of the ghost shrimp 4x6mer (Fig. 4.2).

From this finding an evolutionary pathway can be hypothesised. The ancestral form was a 4x6mer that split into 2x6mers when the isopods branched of. When the decapods evolved the 4x6mer divided again, but in another manner. Only the ancestors of the thalassaid shrimps kept the 4x6mer (Fig. 4.3).

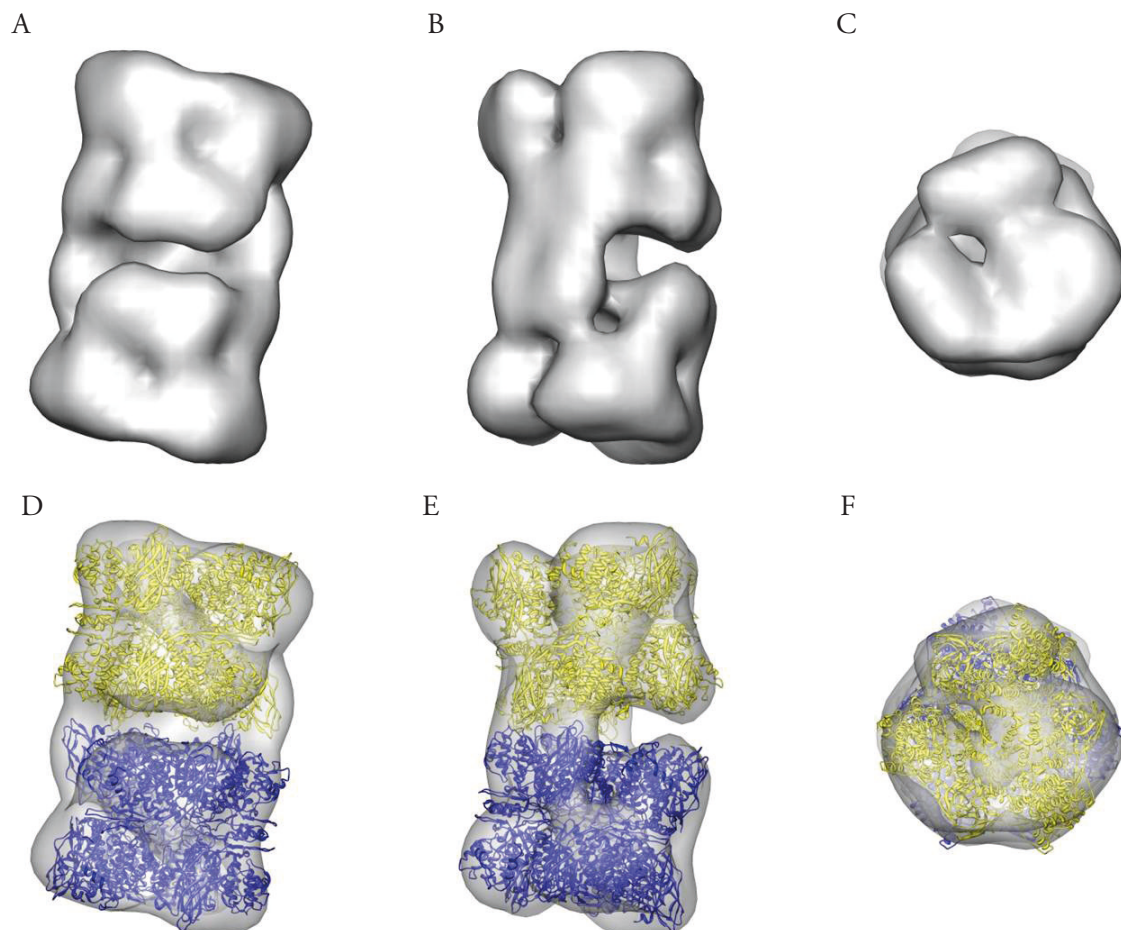


Fig. 4.1 Isopod 2x6mer hemocyanin. (A), (B) and (C) Different views of the density map of the 2x6mer hemocyanin from the isopod *L. oceanica*. (D), (E) and (F) same as (A)-(C) except density maps are visualised transparent and docked with two hexamers (pdbentry 1HCY). Notice the tilt between both hexamers, leading to a contact between two subunits per hexamer (E) (3D reconstruction produced by C. Gatsogiannis).

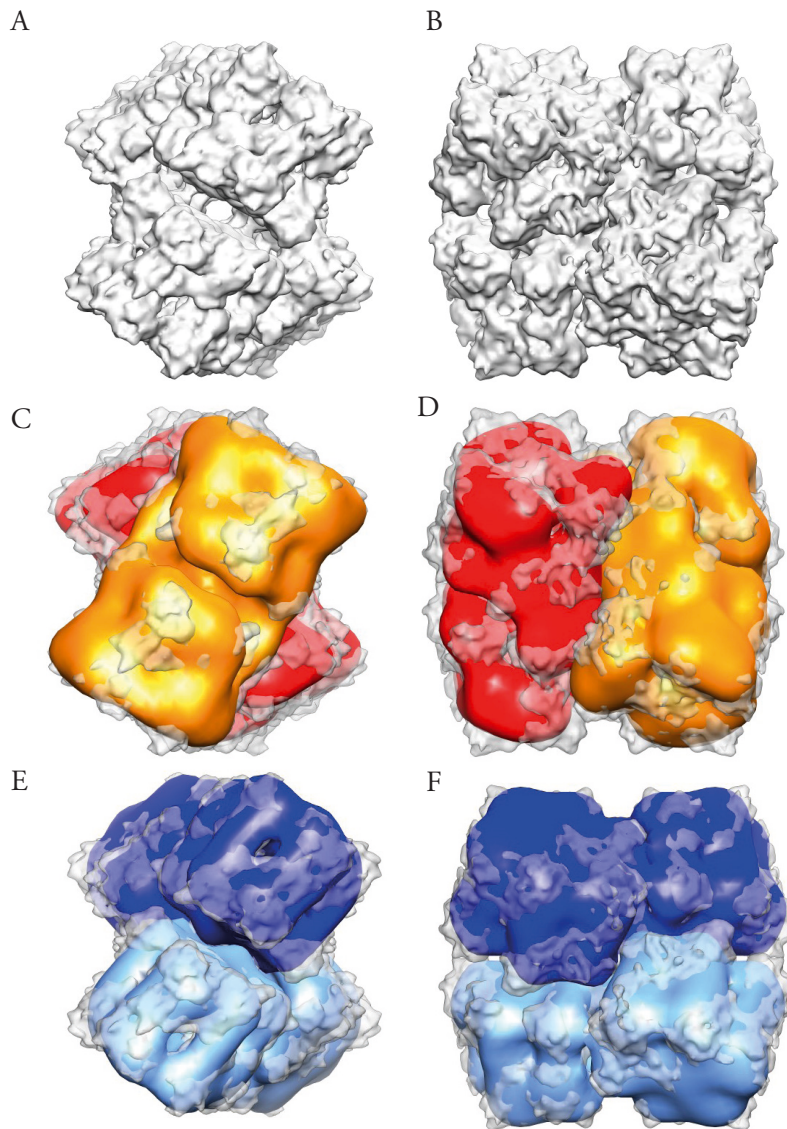


Fig. 4.2 Comparison of crustacean 2x6mer hemocyanins with the 4x6mer hemocyanin from the thalassinid shrimp *C. truncata*. (A) and (B) Density map of the 4x6mer *C. truncata* (C. Kuehne and J. Markl, unpublished). (C) and (D) as in (A) and (B) docked with two isopod-type 2x6mer hemocyanins (red, orange). (E) and (F) As in (A) and (B) docked with two decapod-type 2x6mer hemocyanins (blue and light blue). Both 2x6mer types fit the 4x6mer density map well. Due to the docking process the as yet undefined handiness of the 2x6mer reconstructions became clear.

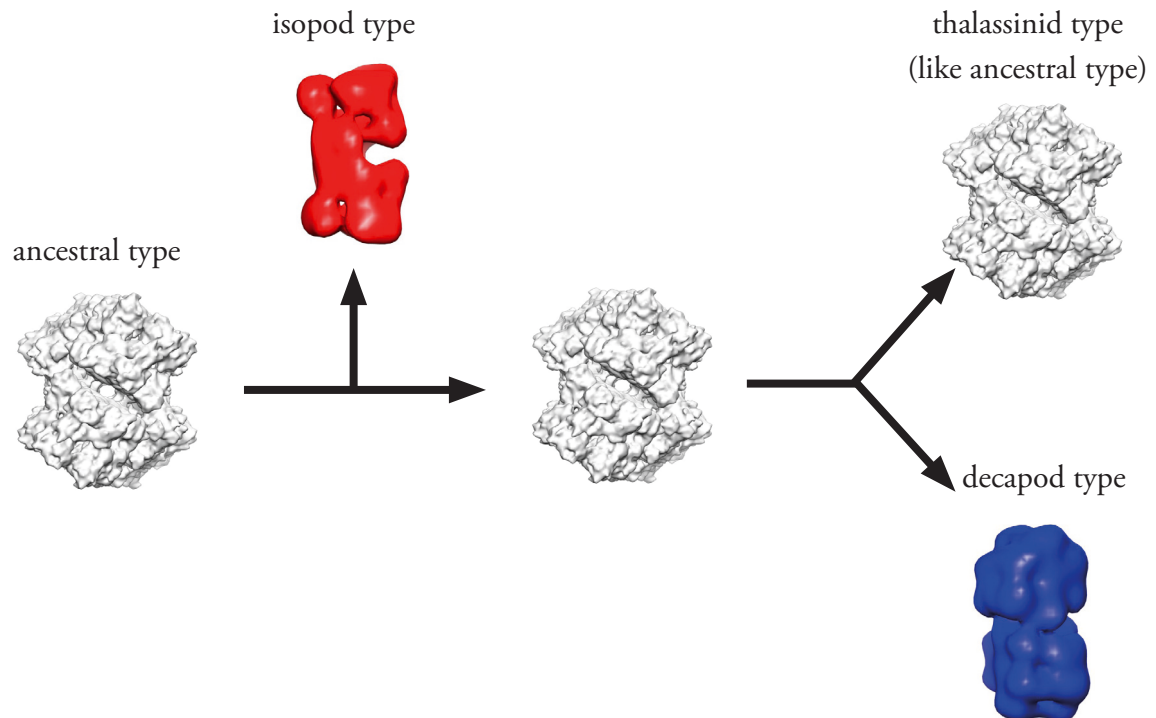


Fig. 4.3 Hypothetical evolution of decapod hemocyanins. From the structural analysis of the density maps received from decapods, isopods and the ghost shrimp *C. truncata* an hypothetical evolutionary pathway can be developed. The ancestral form was the 4x6mer type still present today in thalassinid shrimp. When the isopods branched off the 4x6mer was reduced to 2x6mers of the described type. Later the 4x6mer was reduced again when the decapods developed, but in a different manner. Thus there are three different architectures found that originated from the same starting structure. The decapod-type 2x6mer, the isopod-type 2x6mer and the thalassinid-type 4x6mer.

4.2 Envelope proteins from HIV

To assess the quality of the reconstructed density maps for NL4-3 and Ada the FSC should not be the only measure. In both cases models of the same size and mass were reconstructed with three clearly separated masses. As both density maps were derived from the same starting model, they resemble their individual data sets. To further evaluate the reconstructed models they were compared to published density maps from Env-proteins (Zhu et al., 2006; Wu et al., 2010; White et al., 2010; Zanetti et al., 2006; Moscoso et al., 2011; Liu et al., 2008). For the gp120 part all reconstructed models show three distinct masses. Some are closed at the top and show more cage like structure and others are more open at the top, but with a central mass as the models presented here. For the gp41 part there are two groups: one with one central stalk at the bottom and the other with three “legs”. The density maps from NL4-3 and Ada show three distinct masses that merge at the bottom. It is not known in our constructs whether the gp41 part is in pre- or post-fusion conformation.

Additionally, docking of a molecular model should be a measure for the quality of the reconstructed density. As there is only reliable conformation information for the gp120 part of the molecular complex a molecular model was produced and docked into the obtained structure automatically. As the molecular model was produced from different crystallographic structures, it was evaluated for consistency. Especially the fusion of the V3 loop to the rest of the gp120 structure is of interest. As there are numerous amino acids, overlapping between the V3 loop crystal structure and the unliganded gp120 core fusion was rather easy. Nevertheless, that the V3 loop resembles a CD4 bound state. At the same time there is no crystal structure available from an unliganded gp120 resolving the V3 loop. As the conformation of the gp41 part is not known, only rods were docked into the empty densities, with the fusion peptide connected to the gp120 part of the complex. Altogether the docked structural elements fit both reconstructions well in size and shape, and therefore, a reliable orientation for the gp120 parts of the molecular complexes were found. To further confirm the orientation of the docked gp120, immuno-electron microscopy was performed. Therefore mAb447-52D was used as it targets an epitope in the V3-loop region. From the NL4-3-447-52D complex, a reconstruction was conducted and extra mass appeared at the upmost tip of the density map (Fig. 3.14). This extra mass resembles the docked antibody. With this extra mass the molecular model developed here was supported and the orientation of the V3 loop was independently shown. Nevertheless, confirmation of this model requires a superior map to be developed.

Comparison of the two density maps reveals that the gp41 part of them has the same orientation (Fig. 3.12 (C)). The gp120 part on the other hand seems to be rotated inward by about 40° in the Ada reconstruction compared to NL4-3 (Fig. 4.4). Moreover the entire density map of Ada seems to be more compact. As previously published data suggested a more

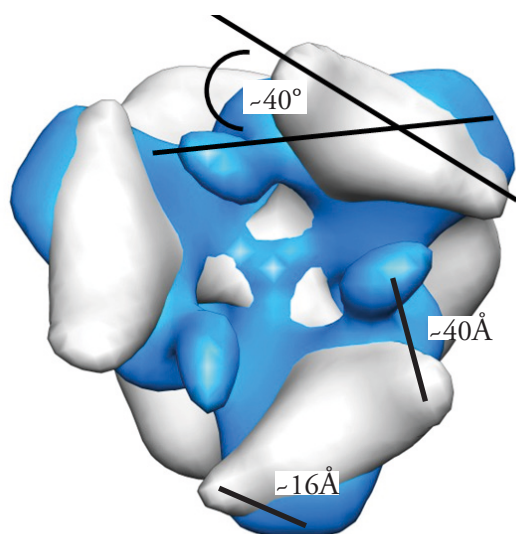


Fig. 4.4 Comparison of NL4-3 and Ada gp120 parts. From the top the angle between NL4-3 (grey) and Ada (blue) becomes evident. It was measured to be $\sim 40^\circ$. The distance between the two tips is $\sim 40\text{\AA}$ and the two V4/5-loop regions $\sim 16\text{\AA}$.

free gp120 molecules, structural details cannot be described. Nevertheless it is suggested that only one CD4 molecule binds to the trimer and leads to a transition of the entire complex. It still remains unclear if this transition is fully comparable to those found in cleaved Env trimers that clearly bind three CD4 molecules (Liu et al., 2008; White et al., 2010; Harris et al., 2011; Wu et al., 2010).

Altogether the presented data suggest that R5- and X4- dependent HIV Env proteins display different conformations in their gp120 part. The R5-dependent strand, Ada, might display a more closed conformation than the X4-dependent strand NL4-3. In addition it appears for NL4-3 that occupation of one CD4 binding site leads to conformational changes that exclude binding of further CD4 molecules to neighbouring gp120 molecules.

closed conformation for R5 viruses (Naganawa et al., 2008; Zhuang et al., 2011) this finding is consistent.

Additionally it was interesting to see how structural changes resulting from interaction with CD4 (natural primary receptor) could be followed in negative stain. Therefore NL4-3 was incubated with a four domain CD4 and a density map was calculated. Although structural changes were observed there was only very little extra mass present in the C3-symmetric reconstructions (not shown). As it was suggested for uncleaved SIVmac gp140 that only one CD4 binds (Kim et al., 2001) (Zhang et al., 2001), an asymmetric reconstruction was performed. Both, class sum images and the density map, showed only one extra mass (Fig. 3.16). Due to the inferior resolution of the density map and the unclear transition state of the CD4-

4.3 The 20S and 20S-PA28 proteasome

4.3.1 Preparation and image acquisition of the proteasome sample

The sample obtained was evaluated under negative stain conditions. It became clear that only side view particles could be used. These allowed to discriminate between capped (20S-PA28) and uncapped (20S) particles (see Fig. 3.17). In negative stain images only very few 20S particles with an additional cap were found. To check whether the capped particles probably are mostly in top view the sample was vitrified and images were taken (not shown). Also under cryo-EM conditions the problem was that very few particles could be assigned as capped. Therefore it was decided to use the negative stain method as this is faster and particle classification can be done easily. Unfortunately, from ~170000 automatically selected particles only ~2000 clearly capped side view particles could be manually selected (examples in Fig. 3.18).

4.3.2 Evaluation of the 3D reconstructions

The 3D reconstructions of the 20S and the 20S-PA28 proteasome complexes both yielded resolutions at around 18Å. As for both the same number of particles (~2000) and the same symmetry (C7) was applied and as moreover, the particles were collected from the same images, the results should be well comparable. Nevertheless the question arises if a seven-fold symmetry can produce trustworthy results for pseudo-symmetrical complexes. For the 20S molecule a C2 symmetry and for the 20S-PA28 complex no symmetry at all would be correct, because of the fact that seven different subunit types are involved. In previous work (Nickell et al., 2007), reaching the same resolution range, the 20S proteasome was calculated with a D7 symmetry and showed a convincing correlation with the crystal structure. The crystal structures of the bovine 20S proteasome (Unno et al., 2002) and the yeast 20S proteasome (Blackburne et al., 2010) reveal that the differences between the single subunits are mainly on the secondary structure level. Therefore at a lower resolution the 20S proteasome can be calculated with a pseudo-symmetry.

To fully exclude a symmetry bias, asymmetric reconstructions were conducted and compared with the symmetrical ones (Fig. 4.5). Measuring the correlation value between the respective C7 and asymmetric reconstructions yielded correlation coefficients >0.99 for the 20S particle and >0.98 for the 20S-PA28 particle. Therefore it was assumed that the application of the pseudo-C7 symmetry did not create artefacts at the present resolution level.

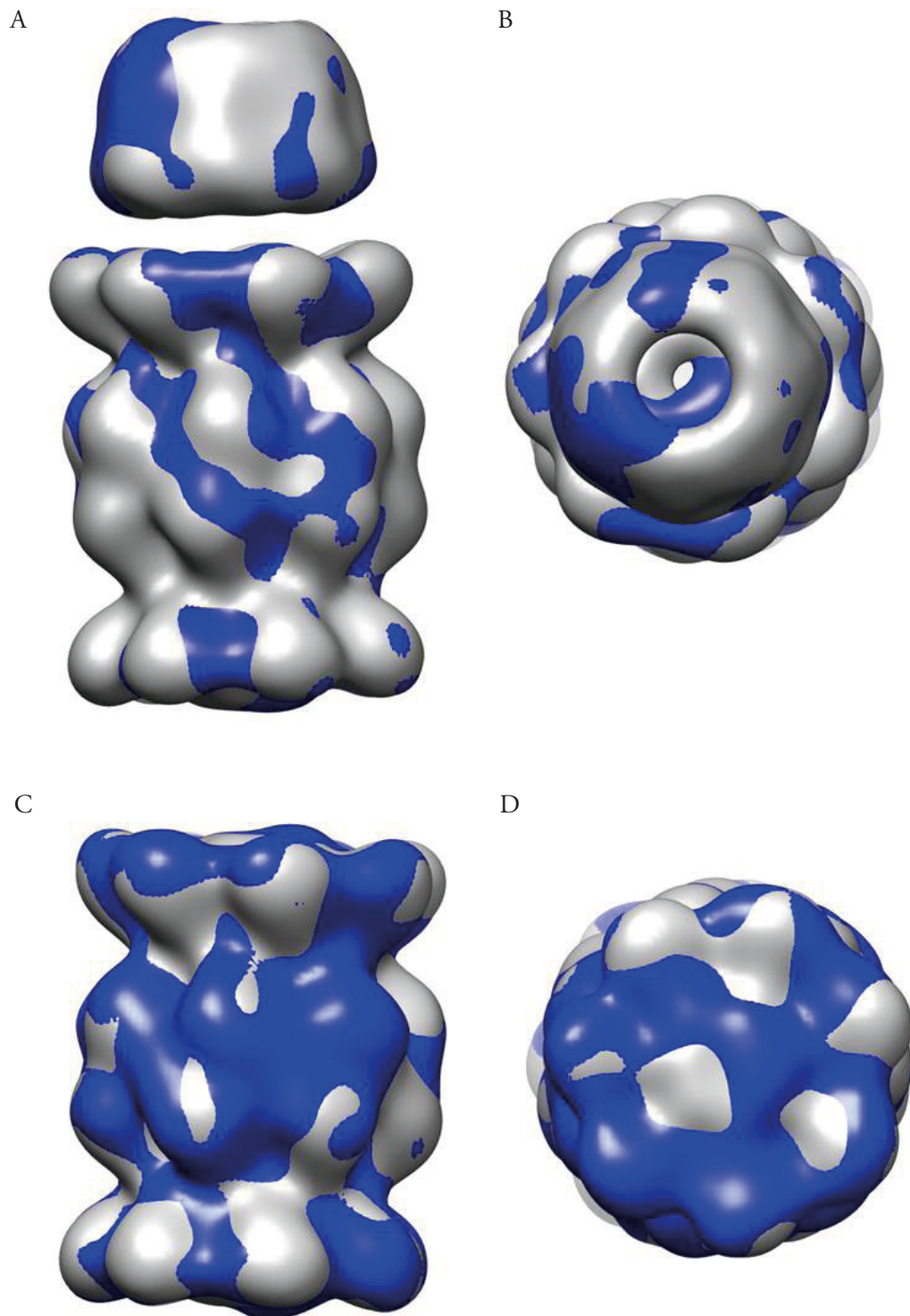


Fig. 4.5 Comparison of symmetric and asymmetric proteasome reconstructions. (A) Side view and (B) top view of near mass threshold 20S-PA28 complex. Grey with C7-symmetry and blue without symmetry applied. The correlation between both models is >0.99 . (C) Side view and (D) top view of the 20S proteasome with the same color code as in (A) and (B). The correlation between both is >0.98 .

The next question was whether the opening seen on one side of the 20S-PA28 complex and the equal mass distribution on both sides of the 20S molecule are consistent at different threshold values. One threshold was chosen nearly mass corrected and one was where faint connections between 20S core and the PA28 activator became visible (see Fig. 3.21 (A)). For the 20S-PA28 complex there is an opening in the capped part of the 20S particle, thus the upper gate seems to be open (Fig. 4.6 (A)). The uncapped part of the 20S core particle seems to be in the closed conformation. In the 20S proteasome both openings show approximately the same mass in both threshold values (Fig. 4.6 (B)). Therefore we assume the same conformation for both gates. Docking of the crystal structure of the bovine proteasome (pdbentry 1IRU; Unno et al., 2002) into the 20S reconstruction yielded a correlation value of 0.84. For the combined model, consisting of half a bovine 20S structure and half a yeast 20S with the *Trypanosoma* PA26 activator (pdbentry 1FNT; Whitby et al., 2000), a CCV of 0.88 was measured after docking into the 20S-PA28 complex. Docking the whole bovine 20S and the PA26 activator yields a CCV of 0.86. As the only difference is the closed conformation on both sides of the 20S particle, this could be the reason for the slightly higher CCV, indicating a better fit.

The combined model docked into the 20S-PA28 reconstruction at near mass threshold (Fig. 4.7) reveals that the open gate of the PA26 (red) activated 20S (blue) particle fits the opening of the complex. The lower part of the reconstruction, where no opening appears, the bovine half 20S proteasome (green) fits the available mass. This visual confirmation of the measured cross correlation values is an indication that the combined model might be more realistic.

As the main mass disappearing at higher threshold in the 20S-PA28 complex is at the capped gate, I assume higher flexibility here (e. g. Lariviere et al., 2012). Although the opening of the gate enhances the overall activity of the 20S proteasome and the amount of double cleaved products (Kloetzel et al., 2001; Strehl et al., 2005; Klotzel et al., 2004; Dick et al., 1996), the opening of the gate seems not to be an exclusively physical event. There seems to be interaction between the substrate and the activator/gate region, as some substrate specificities are not altered upon activation of the 20S proteasome by PA28 (Mishto et al., 2008). This finding agrees with the data shown here as the capped gate is not very well resolved and the mass disappears at first there at higher threshold levels. Looking at the crystal structure of the 20S-PA26 reveals that up to 15 amino acids (e.g. α -subunit type six) were not resolved in the N-terminal region of the α -subunits. For the activation of the 20S proteasome by Blm10 (another 20S activator) it was shown that the N-terminal ends of the α -subunits are moved from the central pore, but form a different conformation as upon activation with PA26 (Sadre-Bazzas et al., 2010). This is an other indication for the high flexibility in this region. It cannot be excluded that the N-terminal ends function as a gate that displays more than

one conformation and that sorts the preferred peptides upon length and sequence (Mishto et al., 2008).

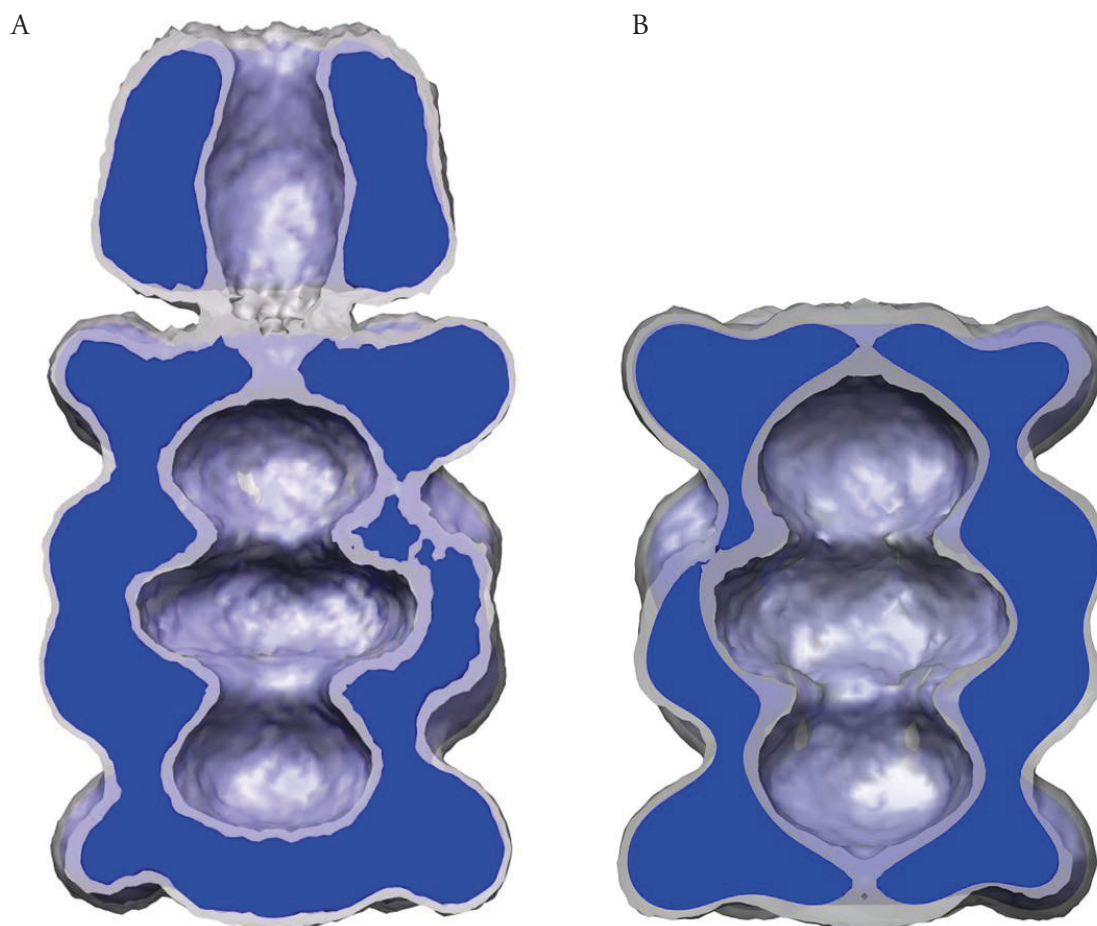


Fig. 4.6 3D density maps of the 20S-PA28 complex and the 20S proteasome at different thresholds. (A) 20S-PA28 complex and (B) the 20S proteasome. Density maps are superposed at two different threshold values (blue, approximately mass corrected; grey, higher) as applied in Fig. 3.21 (A) and (B), respectively. Note that top and bottom of the 20S-PA28 complex clearly differ in mass (A), whereas they are approximately equal in the 20S molecule (B). This is particularly obvious at mass-corrected threshold (blue).

4.3.3 Conclusions on function and structure of the 20S-PA28 complex

At the resolution of the reconstructed models ($\sim 18\text{\AA}$) it is not possible to describe any details at the secondary structure level. Nevertheless some structural features can be deduced from the present model. It appears that docking of an activator complex to one side of the 20S proteasome opens only the gate at this side. Moreover one can speculate that attachment of

the activator induces some flexibility in the 20S proteasome. This is supported by the finding that the N-terminal ends resting there after docking of the combined molecular model are not fully resolved in the crystal structure.

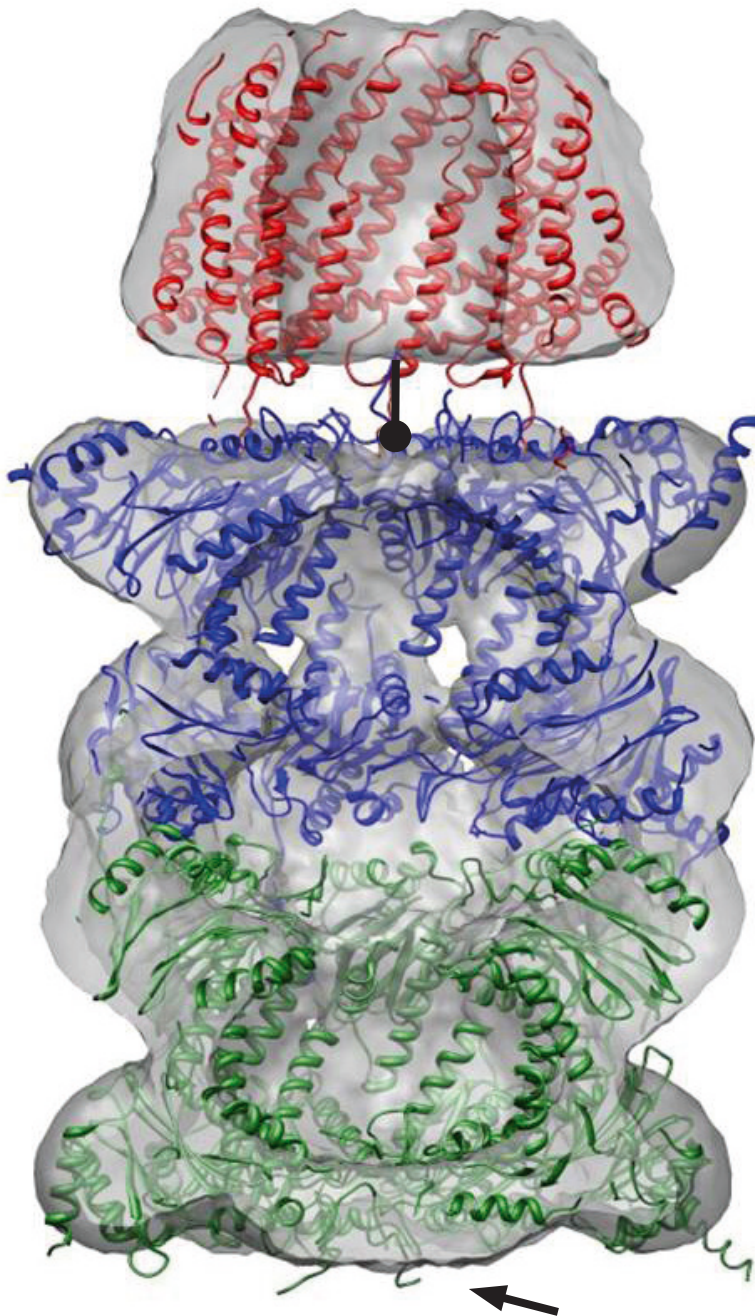


Fig. 4.7 Cut-open view of the docked 20S-PA28. In the cut-open view docked with the bovine proteasome structure (green) and the PA26 (red) activated yeast proteasome structure (blue) the uncapped gate is closed by the N-terminal regions from the α -subunits (arrow). The capped gate is open and forms a pore (round arrow). The connection between 20S core and PA28 activator are not resolved at this threshold (mass corrected).

4.4 Hepatitis B virus capsids

4.4.1 Evaluation of the T3 capsid

The nominal resolution obtained in the FSC is not the only quality measure of a structure. A second criterion is the comparison of the resolved density map with the docked crystal structure (pdbentry 1QGT). Here the cross-correlation value was measured (UCSF Chimera module *fit in map*) with the pdbentry-model filtered to 6.5Å. This resulted in a correlation of ~89%. Considering that there is a long flexible C-terminal end (Wynne et al., 1999) and that the resolution seems to be worse in the upper spike region (see Fig. 3.27) this is a convincing result. 6.5Å is in the medium range for published resolutions of icosahedral particles. The reason why the resolution did not go further here might be a certain flexibility of the entire HBV capsid (Rosemann et al., 2005; Rosemann et al., 2012; Böttcher et al., 2006) also crystals from T4 virus capsids only diffracted to 8Å resolution (Tan et al., 2007).

4.4.2 Interaction in the HBV core protein dimer

To evaluate the bridges that are not filled with helices, the atoms at the corresponding positions were checked. These are the S-S-link between the two Cys-61 and the hydrophobic core (Wynne et al., 1999). There is a clear connection visible at the position of the two Cys-61 (Fig. 4.9 (D)). To evaluate the hydrophobic core and the residues accounted for it, the corresponding amino acids were looked at. These are Tyr-6, Phe-9, Leu-15, Leu-16, Phe-18, Leu-16, Phe-18, Phe-19, Phe-23, Phe-24, Trp-102, Phe-103, Phe-110, Val-115, Tyr-118, Leu-119, Phe-122, Trp-125 and Leu-140 (Wynne et al., 1999). The density map docked with the molecular model and the hydrophobic core residues (see Fig. 3.8 (A) and (B) green) at near mass corrected threshold reveals that all these residues are accounted for by mass of the density map. Nevertheless, at a higher threshold value some mass disappears and some bridges become evident. They are occupied by hydrophobic residues and will therefore be analysed here in more detail (see Fig. 3.9). This might help to find direct interaction partners within the hydrophobic core. Here two bridges associated with amino acids from the hydrophobic core are described. These amino acids are Phe-23 and Phe-24 with Trp-102, and Phe-18 with Phe-122 and Trp-125. Moreover two residues were found to form a bridge not described as part of the hydrophobic core (Val27 and Trp-62).

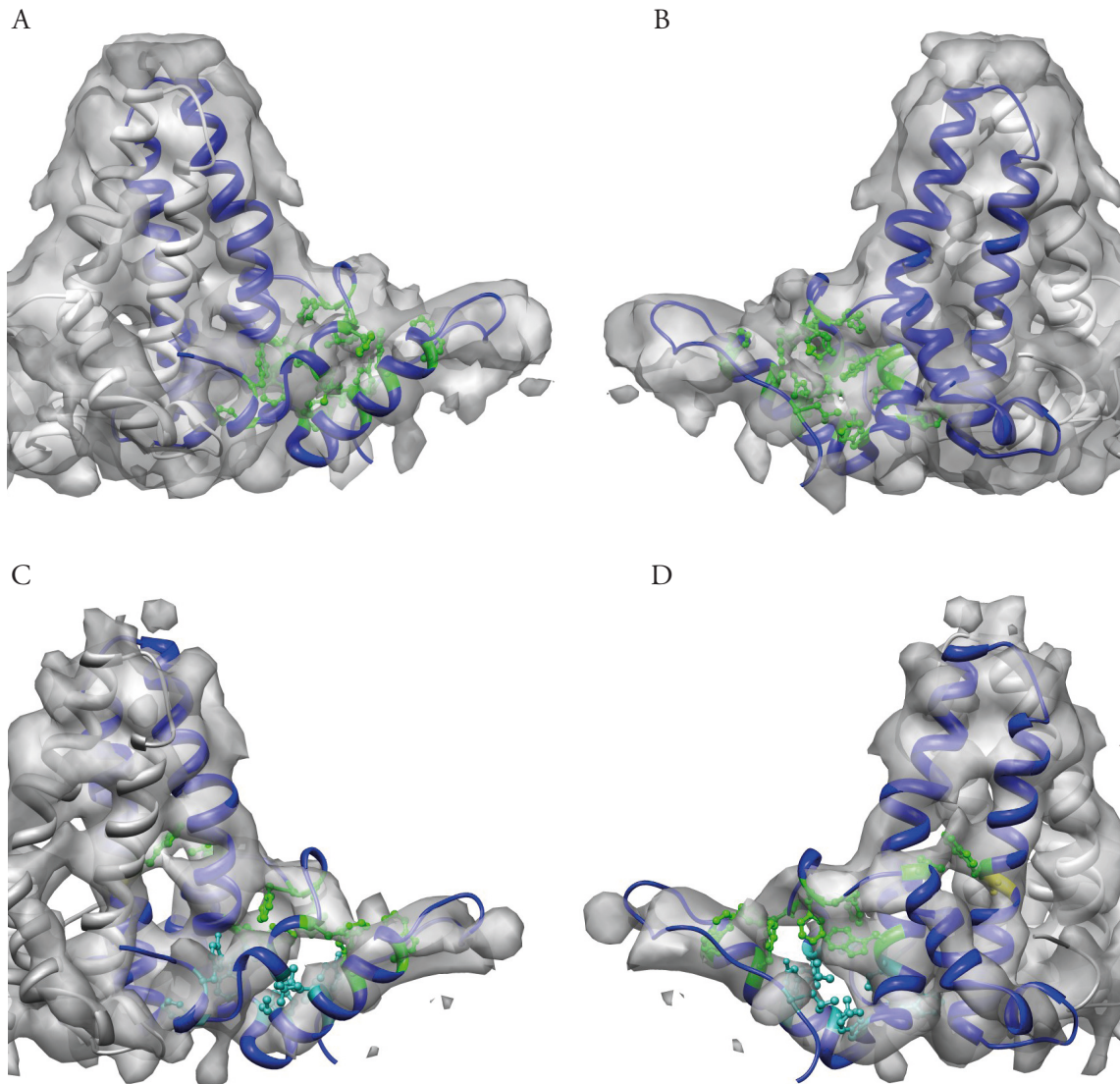


Fig. 4.8 The hydrophobic core in HBV capsids. (A) and (B) Dimer of the HBV T3 capsid at near mass threshold. Docked crystallographic dimer (white and blue), with the amino acids belonging to the hydrophobic core shown in ball and stick mode (green). The hydrophobic core fills the space available. (C) and (D) Same as in (A) and (B), but the threshold value is higher and some prominent bridges appear in the structure. Additionally Cys-61 is in yellow (D).

To evaluate individual connections and their importance for the integrity of the virus capsid it is necessary to mutate single positions, as already performed by Ponsel and Bruss, (2003). They published 52 point mutations and studied the effects on cytoplasmic nucleocapsids and secreted virions. The effect was quantified by electron paramagnetic resonance (EPR) spectroscopy, and the ratio between wild type and the mutated form was calculated. This gives a good measure for the importance of specific amino acids.

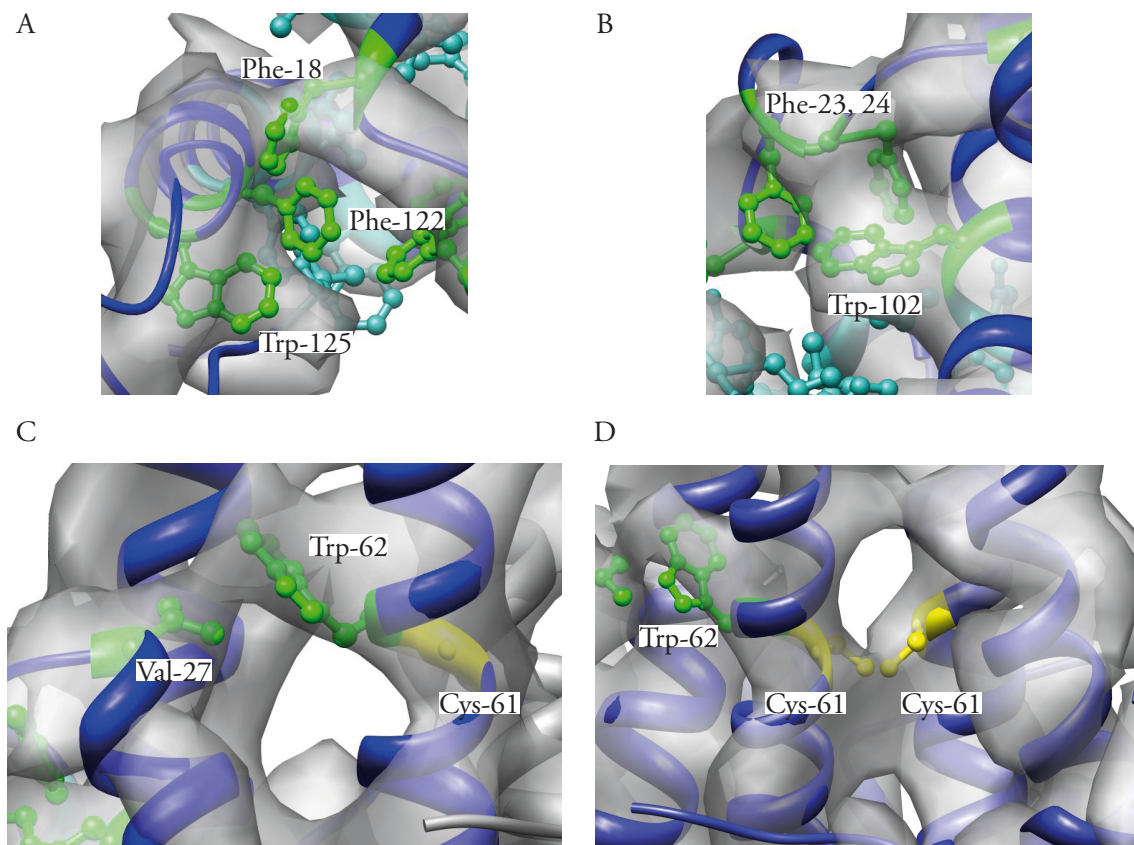


Fig. 4.9 Hydrophobic interaction in the T3 capsid. (A) Bridge seen at the position of Phe-18, Phe-122 and Trp-125. As Trp-125 is further away from the bridge it might not be involved in the interaction there. Nevertheless, the C α distance is only 10Å between Phe-18 and Trp125. (B) Bridge formed between residues Phe-23,-24 and Trp-102. The bridge seen in the density map is filled with the residues and there is a strong interaction possible. Unfortunately no residue involved was mutated yet, to estimate its importance for the folding process. Interactions described in (A) and (B) are all between amino acids belonging to the hydrophobic core (Wynne et al., 1999). (C) Interaction deduced from the density map and not described so far is between Val-27 and Trp-62. There is a clear bridge found in the reconstruction and mutation of the corresponding residues results in a loss of ~65% of the capsids. Interestingly Trp-62 neighbours to Cys-61 forming a S-S-bond, thus possibly stabilising the outer parts of the dimer. (D) S-S-bond between Cys-61. Both cysteines are located inside the density.

The first bridge seen in the density map at a higher threshold value has Phe-18, Phe-122 and Trp-125 in close proximity (Fig. 4.9 (A)). The distances between the C α -atoms were found to be 8Å between Phe-18 and Phe-122, and 10Å between Phe-18 and Trp-125. As Phe-122 and Trp-125 are on the same helix, the distance was not quantified. It seems as if all three amino acids play an important role in capsid formation: Their mutation leads to the absence of secreted virions and only very small portions of cytoplasmic nucleocapsids (Ponsel and Bruss, 2003). This bridge is found at the outer tip of helix $\alpha 5$ and might play an

important stabilizing role. Moreover, helix $\alpha 5$ plays an important role in oligomerization of the dimers to the final capsid (König et al, 1998; Wynne et al., 1999).

The second bridge described (Fig. 4.9 (B)) has again amino acids from the hydrophobic core in close proximity. These are Phe-23, 24 and Trp-102. The respective C α distances are 7Å for Phe-24 and Trp-102, and 10Å for Phe-23 and Trp-102. Again the residues are in close proximity and hydrophobic interaction is well possible there. This could stabilize the lateral loop by connecting it to the central 4-helix bundle. This is further supported as the lateral loop is well resolved, pointing towards low flexibility.

Another connection seen is filled with Val-27 and Trp-62. These two amino acids are not part of the hydrophobic core (Wynne et al., 1999). With a C α distance of 9Å they are in close proximity and interaction is well possible. Moreover it is very interesting to see that the Trp-62 is next to Cys-61 forming the disulfide bond. Although the amount of nucleocapsids and secreted virions was divided by half compared to the wild type (Ponsel and Bruss, 2003), the effect is far weaker as described for other residues. They might not be directly involved in the oligomerisation process, but play a role in the overall stability of the capsid.

This work enabled assignment of residues described as the hydrophobic core (Wynne et al., 1999) to distinct interaction partners. This was possible for two connections found in the density map (Fig. 4.9). If no clear interaction partners were found for amino acids described in Wynne et al., (1999), they might still play a crucial role for oligomerization (Ponsel and Bruss, 2003). In addition, two possible hydrophobic interaction partners outside the hydrophobic core could be detected (see Fig. 4.9).

4.4.3 Interaction between HBV core protein dimers

As the connections between dimers are of vital importance for the integrity of the capsid structure, they were carefully analysed here. Previous studies already suggested important roles for Arg-127 (helix $\alpha 5$) and the proline rich loop (Wynne et al., 1999; König et al., 1998; Ponsel and Bruss, 2003). As no interaction partner was described for Arg-127, it was interesting to see if a acidic amino acid could be found in close proximity. The crystal structure reveals that Arg-127 is opposed by Asp-28, Arg-29 and Asp-32. Looking at the orientation of Arg-127 (Fig. 4.10) reveals no obvious partner for chemical bonding. Point mutations at these position (Ponsel and Bruss, 2003) revealed the importance for oligomerization of the specific amino acids. Mutation of Arg-127 or Asp-28 leads to the loss of cytoplasmic capsids and secreted virions, indicating their vital importance. Mutation of Arg-29 leads to a tremendous loss of EPR signal, and mutation of Asp-32 brings the signal down to about one third (Ponsel and Bruss, 2003). This leads to the assumption that two principle interaction motives are possible. The first one connects Arg-127 with Asp-28 and Arg-29 with Asp-32. In the second case, Arg-127 connects to Asp32 and Arg29 to Asp-28 (Fig. 4.11). Would bridges

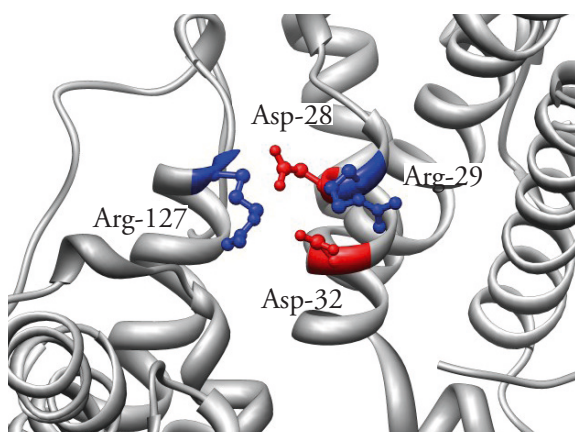


Fig. 4.10 Connection between dimers in the T3 capsid. Helix $\alpha 5$ contains Arg-127 (blue) and is opposed by Arg-28 (blue), Asp-29 and Asp-32 (red) in helix $\alpha 2$. Clear interaction partners are not obvious in the crystal structure.

between dimers support one of the scenarios? The respective $C\alpha$ distances were measured in the molecular model for the above amino acids.

In the C5 symmetry axis connection, the distance between Arg-127 and Asp-28 is $\sim 8\text{\AA}$ and between Arg-127 and Asp-32 it is $\sim 12\text{\AA}$. In the density map no connection can be seen between Arg-127 and Asp-32. This favours a connection between Arg-127 and Asp-28. In the C3 symmetry axis the distances are $\sim 6\text{\AA}$ (Arg-127 \leftrightarrow Asp-28) and $\sim 9\text{\AA}$ (Arg-127 \leftrightarrow Asp-32). As there is a faint bridge (see Fig. 3.30 (A)) between Arg-127 and Asp-28 these two amino acids might again be the interaction partners.

For the crystallographic trimer, distances of $\sim 4\text{\AA}$ (Arg-127 \leftrightarrow Asp-28) and $\sim 7\text{\AA}$ (Arg-127 \leftrightarrow Asp-32) were measured. The density map at this position reveals a clear bridge between Arg-127 and Asp-32 (see Fig. 3.30 (C), arrow). Therefore these two amino acids might hydrostatically interact here. Thus, these four amino acids could function as a molecular switch forming a long (Arg-127 \leftrightarrow Asp28) or a short (Arg-127 \leftrightarrow Asp32) connection.

The relative percentage of long to short connections could help to understand the formation of T3 and T4 capsid types. In T3 1/3 of the dimer interactions are of the short type (1/4 in T4). This shorter link could lead to a steeper curvature between two neighbouring dimers, thus too many of these interactions would prevent the formation of T4 capsids.

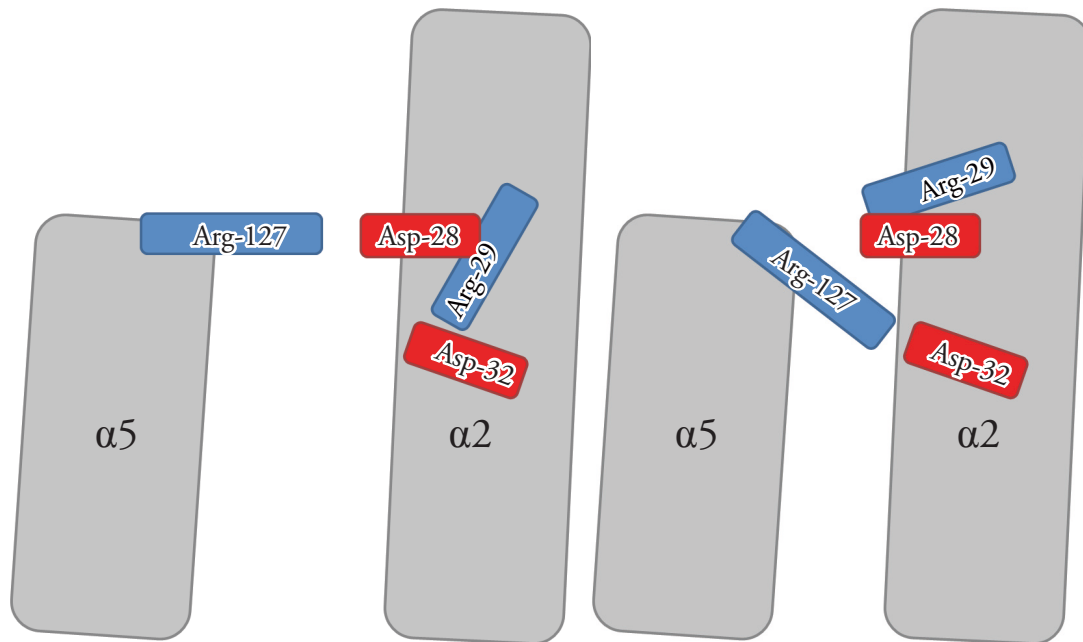


Fig. 4.11 Hypothetical interactions between dimers in HBV capsids. (A) Arg-127 might interact with Asp-29, and Arg-28 with Asp-32. (B), Arg-127 interacts with Asp-32, and Arg-28 with Asp-29.

4.5 Negative staining EM and 3D reconstruction

4.5.1 Comparing overall structural details of protein complexes

The biggest mass differences in the density maps produced here are found between the 20S proteasome and the 20S-PA28 complex. The activator is resolved and the two states can even be discriminated at the single particles level. A second very large difference in two closely related structures is between the T3 and the T4 capsids from HBV. The negative stain reconstructions show two different diameters for the two states, and therefore the separation of both was well possible. This was expected as they could be discriminated on the single particle level.

The orientation of the two hexamers within the different 2x6mer hemocyanins revealed clear differences between the decapod-type, the stomatopod-type and the isopod-type hemocyanin. Within the three different 2x6mer hemocyanins from decapods, slight differences were indicated. Nevertheless they are too small to be confirmed in negative staining and require cryo-EM. Two small differences that could be pinned down here are the shift in the stomatopod-type 2x6mer hemocyanin compared to the one described by Micetic et al., (2010) and the 40° rotation seen in the two Env proteins from HIV. In both cases there are good arguments that the differences seen are true features of the respective data set. For the

2x6mer hemocyanin from *O. scyllarus*, two different 3D models were proposed previously (Micetic et al., 2010; Bijlholt and van Bruggen, 1986). Comparing the class sum images from the 1986 work with the side view shown here (see Fig. 3.9) reveals that the overlap of the two hexamers is the same. This strongly supports the 1986 concept.

For the Env protein from HIV there is a rotational difference of 40° described for the gp120 region. This difference equals a distance at the tip of the V3 loop of $\sim 40\text{\AA}$ and at the opposite position where the V4/V5 is located the distance is $\sim 16\text{\AA}$ (see Fig. 4.4). Therefore the difference is partly above and partly below the resolution limit and should not be overinterpreted. Nevertheless the gp120 molecular model was docked automatically and is additionally supported by biochemical data. Moreover, both models come from the same starting model and as the V3 loop location was further validated with mAb447-52D. All this indicates that the different gp120 conformations seen in NL4-3 and Ada are based on differences present in the data set.

Structural details resolved here were seen in molecular complexes of different size. The size of the complex seems to be less important, but the structural difference. The larger the difference the better the resolution in negative stain. Nevertheless, larger complexes produce more trustworthy results, as differences can already be examined on the single particle level.

4.5.2 Comparing molecular details

The resolution limit of negative staining EM towards molecular details was evaluated using the following structural features. (i) The connections between the 20S proteasome and the PA-28 activator; (ii) the inserted peptide in HBV capsids (iii); the individual subunits in the 2x6mers; and (iv) the V3 loop in HIV Env proteins. The 20S-PA28 complex at different thresholds (see Fig. 4.6) reveals that the first structural details disappearing are the C-terminal ends of PA28, connecting the activator to the 20S core particle. As this is unstructured there might be a certain flexibility in this region. Therefore this molecular detail is not resolved very well. As the capsid of HBV has an inserted protein sequence at the top of the spike, it was interesting to see whether or not it possesses a defined structure or is flexible. In negative stain the entire capsid structure was resolved for T3 and T4; nevertheless it was not possible to see the inserted peptide. This was expected as changes on the secondary structure level can not be visualised by negative staining. Therefore it was necessary to perform cryo-EM in this case. Compared to the density map from negative staining images, the reconstruction from vitrified samples answers the questions raised and showed that the inserted peptide possesses no defined structure (see Fig. 3.31). For the contacts formed by the hemocyanin 2x6mers from decapods it was possible to describe that the 7-stranded β -barrel plays an important role in dimerisation (e. g. Fig. 3.4). However, it was not possible to determine the exact amino acids that are responsible. In the cryo-EM structure from the HBV T3 capsid it was possible

to identify amino acids that are important for structural stability as there are some defined bridges (4.4.3). But although the resolution is far better there, it is necessary that the findings are supported by mutation experiments.

As it is unclear if the V3 loop is co-localised with the V1/V2 loop (indicated with magenta sphere in Fig. 3.15), the molecular mass in this region is not clear. Although the V3 loop was resolved in negative stain and the molecular model docked automatically, it was necessary to validate the position with further experiments. This was attempted here using mAb447-52D to confirm the position of the V3 loop (see Fig. 3.14). Previous studies have already shown in case of HIV the potential of negative staining EM together with immuno labelling (e.g. Lau et al., 2012).

In conclusion, 3D reconstruction of protein complexes from negative staining EM images yielded some reliable informations as confirmed by other methods. However it is important to bear the limits of the method in mind as shown in my PhD study. There is the resolution limit and the rigidity of the molecular structure of interest. The major advantage is certainly that results can be obtained in very short time, and less problems in EM grid preparation occur compared to cryo-EM. Although cryo-EM is undoubtedly most powerful to achieve highly resolved structures, 3D reconstruction from negative staining EM also has advantages.

5 Summary

This work presents different protein complex structures as 3D density maps from negatively stained or unstained vitrified electron microscopical samples. The main goal of this work was to evaluate the potential of negative stain reconstructions with regard to molecular or structural detail. Therefore three 2x6mer hemocyanins from decapod crustaceans (*A. leptodactylus*, *H. americanus* and *C. maenas*) and one from the mantis shrimp *O. scyllarus* were reconstructed. Moreover two different HIV Env proteins, the 20S and the PA28 activated 20S human proteasome and HBV T3 and T4 capsids were studied. All were reconstructed from negative stain data except for the capsids from HBV where images from vitrified samples were also recorded. The four different projects were also designed to answer individual questions.

Comparing the different architectures from the studied 2x6mer hemocyanins with the 2x6mer from the isopod *L. oceanica* and the 4x6mer from the thalassinid shrimp *C. truncata* revealed structural similarities. Either two 2x6mers from decapods or two 2x6mers from the isopod could form the 4x6mer from *C. truncata*. This allowed to infer an evolutionary pathway that starts with an ancestral 4x6mer thalassinid-type hemocyanin. The isopod-type 2x6mer hemocyanin and the decapod-type 2x6mer developed later from the 4x6mer.

The 20S and the PA28 activated 20S proteasome could be clearly discriminated in negative stain. Only single capped 20S-PA28 complexes were found in the applied sample. From the data received it can be speculated that due to activator binding only one side of the proteasome is in the open state.

For HIV Env gp140 proteins from two different virus strands (R5 and X4) it was possible to identify two different conformations. The X4 like NL4-3 shows a more open conformation than the R5 like Ada. Meaning that NL4-3 has a more elongated shape. Moreover an inward rotation of 40° was found in the gp120 part of Ada. For NL4-3 the location of the V3 loop was determined using mAb447-52D and that only one primary receptor CD4 can bind to the trimer.

As the capsid of human HBV is used as an antigen carrier it was of interest to see whether the inserted epitope shows a defined conformation. For the larger T4 it was previously shown that there is none. After initial negative stain reconstructions were conducted a density map of T3 from unstained vitrified samples was calculated with a resolution of 6.5Å. Although the inserted epitope did not show any defined structure some of the revealed molecular interfaces might be important for a better understanding of virus assembly.

Ultimately, the present work yielded a better understanding of the potential and limitations of negative staining in 3D electron microscopy.

6 Zusammenfassung

Im Rahmen dieser Arbeit wurden mittels 3D-Elektronenmikroskopie 3D Rekonstruktionen von verschiedenen Proteinkomplexen mittels Negativkontrastierung oder Vitrifizierung erstellt. Das Hauptziel war hierbei herauszufinden, inwieweit molekulare oder strukturelle Details mittels Negativkontrastierung dargestellt werden können. Hierzu wurden drei 2x6mere Hämocyanine von decapoden Krebsen (*A. leptodactylus*, *H. americanus* und *C. maenas*) und ein 2x6mer des Knallkrebse *O. scyllarus* rekonstruiert. Darüberhinaus wurden zwei Hüllproteine von HIV, das 20S und das PA28-aktivierte 20S Proteasom des Menschen und T3- und T4-Kapside von HBV. Alle Rekonstruktionen wurden aus Bildern negativ kontrastierter Proben erstellt, mit Ausnahme der HBV-Kapside, die auch unter kryo-Bedingungen aufgenommen wurden. Für jedes der vier Projekte sollten außerdem individuelle Fragestellungen beantwortet werden.

Beim Vergleich des Aufbaus der 2x6mer Hämocyanine mit dem des Isopoden *L. oceanica* und dem 4x6meren Hämocyanin von *C. truncata*, stellten wir strukturelle Verwandtschaften fest. Zwei 2x6mere von Decapoden oder zwei 2x6mere des Isopoden können alternativ das 4x6mer von *C. truncata* bilden. Dies ermöglicht es, einen hypothetische Evolutionsweg angefangen bei einem Vorläufer-4x6mer hin zu den 2x6mer Hämocyaninen der Decapoden und Isopoden zu formulieren. Hierbei blieb das 4x6mer bis heute bei den Thalassiniden (Maulwurfskrebsen) erhalten.

Zwischen 20S und PA28-aktiviertem 20S Proteasom konnte in negativ kontrastierten Proben sehr gut unterschieden werden. Es wurden nur 20S Partikel gefunden, die den Aktivator auf einer Seite gebunden hatten. Vermutlich wird durch die Aktivierung auf nur einer Seite auch nur eine Seite des Proteasoms geöffnet. Die 3D-Rekonstruktion stützt diese Hypothese.

Für zwei gp140-Hüllproteine von HIV konnten unterschiedliche Konformationen gezeigt werden. NL4-3 (X4) zeigt eine offenere Struktur und Ada (R5) eine geschlosseneren. Das heißt, NL4-3 zeigt eine gestrecktere Konformation. Darüber hinaus wurde eine Rotation um 40° im gp120 Bereich der beiden Molekülkomplexe im Vergleich zueinander gefunden. Für NL4-3 konnte mithilfe des mAb447-52D die Lage des V3-Loops gezeigt werden und dass nur ein einzelnes CD4 Molekül bindet.

Für die HBV-Kapside sollte in T3 ein inseriertes Peptid gezeigt werden. Von T4 war bereits bekannt, dass keine definierte Struktur eines solchen Peptids vorliegt. Zur ersten Einschätzung wurden die Proben negativ kontrastiert und später vitrifiziert. Es konnte eine Auflösung des T3-Kapsids von 6.5Å erreicht werden und obwohl das inserierte Peptid nicht aufgelöst werden konnte konnten neue Einblicke in die Quartärstruktur gewonnen werden.

Letztendlich trägt diese Arbeit zu einem besseren Verständnis der Vor- und Nachteile von negativ kontrastierten Proben in der 3D-Elektronenmikroskopie bei.

7 Appendix

Abbreviations	
AleHc	<i>Astacus leptodactylus</i> hemocyanin
CCV	cross correlation value
CHR	C-terminal heptat repeat
CmaHc	<i>Carcinus maenas</i> hemocyanin
DCPs	double cleaved products
EPR	electro-paramagnetic resonance
GMP	good manufacturing praxis
gp120	glycoprotein 120
gp140	glycoprotein 140
gp41	glycoprotein 41
HamHc	<i>Homarus americanus</i> hemocyanin
HBV	hepatitis B virus
HIV	human immunodeficiency virus
JGU	Johannes Gutenberg-Universität Mainz
mAb	monoclonal antibody
NHR	N-terminal heptat repeat
OscHc	<i>Odontodactylus scyllarus</i> hemocyanin
pdbentry	protein data bank
SIV	simian immunodeficiency virus

Amino acid abbreviations	
Alanine	Ala
Arginine	Arg
Asparagine	Asn
Aspartic acid	Asp
Cysteine	Cys
Glutamic acid	Glu
Glutamine	Gln
Glycine	Gly
Histidine	His
Isoleucine	Iso
Leucine	Leu
Lysine	Lys
Methionine	Met
Phenylalanine	Phe
Proline	Pro
Serine	Ser
Threonine	Thr
Tryptophan	Trp
Tyrosine	Tyr
Valine	Val

2% Uranyl formate solution

Boil diH₂O, cool down slowly to room temp.

Add 0.1g Uranyl formate to an empty beaker

Add 5mL diH₂O

Vortex 10 minutes in the dark

Add 2 μ L 10N KOH per 1ml of solution

Vortex 10 minutes in the dark

Spin at maximum speed on table top centrifuge for 10 min.

Filter the solution with a 0.2 μ m syringe filter in the dark

8 Bibliography

- Arnold, K., Bordoli, L.; Kopp, J.; Schwede, T. (2006): The SWISS-MODEL workspace: a web-based environment for protein structure homology modelling. In: *Bioinformatics* 22 (2), S. 195–201.
- Bedford, L.; Layfield, R.; Mayer, R. J.; Peng, J.; Xu, P. (2011): Diverse polyubiquitin chains accumulate following 26S proteasomal dysfunction in mammalian neurones. In: *Neurosci. Lett.* 491 (1), S. 44–47.
- Bijlholt, M.; van Bruggen, E. F. (1986): A model for the architecture of the hemocyanin from the arthropod *Squilla mantis* (Crustacea, Stomatopoda). In: *Eur. J. Biochem.* 155 (2), S. 339–344.
- Bijlholt, M. M.; van Heel, M. G.; van Bruggen, E. F. (1982): Comparison of 4 X 6-meric hemocyanins from three different arthropods using computer alignment and correspondence analysis. In: *J. Mol. Biol.* 161 (1), S. 139–153.
- Binley, J. M.; Sanders, R. W.; Clas, B.; Schuelke, N.; Master, A.; Guo, Y. et al. (2000): A recombinant human immunodeficiency virus type 1 envelope glycoprotein complex stabilized by an intermolecular disulfide bond between the gp120 and gp41 subunits is an antigenic mimic of the trimeric virion-associated structure. In: *J. Virol.* 74 (2), S. 627–643.
- Bochtler, M.; Ditzel, L.; Groll, M.; Hartmann, C.; Huber, R. (1999): The proteasome. In: *Annu Rev Biophys Biomol Struct* 28, S. 295–317.
- Borries B.; Ruska E. (1938): Das Übermikroskop als Fortsetzung des Lichtmikroskops. In: *Verhandlungen d. Ges. dt. Naturforscher und Ärzte* 95, S. 72–77.
- Bohn, S.; Beck, F.; Sakata, E.; Walzthoeni, T.; Beck, M.; Aebersold, R. et al. (2010): Structure of the 26S proteasome from *Schizosaccharomyces pombe* at subnanometer resolution. In: *Proc. Natl. Acad. Sci. U.S.A.* 107 (49), S. 20992–20997.
- Böttcher, B.; Wynne, S. A.; Crowther, R. A. (1997): Determination of the fold of the core protein of hepatitis B virus by electron cryomicroscopy. In: *Nature* 386 (6620), S. 88–91.

- Böttcher, B.; Vogel, M.; Ploss, M.; Nassal, M. (2006): High plasticity of the hepatitis B virus capsid revealed by conformational stress. In: *J. Mol. Biol.* 356 (3), S. 812–822.
- BRENNER, S.; HORNE, R. W. (1959): A negative staining method for high resolution electron microscopy of viruses. In: *Biochim. Biophys. Acta* 34, S. 103–110.
- Burgess, Stan A.; Walker, Matt L.; Thirumurugan, Kavitha; Trinick, John; Knight, Peter J. (2004): Use of negative stain and single-particle image processing to explore dynamic properties of flexible macromolecules. In: *Journal of Structural Biology* 147 (3), S. 247–258.
- Burmester, T. (2001): Molecular evolution of the arthropod hemocyanin superfamily. In: *Mol. Biol. Evol.* 18 (2), S. 184–195.
- Buzon, V.; Natrajan, G.; Schibli, D.; Campelo, F.; Kozlov, M. M.; Weissenhorn, W. (2010): Crystal structure of HIV-1 gp41 including both fusion peptide and membrane proximal external regions. In: *PLoS Pathog.* 6 (5), S. e1000880.
- Caffrey, M. (2011): HIV envelope: challenges and opportunities for development of entry inhibitors. In: *Trends Microbiol.* 19 (4), S. 191–197.
- Carlo, S. de; Harris, J. R. (2011): Negative staining and cryo-negative staining of macromolecules and viruses for TEM. In: *Micron* 42 (2), S. 117–131.
- Carragher, B.; Kisseberth, N.; Kriegman, D.; Milligan, R. A.; Potter, C. S.; Pulokas, J.; Reilein, A. (2000): Leginon: an automated system for acquisition of images from vitreous ice specimens. In: *J. Struct. Biol.* 132 (1), S. 33–45.
- Cascio, Paolo; Call, Matthew; Petre, Benjamin M.; Walz, Thomas; Goldberg, Alfred L. (2002): Properties of the hybrid form of the 26S proteasome containing both 19S and PA28 complexes. In: *EMBO J.* 21 (11), S. 2636–2645.
- Chen, B.; Vogan, E. M.; Gong, H.; Skehel, J. J.; Wiley, D. C.; Harrison, S. C. (2005): Determining the structure of an unliganded and fully glycosylated SIV gp120 envelope glycoprotein. In: *Structure* 13 (2), S. 197–211.

-
- Chen, V. B.; Arendall, W. B.; Headd, J. J.; Keedy, D. A.; Immormino, R. M.; Kapral, G.J. et al. (2010): MolProbity: all-atom structure validation for macromolecular crystallography. In: *Acta Crystallogr. D Biol. Crystallogr.* 66 (Pt 1), S. 12–21.
- Conway, J. F.; Cheng, N.; Zlotnick, A.; Wingfield, P. T.; Stahl, S. J.; Steven, A. C. (1997): Visualization of a 4-helix bundle in the hepatitis B virus capsid by cryo-electron microscopy. In: *Nature* 386 (6620), S. 91–94.
- da Fonseca, P. C. A.; Morris, E. P. (2008): Structure of the human 26S proteasome: subunit radial displacements open the gate into the proteolytic core. In: *J. Biol. Chem.* 283 (34), S. 23305–23314.
- Davis, I. W.; Leaver-Fay, A.; Chen, V. B.; Block, J. N.; Kapral, G. J.; Wang, X. et al. (2007): MolProbity: all-atom contacts and structure validation for proteins and nucleic acids. In: *Nucleic Acids Res.* 35 (Web Server issue), S. W375-83.
- Derby, N. R.; Gray, S.; Wayner, E.; Campogan, D.; Vlahogiannis, G.; Kraft, Z. et al. (2007): Isolation and characterization of monoclonal antibodies elicited by trimeric HIV-1 Env gp140 protein immunogens. In: *Virology* 366 (2), S. 433–445.
- Dick, T. P.; Ruppert, T.; Groettrup, M.; Kloetzel, P. M.; Kuehn, L.; Koszinowski, U. H. et al. (1996): Coordinated dual cleavages induced by the proteasome regulator PA28 lead to dominant MHC ligands. In: *Cell* 86 (2), S. 253–262.
- Dubochet, J.; Lepault J.; Freeman R.; Berriman J. A. and Homo J.-C: Electron microscopy of frozen water and aqueous solutions. In: *Journal of Microscopy* 1982 (128), S. 219–237.
- Dubochet, J. and McDowall A.: Vitrification of pure water for electron microscopy. In: *Journal of Microscopy* 1981 (124), S. 3–4.
- Egerton, R. F. (2012): TEM-EELS: A personal perspective. In: *Ultramicroscopy* 119, S. 24–32.
- Ruska E. (1932): Das Elektronenmikroskop. In: *Zeitschrift für Physik* (78), S. 318–339.

- Eswar, N.; Eramian, D.; Webb, B.; Shen, M.-Y.; Sali, A. (2008): Protein structure modeling with MODELLER. In: *Methods Mol. Biol.* 426, S. 145–159.
- Fiser, A.; Do, R. K.; Sali, A. (2000): Modeling of loops in protein structures. In: *Protein Sci.* 9 (9), S. 1753–1773.
- Frank, J. (2002): Single-particle imaging of macromolecules by cryo-electron microscopy. In: *Annu Rev Biophys Biomol Struct* 31, S. 303–319.
- Gatsogiannis, C.; Markl, J. (2009): Keyhole limpet hemocyanin: 9-A CryoEM structure and molecular model of the KLH1 didecamer reveal the interfaces and intricate topology of the 160 functional units. In: *J. Mol. Biol.* 385 (3), S. 963–983.
- Gatsogiannis, C.; Moeller, A.; Depoix, F.; Meissner, U.; Markl, J. (2007): Nautilus pompilius hemocyanin: 9 A cryo-EM structure and molecular model reveal the subunit pathway and the interfaces between the 70 functional units. In: *J. Mol. Biol.* 374 (2), S. 465–486.
- Goddard, T. D.; Huang, C. C.; Ferrin, T. E. (2007): Visualizing density maps with UCSF Chimera. In: *J. Struct. Biol.* 157 (1), S. 281–287.
- Groll, M.; Ditzel, L.; Löwe, J.; Stock, D.; Bochtler, M.; Bartunik, H. D.; Huber, R. (1997): Structure of 20S proteasome from yeast at 2.4 Å resolution. In: *Nature* 386 (6624), S. 463–471.
- Guex, N.; Peitsch, M. C. (1997): SWISS-MODEL and the Swiss-PdbentryViewer: an environment for comparative protein modeling. In: *Electrophoresis* 18 (15), S. 2714–2723.
- Harauz, G.; van Heel, M. G. (1986): Exact filter for general geometry in three dimensional reconstruction. In: *OPTIK* 73 (4), S. 146–156.
- Harris, A.; Borgnia, M. J.; Shi, D.; Bartesaghi, A.; He, H.; Pejchal, R. (2011): Trimeric HIV-1 glycoprotein gp140 immunogens and native HIV-1 envelope glycoproteins display the same closed and open quaternary molecular architectures. In: *Proc. Natl. Acad. Sci. U.S.A.* 108 (28), S. 11440–11445.

- Harris, J. R. (1969): Some negative contrast staining features of a protein from erythrocyte ghosts. In: *J. Mol. Biol.* 46 (2), S. 329–335.
- Harris, J. R. (1991): Negative staining-carbon film technique: new cellular and molecular applications. In: *J Electron Microsc Tech* 18 (3), S. 269–276.
- Harris, J. R. (1999): Negative staining of thinly spread biological particulates. In: *Methods Mol. Biol.* 117, S. 13–30.
- Harris, J. R. (2007): Negative staining of thinly spread biological samples. In: *Methods Mol. Biol.* 369, S. 107–142.
- Harris, J. R. (2008): Negative staining across holes: application to fibril and tubular structures. In: *Micron* 39 (2), S. 168–176.
- Harris, J. R.; Schröder, E.; Isupov, M. N.; Scheffler, D.; Kristensen, P.; Littlechild, J. A. et al. (2001): Comparison of the decameric structure of peroxiredoxin-II by transmission electron microscopy and X-ray crystallography. In: *Biochim. Biophys. Acta* 1547 (2), S. 221–234.
- Harrison, J. E.; Lynch, J. B.; Sierra, L.-J.; Blackburn, L. A.; Ray, N.; Collman, R. G.; Doms, R. W. (2008): Baseline resistance of primary human immunodeficiency virus type 1 strains to the CXCR4 inhibitor AMD3100. In: *J. Virol.* 82 (23), S. 11695–11704.
- Hazes, B.; Magnus, K. A.; Bonaventura, C.; Bonaventura, J.; Dauter, Z.; Kalk, K. H.; Hol, W. G. (1993): Crystal structure of deoxygenated *Limulus polyphemus* subunit II hemocyanin at 2.18 Å resolution: clues for a mechanism for allosteric regulation. In: *Protein Sci.* 2 (4), S. 597–619.
- Hershko, A.; Ciechanover, A. (1998): The ubiquitin system. In: *Annu. Rev. Biochem.* 67, S. 425–479.
- Hershko, A.; Ciechanover, A.; Varshavsky, A. (2000): Basic Medical Research Award. The ubiquitin system. In: *Nat. Med.* 6 (10), S. 1073–1081.
- Higgins, D. G.; Sharp, P. M. (1988): CLUSTAL: a package for performing multiple sequence alignment on a microcomputer. In: *Gene* 73 (1), S. 237–244.

- Huang, C.-C.; Tang, M.; Zhang, M.-Y.; Majeed, S.; Montabana, E.; Stanfield, R. L. (2005): Structure of a V3-containing HIV-1 gp120 core. In: *Science* 310 (5750), S. 1025–1028.
- Iijima, S. (1973): Direct observation of lattice defects in H-Nb₂O₅ by high resolution electron microscopy. In: *Acta Cryst.* (A29), S. 18–24.
- Jaroniec, C. P.; Kaufman, J. D.; Stahl, S. J.; Viard, M.; Blumenthal, R.; Wingfield, P. T.; Bax, A. (2005): Structure and dynamics of micelle-associated human immunodeficiency virus gp41 fusion domain. In: *Biochemistry* 44 (49), S. 16167–16180.
- Kim, M.; Chen, B.; Hussey, R. E.; Chishti, Y.; Montefiori, D.; Hoxie, J. A. et al. (2001): The stoichiometry of trimeric SIV glycoprotein interaction with CD4 differs from that of anti-envelope antibody Fab fragments. In: *J. Biol. Chem.* 276 (46), S. 42667–42676.
- Kiselev, N. A.; Rosier, D. J. de; Klug, A. (1968): Structure of the tubes of catalase: analysis of electron micrographs by optical filtering. In: *J. Mol. Biol.* 35 (3), S. 561–566.
- Klamp, T.; Schumacher, J.; Huber, G.; Kuhne, C.; Meissner, U.; Selmi, A. (2011): Highly Specific Auto-Antibodies against Claudin-18 Isoform 2 Induced by a Chimeric HBcAg Virus-Like Particle Vaccine Kill Tumor Cells and Inhibit the Growth of Lung Metastases. In: *Cancer Research* 71 (2), S. 516–527.
- Kloetzel, P. M. (2001): Antigen processing by the proteasome. In: *Nat. Rev. Mol. Cell Biol.* 2 (3), S. 179–187.
- Kloetzel, P. M. (2004): Generation of major histocompatibility complex class I antigens: functional interplay between proteasomes and TPPII. In: *Nat. Immunol.* 5 (7), S. 661–669.
- König, S.; Beterams, G.; Nassal, M. (1998): Mapping of homologous interaction sites in the hepatitis B virus core protein. In: *J. Virol.* 72 (6), S. 4997–5005.
- Kremer, J. R.; Mastrorarde, D. N.; McIntosh, J. R. (1996): Computer visualization of three-dimensional image data using IMOD. In: *J. Struct. Biol.* 116 (1), S. 71–76.

- Kwong, P. D.; Wyatt, R.; Majeed, S.; Robinson, J.; Sweet, R. W.; Sodroski, J.; Hendrickson, W. A. (2000): Structures of HIV-1 gp120 envelope glycoproteins from laboratory-adapted and primary isolates. In: *Structure* 8 (12), S. 1329–1339.
- Kwong, P. D.; Wyatt, R.; Robinson, J.; Sweet, R. W.; Sodroski, J.; Hendrickson, W. A. (1998): Structure of an HIV gp120 envelope glycoprotein in complex with the CD4 receptor and a neutralizing human antibody. In: *Nature* 393 (6686), S. 648–659.
- Lander, G. C.; Estrin, E.; Matyskiela, M. E.; Bashore, C.; Nogales, E.; Martin, A. (2012): Complete subunit architecture of the proteasome regulatory particle. In: *Nature* 482 (7384), S. 186–191.
- Lander, G. C.; Stagg, S. M.; Voss, N. R.; Cheng, A.; Fellmann, D.; Pulokas, J. et al. (2009): Appion: an integrated, database-driven pipeline to facilitate EM image processing. In: *J. Struct. Biol.* 166 (1), S. 95–102.
- Larivière, L.; Seizl, M.; Cramer, P. (2012): A structural perspective on Mediator function. In: *Curr. Opin. Cell Biol.* 24 (3), S. 305–313.
- Larkin, M. A.; Blackshields, G.; Brown, N. P.; Chenna, R.; McGettigan, P. A.; McWilliam, H. et al. (2007): Clustal W and Clustal X version 2.0. In: *Bioinformatics* 23 (21), S. 2947–2948.
- Lau, P.-W.; Guiley, K. Z.; De, N.; Potter, C. S.; Carragher, B.; MacRae, I. J. (2012): The molecular architecture of human Dicer. In: *Nat. Struct. Mol. Biol.* 19 (4), S. 436–440.
- Liu, J.; Bartesaghi, A.; Borgnia, M. J.; Sapiro, G.; Subramaniam, S. (2008): Molecular architecture of native HIV-1 gp120 trimers. In: *Nature* 455 (7209), S. 109–113.
- Ludtke, S. J.; Baldwin, P. R.; Chiu, W. (1999): EMAN: semiautomated software for high-resolution single-particle reconstructions. In: *J. Struct. Biol.* 128 (1), S. 82–97.
- Lusso, P.; Earl, Patricia L.; Sironi, F.; Santoro, F.; Ripamonti, C.; Scarlatti, G. (2005): Cryptic nature of a conserved, CD4-inducible V3 loop neutralization epitope in the native envelope glycoprotein oligomer of CCR5-restricted, but not CXCR4-using, primary human immunodeficiency virus type 1 strains. In: *J. Virol.* 79 (11), S. 6957–6968.

- Mao, Y.; Wang, L.; Gu, C.; Herschhorn, A.; Xiang, S.-H.; Haim, H. et al. (2012): Subunit organization of the membrane-bound HIV-1 envelope glycoprotein trimer. In: *Nat. Struct. Mol. Biol.* 19 (9), S. 893–899.
- Markl J.; Decker H. (1992): Molecular structure of the arthropod hemocyanins. In: *Advances in Comparative and Environmental Physiology*, S. 325–363.
- Markl, J.; Decker, H.; Stöcker, W.; Savel, A.; Linzen, B.; Schutter, W. G.; van Bruggen, E. F. (1981): On the role of dimeric subunits in the quaternary structure of arthropod hemocyanins. In: *Hoppe-Seyler's Z. Physiol. Chem.* 362 (2), S. 185–188.
- Markl, J.; Savel, A.; Decker, H.; Linzen, B. (1980): Hemocyanins in spiders, IX. Homogeneity, subunit composition and the basic oligomeric structure of *Eurypelma californicum* hemocyanin. In: *Hoppe-Seyler's Z. Physiol. Chem.* 361 (5), S. 649–660.
- Martin, A. G.; Depoix, F.; Stohr, M.; Meissner, U.; Hagner-Holler, S.; Hammouti, K. et al. (2007): *Limulus polyphemus* hemocyanin: 10Å cryo-EM structure, sequence analysis, molecular modelling and rigid-body fitting reveal the interfaces between the eight hexamers. In: *J. Mol. Biol.* 366 (4), S. 1332–1350.
- Mastrorarde, D. N. (1997): Dual-axis tomography: an approach with alignment methods that preserve resolution. In: *J. Struct. Biol.* 120 (3), S. 343–352.
- Matthias B.; Lars D.; Michael G.; Claudia H. and Robert H.: THE PROTEASOME.
- McDowell, E. M.; Combs, J. W.; Newkirk, C. (1983): A quantitative light and electron microscopic study of hamster tracheal epithelium with special attention to so-called intermediate cells. In: *Exp. Lung Res.* 4 (3), S. 205–226.
- McLellan, J. S.; Pancera, M.; Carrico, C.; Gorman, J.; Julien, J.-P.; Khayat, R. et al. (2011): Structure of HIV-1 gp120 V1/V2 domain with broadly neutralizing antibody PG9. In: *Nature* 480 (7377), S. 336–343.
- Mičetić, I.; Losasso, C.; Di Muro, P.; Tognon, G.; Benedetti, P.; Beltramini, M. (2010): Solution structures of 2×6-meric and 4×6-meric hemocyanins of crustaceans *Carcinus aestuarii*, *Squilla mantis* and *Upogebia pusilla*. In: *J. Struct. Biol.* 171 (1), S. 1–10.

- Mindell, J. A.; Grigorieff, N. (2003): Accurate determination of local defocus and specimen tilt in electron microscopy. In: *J. Struct. Biol.* 142 (3), S. 334–347.
- Mishto, M.; Luciani, F.; Holzhütter, H.-G.; Bellavista, E.; Santoro, A.; Textoris-Taube, K. et al. (2008): Modeling the in vitro 20S proteasome activity: the effect of PA28- α and of the sequence and length of polypeptides on the degradation kinetics. In: *J. Mol. Biol.* 377 (5), S. 1607–1617.
- Moscoso, C. G.; Sun, Y.; Poon, S.; Xing, L.; Kan, E.; Martin, L. et al. (2011): Quaternary structures of HIV Env immunogen exhibit conformational vicissitudes and interface diminution elicited by ligand binding. In: *Proc. Natl. Acad. Sci. U.S.A.* 108 (15), S. 6091–6096.
- Mosier, D. E. (2009): How HIV changes its tropism: evolution and adaptation? In: *Curr Opin HIV AIDS* 4 (2), S. 125–130.
- Mulder, A. M.; Yoshioka, C.; Beck, A. H.; Bunner, A. E.; Milligan, R. A.; Potter, C. S. et al. (2010): Visualizing ribosome biogenesis: parallel assembly pathways for the 30S subunit. In: *Science* 330 (6004), S. 673–677.
- Naganawa, S.; Yokoyama, M.; Shiino, T.; Suzuki, T.; Ishigatsubo, Y.; Ueda, A. et al. (2008): Net positive charge of HIV-1 CRF01_AE V3 sequence regulates viral sensitivity to humoral immunity. In: *PLoS ONE* 3 (9), S. e3206.
- Nicholas, H.; Nicholas D. W.; Deerfield B.J. (1997): GeneDoc: analysis and visualization of genetic variation. In: *Embnew. news* (4), S. 14.
- Nickell, S.; Beck, F.; Korinek, A.; Mihalache, O.; Baumeister, W.; Plitzko, J. M. (2007): Automated cryoelectron microscopy of “single particles” applied to the 26S proteasome. In: *FEBS Lett.* 581 (15), S. 2751–2756.
- Ohi, M.; Li, Y.; Cheng, Y.; Walz, T. (2004): Negative Staining and Image Classification - Powerful Tools in Modern Electron Microscopy. In: *Biol Proced Online* 6, S. 23–34.

- Orlova, E. V.; Dube, P.; Harris, J. R.; Beckman, E.; Zemlin, F.; Markl, J.; van Heel, M. (1997): Structure of keyhole limpet hemocyanin type 1 (KLH1) at 15 Å resolution by electron cryomicroscopy and angular reconstitution. In: *J. Mol. Biol.* 271 (3), S. 417–437.
- Pancera, M.; Majeed, S.; Ban, Y.-E. A.; Chen, L.; Huang, C.-C.; Kong, L. et al. (2010): Structure of HIV-1 gp120 with gp41-interactive region reveals layered envelope architecture and basis of conformational mobility. In: *Proc. Natl. Acad. Sci. U.S.A.* 107 (3), S. 1166–1171.
- Pettersen, E. F.; Goddard, T. D.; Huang, C. C.; Couch, G. S.; Greenblatt, D. M.; Meng, E. C.; Ferrin, T. E. (2004): UCSF Chimera--a visualization system for exploratory research and analysis. In: *J Comput Chem* 25 (13), S. 1605–1612.
- Ponsel, D.; Bruss, V. (2003): Mapping of amino acid side chains on the surface of hepatitis B virus capsids required for envelopment and virion formation. In: *J. Virol.* 77 (1), S. 416–422.
- Potter, C. S.; Chu, H.; Frey, B.; Green, C.; Kisseberth, N.; Madden, T. J. et al. (1999): Legion: a system for fully automated acquisition of 1000 electron micrographs a day. In: *Ultramicroscopy* 77 (3-4), S. 153–161.
- Poveda, E.; Alcamí, J.; Paredes, R.; Córdoba, J.; Gutiérrez, F.; Llibre, J. M. et al. (2010): Genotypic determination of HIV tropism - clinical and methodological recommendations to guide the therapeutic use of CCR5 antagonists. In: *AIDS Rev* 12 (3), S. 135–148.
- Quispe, J.; Damiano, J.; Mick, S. E.; Nackashi, D. P.; Fellmann, D.; Ajero, T. G. et al. (2007): An improved holey carbon film for cryo-electron microscopy. In: *Microsc. Microanal.* 13 (5), S. 365–371.
- Radermacher, M. (1988): Three-dimensional reconstruction of single particles from random and nonrandom tilt series. In: *J Electron Microscop Tech* 9 (4), S. 359–394.
- Radermacher, M.; Wagenknecht, T.; Verschoor, A.; Frank, J. (1987): Three-dimensional reconstruction from a single-exposure, random conical tilt series applied to the 50S ribosomal subunit of *Escherichia coli*. In: *J Microsc* 146 (Pt 2), S. 113–136.

-
- Rehm, P.; Pick, C.; Borner, J.; Markl, J.; Burmester, T. (2012): The diversity and evolution of chelicerate hemocyanins. In: *BMC Evol. Biol.* 12, S. 19.
- Roseman, A. M.; Borschukova, O.; Berriman, J. A.; Wynne, S. A.; Pumpens, P.; Crowther, R. A. (2012): Structures of hepatitis B virus cores presenting a model epitope and their complexes with antibodies. In: *J. Mol. Biol.* 423 (1), S. 63–78.
- Roseman, A. M.; Berriman, J. A.; Wynne, S. A.; Butler, P. J. G.; Crowther, R. A. (2005): A structural model for maturation of the hepatitis B virus core. In: *Proc. Natl. Acad. Sci. U.S.A.* 102 (44), S. 15821–15826.
- Rosenthal, P. B.; Henderson, R. (2003): Optimal determination of particle orientation, absolute hand, and contrast loss in single-particle electron cryomicroscopy. In: *J. Mol. Biol.* 333 (4), S. 721–745.
- Sali, A.; Blundell, T. L. (1993): Comparative protein modelling by satisfaction of spatial restraints. In: *J. Mol. Biol.* 234 (3), S. 779–815.
- Saxton, W. O.; Frank, J. (1977): Motif detection in quantum noise-limited electron micrographs by cross-correlation. In: *Ultramicroscopy* 2 (2-3), S. 219–227.
- Schatz, M.; Orlova, E. V.; Dube, P.; Jäger, J.; van Heel, M. (1995): Structure of *Lumbricus terrestris* hemoglobin at 30 Å resolution determined using angular reconstitution. In: *J. Struct. Biol.* 114 (1), S. 28–40.
- Schatz, M.; van Heel, M. (1990): Invariant classification of molecular views in electron micrographs. In: *Ultramicroscopy* 32 (3), S. 255–264.
- Scherbaum, S.; Ertas, B.; Gebauer, W.; Burmester, T. (2010): Characterization of hemocyanin from the peacock mantis shrimp *Odontodactylus scyllarus* (Malacostraca: Hoplocarida). In: *J. Comp. Physiol. B, Biochem. Syst. Environ. Physiol.* 180 (8), S. 1235–1245.
- Serysheva, I. I.; Orlova, E. V.; Chiu, W.; Sherman, M. B.; Hamilton, S. L.; van Heel, M. (1995): Electron cryomicroscopy and angular reconstitution used to visualize the skeletal muscle calcium release channel. In: *Nat. Struct. Biol.* 2 (1), S. 18–24.

- Sharon, M.; Kessler, N.; Levy, R.; Zolla-Pazner, S.; Görlach, M.; Anglister, J. (2003): Alternative conformations of HIV-1 V3 loops mimic beta hairpins in chemokines, suggesting a mechanism for coreceptor selectivity. In: *Structure* 11 (2), S. 225–236.
- Shibatani, T.; Carlson, E. J.; Larabee, F.; McCormack, A. L.; Früh, K.; Skach, W. R. (2006): Global organization and function of mammalian cytosolic proteasome pools: Implications for PA28 and 19S regulatory complexes. In: *Mol. Biol. Cell* 17 (12), S. 4962–4971.
- Sines, J.; Rothnagel, R.; van Heel, M.; Gaubatz, J. W.; Morrisett, J. D.; Chiu, W. (1994): Electron cryomicroscopy and digital image processing of lipoprotein(a). In: *Chem. Phys. Lipids* 67-68, S. 81–89.
- Strehl, B.; Seifert, U.; Krüger, E.; Heink, S.; Kuckelkorn, U.; Kloetzel, P. M. (2005): Interferon-gamma, the functional plasticity of the ubiquitin-proteasome system, and MHC class I antigen processing. In: *Immunol. Rev.* 207, S. 19–30.
- Tan, W. S.; McNae, I. W.; Ho, K. L.; Walkinshaw, M. D. (2007): Crystallization and X-ray analysis of the T = 4 particle of hepatitis B capsid protein with an N-terminal extension. In: *Acta Crystallogr. Sect. F Struct. Biol. Cryst. Commun.* 63 (Pt 8), S. 642–647.
- Thompson, J. D.; Gibson, T. J.; Plewniak, F.; Jeanmougin, F.; Higgins, D. G. (1997): The CLUSTAL_X windows interface: flexible strategies for multiple sequence alignment aided by quality analysis tools. In: *Nucleic Acids Res.* 25 (24), S. 4876–4882.
- Thompson, J. D.; Higgins, D. G.; Gibson, T. J. (1994): CLUSTAL W: improving the sensitivity of progressive multiple sequence alignment through sequence weighting, position-specific gap penalties and weight matrix choice. In: *Nucleic Acids Res.* 22 (22), S. 4673–4680.
- Thon F. (1966): Zur Defokussierungsabhängigkeit des Phasenkontrastes bei der elektronenmikroskopischen Abbildung. In: *Zeitschrift für Naturforschung* (21a), S. 476–478.
- Tran, E. E. H.; Borgnia, M. J.; Kuybeda, O.; Schauder, D. M.; Bartesaghi, A.; Frank, G. A. et al. (2012): Structural mechanism of trimeric HIV-1 envelope glycoprotein activation. In: *PLoS Pathog.* 8 (7), S. e1002797.

-
- UNAIDS (2011): World AIDS Day Report 2011. Hg. v. UNAIDS. UNAIDS. Switzerland. Online verfügbar unter www.unaids.org.
- Unno, M.; Mizushima, T.; Morimoto, Y.; Tomisugi, Y.; Tanaka, K.; Yasuoka, N.; Tsukihara, T. (2002): The structure of the mammalian 20S proteasome at 2.75 Å resolution. In: *Structure* 10 (5), S. 609–618.
- van Heel, M. (1987): Angular reconstitution: a posteriori assignment of projection directions for 3D reconstruction. In: *Ultramicroscopy* 21 (2), S. 111–123.
- van Heel, M.; Frank, J. (1981): Use of multivariate statistics in analysing the images of biological macromolecules. In: *Ultramicroscopy* 6 (2), S. 187–194.
- van Heel, M.; Gowen, B.; Matadeen, R.; Orlova, E. V.; Finn, R.; Pape, T. et al. (2000): Single-particle electron cryo-microscopy: towards atomic resolution. In: *Q. Rev. Biophys.* 33 (4), S. 307–369.
- van Heel, M.; Harauz, G.; Orlova, E. V.; Schmidt, R.; Schatz, M. (1996): A new generation of the IMAGIC image processing system. In: *J. Struct. Biol.* 116 (1), S. 17–24.
- van Heel, M.; Schatz, M. (2005): Fourier shell correlation threshold criteria. In: *J. Struct. Biol.* 151 (3), S. 250–262.
- Vanlandschoot, P.; van Houtte, F.; Hoek, F.; Nieuwland, R.; Leroux-Roels, G. (2003): *Saccharomyces cerevisiae*-derived HBsAg preparations differ in their attachment to monocytes, immune-suppressive potential, and T-cell immunogenicity. In: *J. Med. Virol.* 70 (4), S. 513–519.
- Voges, D.; Zwickl, P.; Baumeister, W. (1999): The 26S proteasome: a molecular machine designed for controlled proteolysis. In: *Annu. Rev. Biochem.* 68, S. 1015–1068.
- Volbeda, A.; Hol, W. G. (1989): Crystal structure of hexameric haemocyanin from *Panulirus interruptus* refined at 3.2 Å resolution. In: *J. Mol. Biol.* 209 (2), S. 249–279.
- Voss, N. R.; Yoshioka, C. K.; Radermacher, M.; Potter, C. S.; Carragher, B. (2009): DoG Picker and TiltPicker: software tools to facilitate particle selection in single particle electron microscopy. In: *J. Struct. Biol.* 166 (2), S. 205–213.

- Ward J. H. (1963): Hierarchical grouping to optimize an objective function. In: *Journal of the American statistical association* 58 (301), S. 236–244.
- Whitby, F. G.; Masters, E. I.; Kramer, L.; Knowlton, J. R.; Yao, Y.; Wang, C. C.; Hill, C. P. (2000): Structural basis for the activation of 20S proteasomes by 11S regulators. In: *Nature* 408 (6808), S. 115–120.
- White, T. A.; Bartesaghi, A.; Borgnia, M. J.; Meyerson, J. R.; La Cruz, M. J. V. de; Bess, J. W. et al. (2010): Molecular architectures of trimeric SIV and HIV-1 envelope glycoproteins on intact viruses: strain-dependent variation in quaternary structure. In: *PLoS Pathog.* 6 (12), S. e1001249.
- Wu, S.-R.; Löving, R.; Lindqvist, Bi.; Hebert, H.; Koeck, P. J. B.; Sjöberg, Ma.; Garoff, H. (2010): Single-particle cryoelectron microscopy analysis reveals the HIV-1 spike as a tripod structure. In: *Proc. Natl. Acad. Sci. U.S.A.* 107 (44), S. 18844–18849.
- Wyatt, R.; Sodroski, J. (1998): The HIV-1 envelope glycoproteins: fusogens, antigens, and immunogens. In: *Science* 280 (5371), S. 1884–1888.
- Wynne, S. A.; Leslie, A. G.; Butler, P. J.; Crowther, R. A. (1999): Crystallization of hepatitis B virus core protein shells: determination of cryoprotectant conditions and preliminary X-ray characterization. In: *Acta Crystallogr. D Biol. Crystallogr.* 55 (Pt 2), S. 557–560.
- Zanetti, G.; Briggs, J. A. G.; Grünewald, K.; Sattentau, Q. J.; Fuller, S. D. (2006): Cryo-electron tomographic structure of an immunodeficiency virus envelope complex in situ. In: *PLoS Pathog.* 2 (8), S. e83.
- Zhang, C. W.; Chishti, Y.; Hussey, R. E.; Reinherz, E. L. (2001): Expression, purification, and characterization of recombinant HIV gp140. The gp41 ectodomain of HIV or simian immunodeficiency virus is sufficient to maintain the retroviral envelope glycoprotein as a trimer. In: *J. Biol. Chem.* 276 (43), S. 39577–39585.
- Zhou, T.; Xu, L.; Dey, B.; Hessel, A. J.; van Ryk, D.; Xiang, S.-H. et al. (2007): Structural definition of a conserved neutralization epitope on HIV-1 gp120. In: *Nature* 445 (7129), S. 732–737.

- Zhou, Z. H. (2008): Towards atomic resolution structural determination by single-particle cryo-electron microscopy. In: *Current Opinion in Structural Biology* 18 (2), S. 218–228.
- Zhu, P.; Liu, J.; Bess, J.; Chertova, E.; Lifson, J. D.; Grisé, H. et al. (2006): Distribution and three-dimensional structure of AIDS virus envelope spikes. In: *Nature* 441 (7095), S. 847–852.
- Zhu, P.; Winkler, H.; Chertova, E.; Taylor, K. A.; Roux, K. H. (2008): Cryoelectron tomography of HIV-1 envelope spikes: further evidence for tripod-like legs. In: *PLoS Pathog.* 4 (11), S. e1000203.
- Zhuang, K.; Finzi, A.; Tasca, S.; Shakirzyanova, M.; Knight, H.; Westmoreland, S. et al. (2011): Adoption of an “open” envelope conformation facilitating CD4 binding and structural remodeling precedes coreceptor switch in R5 SHIV-infected macaques. In: *PLoS ONE* 6 (7), S. e21350.

9 Danksagung - Acknowledgment

10 Erklärung and Copyright

Erklärung

I hereby declare that I wrote the dissertation submitted without any unauthorized external assistance and used only sourced acknowledged work. All textual passages which are appropriated or paraphrased from published or unpublished texts as well as information obtained from oral sources are duly indicated and listed in accordance with bibliographic rules. In carrying out this research, I complied with the rules of standard scientific practice as formulated in the statutes of Johannes Gutenberg-University Mainz to insure standard scientific practise.

Datum, Ort

Philipp Arnold

Copyright

Die Inhalte dieses Werkes sind urheberrechtliches Eigentum des Instituts für Zoologie im Fachbereich Biologie der Johannes Gutenberg-Universität Mainz.

11 Curriculum vitae

Curriculum Vitae | P. A.

Personal Data

Date of birth	October, 4th 1982
Place of birth	Kaiserslautern
Nationality	German

Education

10/2012	Target completion date of my PhD in 3D-electron microscopy
8/2008	Entered PhD programme at the Johannes-Gutenberg-University (JGU) Mainz
11/2009 – 10/2012	Member of the Max-Planck Graduate Centre with the JGU Mainz
2010 – 2011	Studentspeaker of the Max-Planck Graduate Center with the JGU Mainz
9/2007 – 7/2008	Diplom thesis „3D-reconstruction of the recombinant human protease Meprin β “
11/2007 - 4/2008	JGU Mainz scholarship to sponsor qualified thesis candidates

Curriculum Vitae | P. A.

5/2007 – 7/2007

Diplom exams with majors in zoology, biophysics and physiological chemistry

10/2003 – 8/2007

Undergraduate biology studies at JGU Mainz

4/2003

Abitur at the Hohenstaufen Gymnasium, Kaiserslautern

2002 - 2003

Area representative for Youth for Understanding e.V. for the southwestern region of Germany (Hessen, Rheinland-Pfalz, Saarland)

2001 - 2005

Trainer at various pre-departure and post-arrival seminars for exchange students

2001 - 2002

Interview coordination for potential exchange students

8/1999 – 7/2000

German government scholarship programme for exchange students to Tampa, Florida (USA).

Publications, Conferences & Schools

2012

Orientation of gp120 subunits in two different trimeric gp140 HIV-1 Env molecules; **Arnold P.** et al., (in prep)

Structure of different arthropod 2x6mers with a link to the 4x6mer of the thalassinid ghost shrimp *Callinassa truncata*; **Arnold P.** and Kuehne C. et al., (in prep)

Curriculum Vitae | P. A.

2011

Presentation to the 30th Tiers Winter School on proteases and their inhibitors

DNA condensation with spermine dendrimers: interaction in solution, charge inversion, and morphology control; Kurzenbach D., Velten C., **Arnold P.**, Kizilsavas G. and Hinderberger D., *Soft Matter* (2011)

Soft skill seminar: Project management

Gordon Research Conference on "Three dimensional electron microscopy" with poster presentation

Presentation to the 29th Tiers Winter School on proteases and their inhibitors

2010

Presentation to the German Zoological Society (DZG Tagung)

EMBO Practical Course on cryo-electron microscopy and 3D image processing

Soft skill seminar: Communication skills

Gordon research conference on "Three dimensional electron microscopy" with poster presentation

28th Tiers Winter School on proteases and their inhibitors

Curriculum Vitae | P. A.

2009

Presentation to the German Zoological Society (DZG Tagung)

Meeting of the Royal Microscopy Society, London, UK

Awarded best presentation among students and post-docs at the 27th Tiers Winter School on proteases and their inhibitors

2008

EMC meeting in Aachen with poster presentation

Methods

Preparation of negative stain and cryo samples

Room temperature and cryo TEM

Single particle reconstruction (advanced)

Tomogram reconstruction (intermediate)

SDS-gel electrophoresis, western blot and in situ hybridisation (all intermediate)

Software

Imagic5 (expert), EMAN (advanced), Appion (advanced), UCSF Chimera (expert), etomo (intermediate), Modeller9vX (intermediate), Bash (basic), MS Office, InDesign

Curriculum Vitae | P. A.

other Languages

English (fluent)
Spanish (basics)
Russian (basics)

other Interests

Fishing
Sports (Judo, Volleyball, Soccer)
Travelling